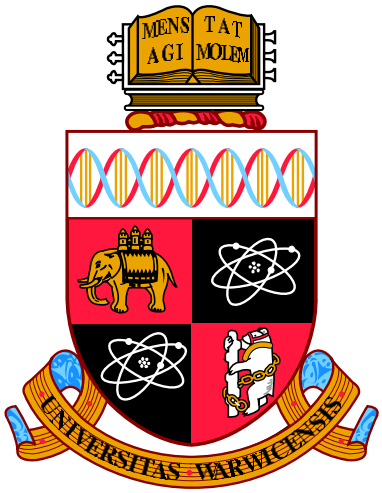

Density Functional Theory Investigations of MnSb(0001)/GaAs(111)B

by

Haiyuan Wang

Thesis

Submitted to the University of Warwick

in part fulfilment for the degree of

Doctor of Philosophy

Department of Physics

February 2017

THE UNIVERSITY OF WARWICK

Contents

Acknowledgements

This thesis has been turned into reality with the immeasurable help, support and efforts from a lot of individuals. Foremost, I would like to thank my brilliant supervisor, Dr. Gavin Bell, without whom I could not imagine that I would have such opportunity to enjoy my research in UK. I have to say I learned far more than what I ever thought from him including the broad knowledge of my subject, the rigorous scientific attitude and even the beautiful British cultures. I should also give thanks to Dr. Jim Robinson, Dr. David Quigley and Dr. Phil Hasnip for their technical guidance of improving my computing skills. Countless times I just pop into their offices with my maybe very stupid questions, but their patience made me feel I am really lucky to be able to join this group.

I submit my heartiest gratitude to three of my seniors in our group, Dr. Matt Bradley, Dr. James D. Aldous, and Dr. Christopher W. Burrows because of their patient instructions and encouragement. I still remember Matt emailed me saying that "Don't worry if it all seems very difficult at first. It took me about a year before I was able to really understand what I was doing....." I printed it out and hung it up on the wall to constantly motivate myself. James almost unconditionally supported everything related to research even though we have never actually met in person yet. Sometimes, he just sits in front of the computer and sends me message that he is ready to answer all of my questions if I need..... It has been a really long time, but I still save the first correction of my paper from Chris, which is full with annotations and his smiley-face icon in the margin of manual.....

My special gratitude also goes to my wonderful friends Dr. Sepehr Vasheghani Farahani (who can be relied on all the time like an older brother and always take the responsibility to cheer us up), Dr. Daesung Park (who is often grabbed by me to the library correcting my figures or answering various dumb questions no matter how busy he is), Collins E. Ouserigha (who always organises parties for us to have fun even I am not a good dancer!.....Goat pepper soup.....), Geanina Apachitei (with whom I spent the majority of my shopping time and who is the only one I always

want to try to take care of), Akash Bhatnagar (who let me notice that Indian food just taste so good!), Alifah Rahman (who shares her rich experience how to become a great mum), two clever Chinese Juniors - Mingmin Yang and Zhengdong Luo (who make me feel so proud of being their SHI-JIE), Sun qi (who always prepares free dinner, and makes sure I have hot food to eat like my mum always does), Philip Mousley (who is really a right person to discuss with about life and science because of his eruditness and nice personality). All of them made my PhD life different, colourful and unforgettable.

I extend my thanks to Dr. Georg Held, Dr. Jacopo Ardini and Dr. James Mudd for their training of CLEED software. Without them, I may not be able to complete this thesis. I appreciate Prof. Dejun Li, Prof. Hui Lui, Shengjie Dong, and Hao Zhu for their deep discussions about my work.

Finally, I must thank my family especially my parents and grandma of their unsparing love and support. They provide exceptional understanding as well as tolerance throughout, even if I am not around for about four years.

Declarations

I declare that this thesis contains an account of my research work carried out at the Department of Physics, University of Warwick between November 2012 and September 2016 under the supervision of Dr. Gavin R. Bell. The research reported here has not been previously submitted, wholly or in part, at this or any other academic institution for admission to a higher degree.

The CASTEP calculations which have provided the results presented in this thesis have been performed on several high-performance computing clusters (Syrah, Minerva, and Tinis) in both the Surface, Interface and Thin Film Group and the Centre for Scientific Computing at the University of Warwick. A number of the results presented in this thesis have been analysed using Accelrys Materials Studio.

The GaAs/MnSb samples were grown by Dr. James D. Aldous using MBE chamber at the University of Warwick. XRD data presented in Chapter 5 was provided by Dr. James D. Aldous and Dr. Chris W. Burrows. XPS and MEIS in Chapters 5 were all taken by Dr. James D. Aldous. The TEM images in Chapters 5 and 6 were taken by Dr. Ana Sanchez. The LEED data in Chapter 4 required to fit I-V curve were performed by Dr. Vinod Dhanak at the University of Liverpool. The CLEED simulation programme was provided by Dr. Greg Held at University of Reading. All other data and interpretation has been carried out by the author.

Haiyuan Wang

February 2017

Several articles based on the work of this PhD period have been published, are in press, or have been submitted for publication:

D. S. Park, S. K. Vasheghani Farahani, M. Walker, J. J. Mudd, **H. Y. Wang**, A. R. Krupski, E. B. Thorsteinsson, D. Seghier, C. J. Choi, C. J. Youn, and C. F. Mcconville, *Recrystallization of highly-mismatched $Be_xZn_{1-x}O$ alloys: formation of a degenerate interface*, ACS Appl. Mat. Interfaces. **6**, 21 (2014).

D. S. Park, **H. Y. Wang**, S. K. Vasheghani Farahani, M. Walker, A. Bhatnagar, D. Seghier, C. J. Choi, J. H. Kang, and C. F. Mcconville, *Surface passivation of semiconducting oxides by self-assembled nanoparticles*, Sci. Rep. **6**, 18449 (2016).

H. Y. Wang, J. D. Aldous, V. Dhanak, C. W. Burrows, E. C. Ouserigha, and G. R. Bell, *Surface stabilisation of Sb-terminated MnSb(0001): theory and experiment* is ready to submit.

H. Y. Wang, J. D. Aldous, C. W. Burrows, E. C. Ouserigha, and G. R. Bell, *Formation mechanisum of metastable half-metallic cubic MnSb phase* is ready to submit.

The work presented in this thesis has been presented at the following national and international conferences.

Surface structure in Mn(Ga)Sb(0001) surface by first principles (poster presentation), 11th international conference on the structure of surfaces, University of Warwick, Coventry, UK (July 2014).

Surface relaxation, Ga segregation and electronic structure in MnSb(0001) epitaxial films on GaAs(111)B from first principles (poster presentation), Magnetisum 2015, University of Leeds, Leeds, UK (March 2015).

Surface reconstruction and Ga segregation at MnSb(0001) surfaces: experiments and density functional theory (oral presentation), ICMAT2015 IUMRS-ICA2015, MRS, Singapore (June 2015).

Formation of secondary half-metallic cubic MnSb on GaAs(111)B (poster presentation) The 9th international symposium on metallic multilayers (MML), Uppsala, Swenden (June 2016).

Trainings and project work during this PhD period.

NAG/HECToR Training course on CASTEP in Computer Science Building, University of Warwick (25th-26th March, 2013).

KKR Green functions for calculations of spectroscopic, transport and magnetic properties University of Warwick (9th-12th July, 2013).

CASTEP training workshop in Department of Materials, University of Oxford (17th-21st August, 2015).

The majority of CASTEP skills have been implemented in the whole PhD project study. Parts of SPRKKR skills and technologies have been performed in a joint project funded by Innovate UK and driven by a company, European Thermodynamics. This Project work has been successfully completed under the supervision of Prof. Julie B. Staunton at the University of Warwick during the period from 1st February to 30th April in 2016.

Abstract

Heteroepitaxial growth of magnetic materials (*e.g.* ferromagnets) onto III-V semiconductors (*e.g.* GaAs and InP) based on spin injection methods has received great attention due to their potential applications in spintronics. However, the formation of distinct surface states, highly mismatched heterointerfaces, and the consequent lower spin polarisation of the ferromagnets have been regarded as major challenges. Therefore, comprehensive understanding the surface and interface properties to select the better magnetic materials for growth are of great importance. In recent studies, MnSb thin films have been successfully grown on GaAs substrates by molecular beam epitaxy (MBE). During the thin film growth, significant surface variations including surface reconstruction, atomic diffusion, and the formation of secondary phases [cubic MnSb (c-MnSb)] have been observed. Hence, the formation of the surface defects (atomic segregation/surface reconstruction) and secondary phases for the niccolite MnSb(n-MnSb)/GaAs heterostructures are presented in this thesis using first-principles calculations.

Experimentally, a number of surface reconstructions of n-MnSb(0001) have been found after the growth of MnSb thin films on GaAs(111)B substrates, wherein the (2×2) surface reconstruction is prevalent. Therefore, quantitative surface structure of MnSb(0001) - (2×2) determination is presented, using density functional theory (DFT) and low energy electron diffraction (LEED) data fitting methods.

Atomic out-diffusion and surface segregation of Ga has been found in the MnSb(0001)/GaAs(111) system by X-ray photoemission spectroscopy (XPS) and medium energy ion scattering (MEIS) measurements. DFT calculations are used to explain these results. In addition, an optimal concentration of the diffused Ga atoms has been shown by comparing the formation energy/surface energy change. Modifications in the structural and electronic properties [atomic bond length, atomic bond angle, charge density difference, and density of states (DOS)] of the Ga-in-MnSb(0001) system are discussed.

Finally, the formation mechanism of c-MnSb polymorph through thermodynamic phase transition caused by Ga segregation in MnSb(0001)/GaAs(111)B has been presented. Atomic relaxation of the model structures driven by Ga substitution into Mn sites at the subsurface layers provides critical insights for the evolution of secondary c-MnSb polymorph. Further theoretical prediction of the new system (MnSb/GaSb) with the cubic polymorph is also provided. All the theoretical models, calculations, and results presented give a crucial guideline for epitaxial growth of half-metallic c-MnSb for the next generation of magnetic applications.

Abbreviations and common symbols

2D	Two dimensional
3D	Three dimensional
BFGS	Broyden-Fletcher-Goldfarb-Shanno
CASTEP	Cambridge Sequential Total Energy Package
CLEED	Cambridge low energy electron diffraction
c-MnSb	MnSb in the cubic phase
DFT	Density functional theory
DM	Density mixing
DOS	Density of states
ECR	Electron counting rule
EDFT	Ensemble density functional theory
E_f	Fermi level
FCC	Face-center cubic
GGA	Generalised gradient approximation
GMR	Giant magnetoresistance
HCP	hexagonal close-packed
HDD	Hard disk dirve
HK	Hohenberg-Kohn
HM	Half-metallic
HMF	Half-metallic ferromagnet
HRTEM	High resolution transmission electron microscopy
$J_{\mathrm{Sb/Mn}}$	Beam equivalent pressure BEP ratio
KS	Kohn-Sham
LCAO	Linear combined atomic orbitals
LDA	Local density approximation
LEED	Low energy electron diffraction
μ_{B}	Bohr magneton, 5.788×10^{5} eV/T

MBE	Molecular beam epitaxy
MEIS	Medium energy ion scattering
MRAM	Magnetoresistive random-access memory
n-MnSb	MnSb in the niccolite phase
P	Spin-pairing energy
PBE	Perdew-Burke-Ernzerhof functional
PDOS	Partial density of states
PW91	Perdew-Wang functional
RT	Room temperature
SADP	Selected area diffraction pattern
SCF	Self-consistent field
SE	Schrödinger equation
SP	Spin-polarisation
STM	scanning tunnelling microscope
T_{c}	Curie temperature
T_{sub}	Substrate temperature
TEM	Transmission electron microscope
TMP	Transition metal pnictides
TMR	Temperature tunneling magnetoresistance
USPPs	Ultrasoft pseudopotentials
w-MnSb	MnSb in the wurtzite structure
XPS	X-ray photoelectron spectroscopy
XRD	X-ray diffraction

Chapter 1

Introduction

1.1 Motivation

There are normally advantages to reducing the physical size and making devices smaller, however, in the course of pursuing miniaturisation, the presence of quantum mechanical tunnel currents limits the advancement of devices. Namely, the electron has ability to penetrate barriers. For example, the distance between transistors become smaller as more transistors are setted onto a chip. Therefore, electron barriers which were thick enough to block current are so thin that electrons can go through them now. One way to complement current electronic devices and create novel functionalities is to manipulate intrinsic spins in a system rather than only using their charge distribution, namely, spintronics [1–3]. A large variety of innovative applications have already been manufactured by this new technique such as spin transistors [4], spin valves [5], and spin batteries [6].

With regard to the fabrication of spintronic devices, the main issue is to search for appropriate materials. It is well-known that ferromagnetic materials have a large spontaneous internal magnetisation, which can be readily generated and controlled by a three or four orders of magnitude smaller external field. In addition, ferromagnetic metals generally have short electron mean free path (about 200 Å), which means the collision of particles easily occurs in ferromagnetic metals. This makes these materials exquisitely surface-sensitive so that their thin films can be effectively utilised [7–9].

Mn-based binaries (*e.g.* MnBi, MnAs and MnSb) among the class of transition metal pnictides (TMP) are mainly such ferromagnets [10]. (*e.g.* other materials in this group such as CrSb, CrAs and CoSb belong to antiferromagnetic compounds [11, 12], and NiSb, TiSb are paramagnetic [12].) Furthermore, apart from MnBi and MnSb having higher Curie temperatures (T_{C}) ($T_{\mathrm{C}}^{\mathrm{MnBi}} = 628K$ [13],

$T_C^{MnSb} = 587K$ [12]) than MnAs ($T_C^{MnAs} = 318\ K$ [14]), MnSb also has a strong magnetic anisotropy. Specifically, the higher (lower or even trivial) coercive field occurs with the applied magnetic field perpendicular (parallel) to the out-of-plane of MnSb, MnSb[0001]. Meanwhile, the coercive fields are almost identical along the in-planes of MnSb, *e.g.* $[2\bar{1}\bar{1}0]$ and $[\bar{1}100]$ directions [15].

In reality, heteroepitaxial growth of magnetic materials, especially ferromagnets (*e.g.* MnAs and MnSb), onto III-V semiconductors (*e.g.* Si and GaAs) is a prime pathway to realise the combination of injected magnetic electrons with semiconductors [16–18]. However, a point worth noticing is that even if a material is ferromagnetic in bulk, there is no guarantee it keeps the same properties in the surface and interface regions. Understanding the magnetic properties of surfaces and interfaces is thus crucialy important. Moreover, heteroexpitaxial thin film growth may be impeded by the surface reconstruction of the substrate layer, therefore, MnSb(0001) surface reconstruction plays a vital role for "inverted" (semiconductor on ferromagnet) interface study. Recently, low temperature tunneling magnetoresistance (TMR) in MnAs/GaAs/MnAs tunnel junctions has been determined [19], and the corresponding investigations of surface reconstruction for MnAs have been reported [20, 21]. To date, there is no theoretical publication focusing on surface reconstruction of MnSb(0001). A better comprehension of the correspondence between surface reconstruction and magnetic moment is still required.

Spin injection efficiency is another key consideration. In general, the larger the spin polarisation at the Fermi level, the higher the injected efficiency is. As a consequence, half-metal materials are expected to be the ideal injected materials due to their 100 % spin polarisation. Cubic MnSb (c-MnSb) possesses half-metallicity, but it is not the stable phase in nature. This thesis investigates some formation mechanisms of c-MnSb films.

1.2 Organisation of the thesis

The work presented in this thesis concerns energetic (*i.e.* phase stability) and structural characterisation (*i.e.* defect formation and new phase transformations)

of n-MnSb(0001) thin films growth on GaAs(111) substrate. A lot of theoretical calculations have been carried out using the Cambridge serial total energy package (CASTEP), and parts of jobs have been performed with the Cambridge low energy electron diffraction (CLEED) software package to verify the CASTEP results.

The thesis is arranged as follows. In the first chapter, the electronic, structural and magnetic characteristics of different morphologies of MnSb, as well as their potential values for spintronics are presented. Some basic surface defects concepts and notation methodology are also demonstrated. Chapter 2 is devoted to an introduction of the theoretical background, simulation packages, and some fundamental optimisation procedures which are required for computational accuracy.

Chapter 3 is the first results chapter, dealing with the (0001) surface stability comparison of different terminations of n-MnSb. The same approaches are then generalised to other materials within transitional metal pnictides to show the correspondence between stability and their magnetic properties. The final section contains the stability comparison of (0001) and $(1\bar{1}00)$ surfaces for n-MnSb. Chapter 4 is dedicated to the surface structure calculations of (2×2) surface reconstructions of n-MnSb(0001). Reconstruction models are tested by comparison to quantitative low energy electron diffraction (LEED).

Chapter 5 is concerned with surface segregation, which has been previously observed during the growth of MnSb(0001) on GaAs(111)B. Based on the experimental observations, extensive theoretical calculations (*e.g.* segregation energy, substitution energy, surface energy change, and electronic structures etc.) are presented to sysmatically understand such atom segregation. In the final results chapter, chapter 6, various interface structures of c-MnSb/n-MnSb with and without Ga substitution are proposed to suggest that Ga is crucial to form half-metallic c-MnSb films. Meanwhile, a set of new interface designs of MnSb/GaSb have been shown in this chapter to give a further prediction of c-MnSb formation mechanisum. In chapter 7, final conclusions of this project and some suggestions for future work are presented.

1.3 Spintronics

Spintronics (spin electronics) is an emerging and promising technology, as mentioned before, its main objective is to obtain control over electron flow through a system by manipulating the intrinsic spin instead of electronic charge. Hence, these devices attempt to make the full-use of the quantum mechanical spins. This can overcome not only a limit of practical device size, but it can also enhance the power efficiency. Details on the decreased physical size has been explained in the motivation section of this thesis. For the case of power efficiency, several electronic devices such as field-effect transistors usually have intrinsic leakage currents during their operation, *e.g.* gradual energy loss flows through a charged capacitor in a device, even it is in an off-mode. Therefore, spintronic technology can offer promising opportunities for overcoming the limit of the power efficiency of the conventional electronic devices.

A typical example of turning discovery into commercialised application of heterojunctions is the giant magnetoresistance (GMR) effect. It has been observed in multilayer thin-film structures composed of alternating magnetic and nonmagnetic layers [22, 23]. The underlying mechanism of fabricating these GMR materials is on the basis of the electrical resistance change in interlayers while spin aligns relative to an applied magnetic field. The overall resistance of system is high for antiparallel alignment and low for parallel alignment. In practical applications, several commercial products are available using GMR materials such as magnetic field sensors (the first commercial product) [24], and read-heads for magnetic hard disk drives (the most influential one) [25]. On the introduction of GMR, the storage capacity of hard disks increased from 1 to 20 GB.

Recently, tunnel magnetoresistance (TMR) pioneered by Julliere [26] has been entensively used to replace GMR in some spintronic devices such as magnetoresistive random-access memories (MRAMs) and hard disk dirves (HDDs) [27]. The difference between GMR and TMR is that the nonmagnetic spacer in GMR is a metal film (*i.e.* ferromagnet-metal-ferromagnet) and in TMR is an insulator (*i.e.* ferromagnet-insulator-ferromagnet). This change can allow TMR to achieve a larger

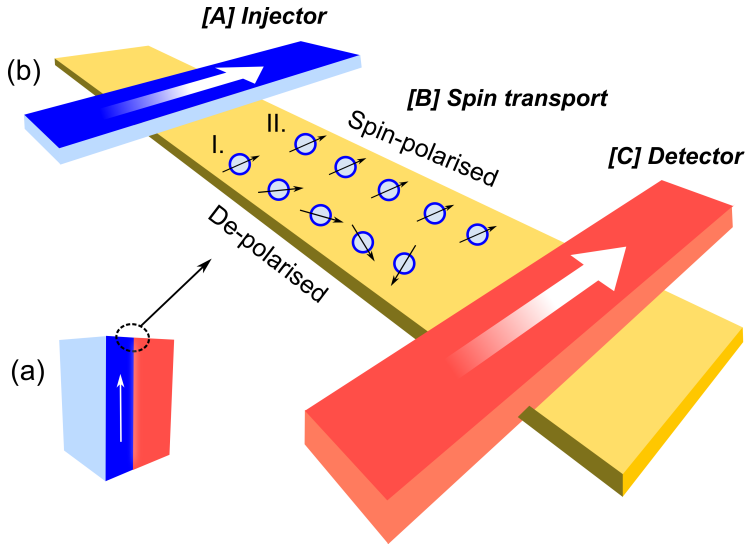

Figure 1.1: (a) Schematic of spin injection from a magnetic thin film (blue region) to a non-magnetic/soft-magnetic substrate (red region) across the interface. (b) Information on detailed spin transport via two ways, (I) de-polarised and (II) polarised spin transport.

magnetoresistance value [28] and a negligible temperature dependence [29].

In order to realise the spin based semiconductor devices, three fundemental requirements must be emphasised here shown in Fig. 1.1:

- ([A] *Injection-magnetic layers*) Magnetic materials must be used to inject spin polarised currents into conventional non-magnetic semiconductors.

- ([B] *Transport-semiconductor layers*) The spin-coherent lifetime (the time before a spin-polarised current becomes de-polarised) within semiconductors must be long enough to be used in devices, which is related with spin transport in semiconductors. Hagele and his co-workers have already reported there is no electron-spin dephasing [only the way of II occurence shown in Fig. 1.1(b)] in GaAs at low temperatures during transport over 4 μm [30]. This means spin-electronic devices is feasible when magnetic electrons are injected into GaAs.

- ([C] *Detection-magnetic layers*) The spin polarised currents must be detected in devices by effective detection methodologies. Compared with requirement one, a spin analyser has been implemented to the devices [31].

1.4 Spintronics applications for MnSb

The first requirement to find effective injection sources is exceedingly important for hybird spintronic devices, and is the main purpose of this project. Practically, any material planned to be used as injected ion has to fulfill two basic conditions, which are the compatibility with the semiconductor host (*e.g.* lattice mismatch between ferromagnet and semiconductor), and the polarised current sources (normally can be achieved by using ferromagnets). Regarding to the former point, transition metal pnictides (TMP) have the excellent engineering compatibility with III-V substrates, which enables them to become suitable materials for epitaxial growth [32–35].

The latter criterion of spin-polarised carriers can be estimated by the value of spin polarisation (SP), which is defined as

$$SP = \frac{DOS_{\text{up}} - DOS_{\text{down}}}{DOS_{\text{up}} + DOS_{\text{down}}}. \tag{1.1}$$

Here, DOS_{up} and DOS_{down} stand for the density of up-spin (majority spin: $\boldsymbol{s} = \frac{1}{2}$) and down-spin (minority spin: $\boldsymbol{s} = -\frac{1}{2}$) electrons at the Femi level, respectively. Figure 1.2 demonstrates the calculated DOS of three different representative materials with individual SP value. Panel (a) presenting GaAs, as a typical semiconductor, has identical numbers of electrons in two spin states. In such a material, the obvious band gap for spin up and spin down states ($DOS_{\text{up}} = DOS_{\text{down}} = 0$) is capable of being observed close to the Fermi level. Semiconductor-type materials therefore cannot be defined by Equ. 1.1 and also cannot be used as spin state injectors. Figure 1.2(b) and (c) show a similar behaviour with an imbalance of the spin populations at the Fermi level. This imbalance commonly takes place in magnetic materials, thus leading to the unequal spin-up and spin-down carriers at E_f in number. The most highly polarised currents is from half-metallic ferromagnetic (HMF) compounds in which the majority spin (spin-up) displays a metallic behavior while the minority spin (spin-down) is insulating, as shown in Fig. 1.2(c) of *c*-MnSb. Due to this special DOS property, it is demonstrated that HMFs (*c*-MnSb) possesses

100 % SP at the Fermi energy [36]. Such a property thus makes *c*-MnSb an ideal spintronic injecting candidate.

Figure 1.2(b) shows a partially polarised compound, *n*-MnSb, which has a spin polarisation *SP* of 18 %. Such low *SP* value may not be enough to make it highly attractive in spintronics, but it is adequate to develop some applications in magneto-optical devices and in waveguides [37] due to the large Kerr effect [38]. Kerr effect (a larger Kerr effect) describes a change (a quick change) in the reflective index of a material with applied fields. Therefore, it can be also used to modulate light since the Kerr effect reponds quickly to changes in the electric field. All of materials commonly show the Kerr effect with different degree of response, which is dependent on the Kerr constant, K, in the relation of $\Delta n = \lambda K E^2$ (where, n is the refractive index of a material and E is the applied field). For example, materials, whose constituent atoms readily displace under an applied electric field like ferroelectrics, exhibit strong interactions in the refractive index of the materials under light illumination. Such high Kerr effect permits the complete light transmission through the material to be obtained even under smaller external electric fields, while no light is transmitted as the electric field is turned off. It recently has been reported that this Kerr effect can be even increased at the oxidation surface [39]. As a result, both polymorph phases of MnSb could play a crucial role for different type of devices.

1.5 Crystal structure of binary pnictides

The transition metal pnictides (TMP) are composed of a transition-metal atom (such as Mn, Ni, or Cr) and a Group V atom (such as P, As or Sb). These materials are generally stabilised at hexagonal NiAs-type (niccolite) structure (*e.g.* MnSb, named as *n*-MnSb) with P63/mmc space group (number 194 in the International Tables for X-ray Crystallography). For MnSb, there are also another two metastable [cubic (*c*-MnSb) and wurtzite (*w*-MnSb)] phases found in experiment. The unit cell of these structures are displayed in the Fig. 1.3. It is clearly shown that the layer stacking of *n*-MnSb is "ABAC" along [0001], where Sb anions occupy two different crystal sites of the alternating "B" and "C". Therefore, Mn and Sb

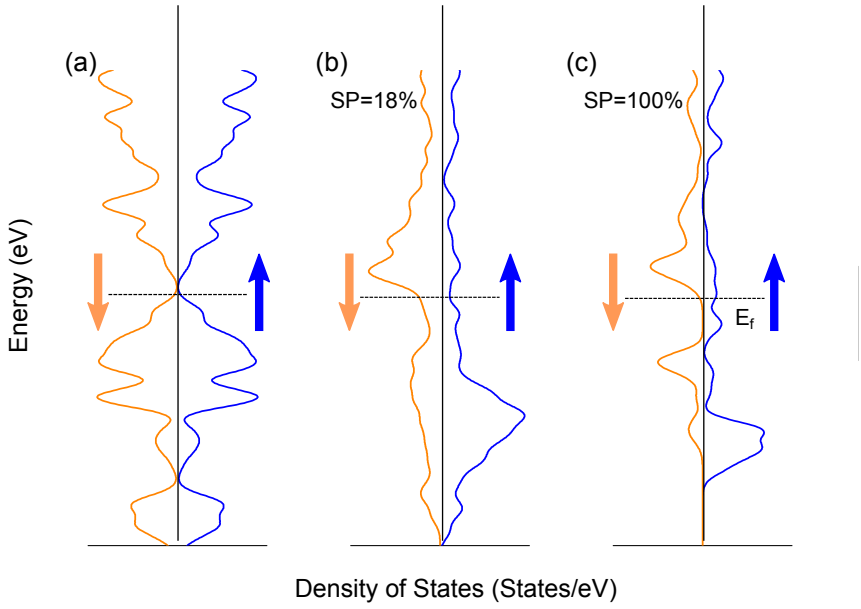

Figure 1.2: Density of states (DOS) for three representative materials (a) semiconductor (GaAs), (b) ferromagnet (n-MnSb), and (c) half-metallic ferromagnet (c-MnSb)

form the trangular prism bonding environment called trigonal prismatic structure, namely, each Sb atom has six neighbouring Mn atoms bonded. Figure 1.3 also shows the strained MnSb with zinc-blended (c-MnSb) and tetragonal structures (w-MnSb), respectively. Lattice parameters, space group and magnetic moment per Mn atoms of three MnSb polymorphs are listed in Table 1.1. Some DFT results indicate that c- and w-MnSb are half-metallic with the magnetic moment per Mn atom of 4 μ_B [40].

Since this thesis intensively presents the electronic properties of c-MnSb and n-MnSb polymopies, molecular orbital energy level diagrams and orbital configurations of tetrahedral (cubic) and trigonal prismatic (hexagonal) structures of MnSb are mainly described here as shown in Fig. 1.3(b,c). It is well-known that there is no s-orbital involved in the hybridisation for both of them [41]. Therefore, only d-orbitals [five electrons from Mn atoms ($3d^5 4s^2$)] and p-orbitals [three electrons from Sb atoms ($5s^2 5p^3$)] which are concerned with the p-d hybridisations are displayed in Fig. 1.3. In addition, the d-orbital is originally split into two energetically separate orbitals, namely, a three-fold t_{2g} (d_{xy}, d_{yz}, and d_{xz}) and a two-fold e_g degenerate state ($d_{x^2-y^2}$ and d_{z^2}). In the tetrahedral structure, e_g has the lower energy states

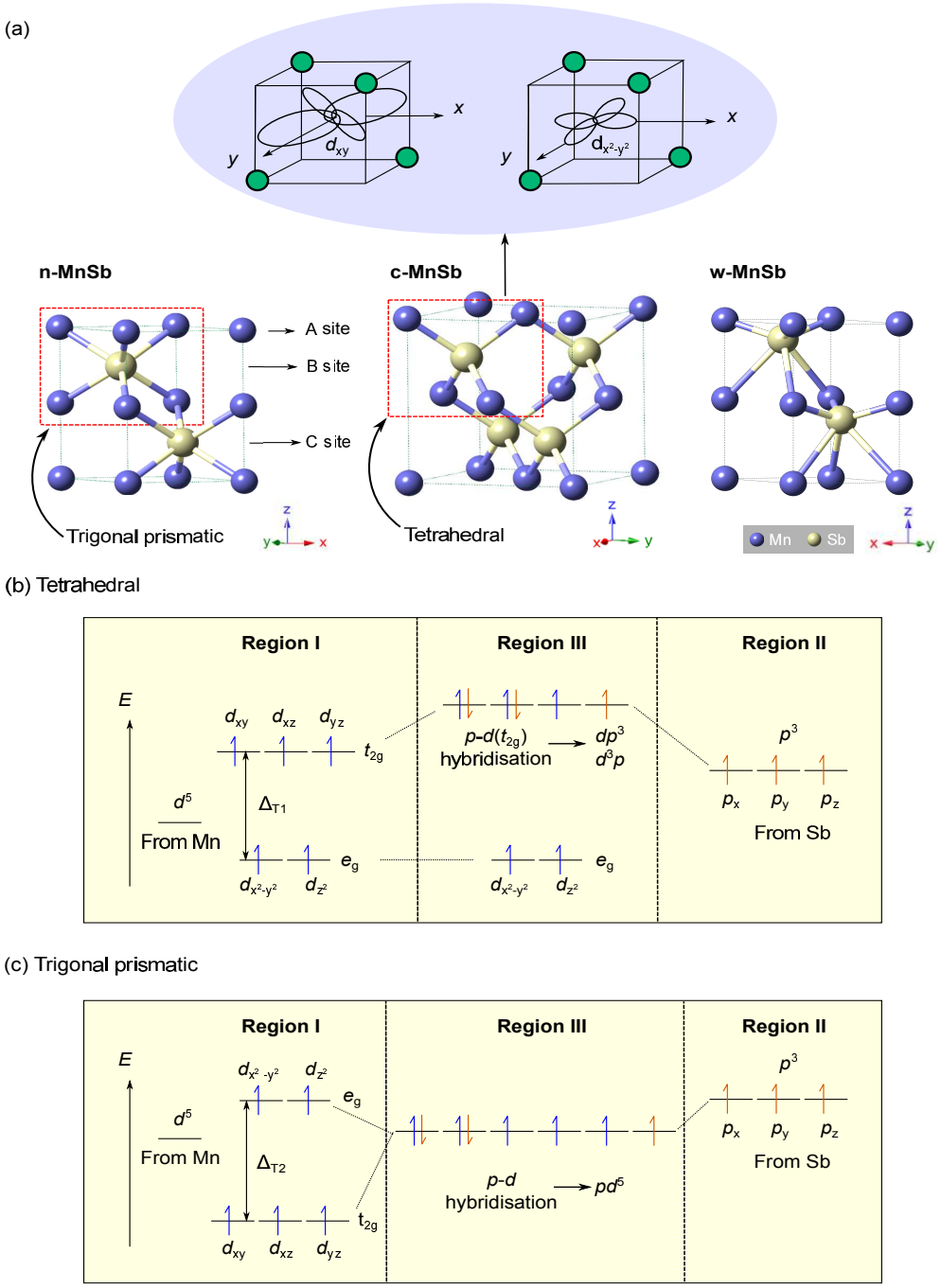

Figure 1.3: (a) Atomic bonding coordinates of n-MnSb, c-MnSb and w-MnSb. The purple (yellow) sphere represents Mn (Sb) atom. The areas in n-MnSb and c-MnSb structures (denoted by the red-dashed boxes) stand for the trigonal prismatic and tetrahedral geometry, respectively. The spatial orientation of d_{xy} and $d_{x^2-y^2}$ orbitals are illustrated in the tetrahedral structure of c-MnSb. (b) and (c) are schematic energy level diagrams for the tetrahedral (c-MnSb) and trigonal prismatic structures (n-MnSb). The Region I and II are the area of the orbital configuration before hybridisation of the d and p orbitals. Δ_{T1} and Δ_{T2} are the energy difference between t_{2g} and e_g orbitals in tetrahedral and trigonal prismatic structures. The up-and-down arrows represent the spin-up and -down of electrons deriving from Mn (blue) and Sb (orange) atoms.

Table 1.1: Structural parameters and magnetic moment per Mn atom of three polymorphs for MnSb calculated from other works.

Species	structure	Lattice parameters (Å)		Space group	Magnetic moment
		$\boldsymbol{a}$	$\boldsymbol{c}$		μ_B
n-MnSb	Niccolite	4.120	5.673 [40]	P63/MMC, *no.* 194	3.48 [40]
c-MnSb	Cubic (zinc-blende)	6.19	6.19 [44]	F-43M, *no.* 216	4 [40]
w-MnSb	Wurtzite	4.380	7.020 [45]	P63MC, *no.* 186	4 [40]

compared to t_{2g} orbitals, while the energy level configuration of e_g and t_{2g} is opposite in trigonal prismatic structure. It has been reported that the p-d hybridisation schemes are produced by p^3d/pd^3 for tetrahedral and by pd^5 for trigonal prismatic structures [42]. As the local tetrahedral environment only allows the hybridisation between the Mn-d t_{2g} and Sb-p orbitals due to a short distance between t_{2g} and p [d_{xy} and p shown in the inset of Fig. 1.3(a)], four newly formed hybridised t_{2g} and p orbitals are considered and shown in Region II in Fig. 1.3(b). There is no orbital interaction between e_g ($d_{x^2-y^2}$) and p orbitals due to a far distance of the orbitals as shown in the inset of Fig. 1.3(a). It is clear that c-MnSb has four net spin-up states, which is proved by the observed magnetic moment of 4 μ_{B} in Table 1.1. However, both of t_{2g} and e_g orbitals have to be involved for the required pd^5 hybridisation. Even though it has four unpaired electrons left, the magnetic moment cannot achieve 4 μ_{B} because of the more complex hybridisation. It should be noted that the high-spin configurations of d orbitals in Region I [Fig. 1.3(b,c)] are considered due to the 5 μ_{B} magnetic moment of Mn^{2+}/Mn^{3+} [43]. Namely, the spin-pairing energy, P, is larger than Δ_{T1} and Δ_{T2} (P is the increased energy when an electron is added to an occupied orbital).

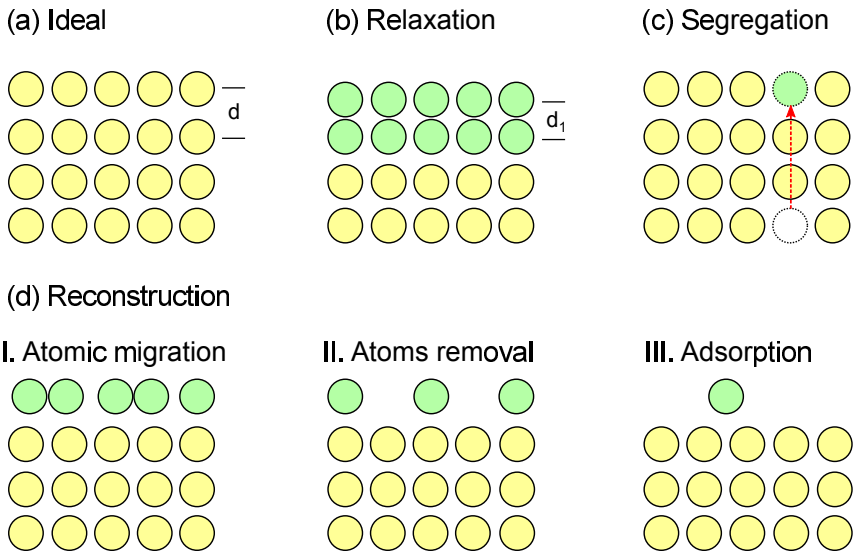

Figure 1.4: The illustration of possible defects which can accur at surfaces. (a) the periodical repeating unit in a ordered array, (b) relaxation (here, $d_1 < d$), (c) segregation, and (d) reconstruction.

1.6 Surface defective states

In practice, the surface can be regarded as a specific kind of defect which destroys the three dimensional periodic environment and results in the surface of crystal assuming significant differences with the bulk properties. In other words, due to dangling bonds, atomically truncated surfaces are energetically less stable, which yields some special surface reactions by either rearranging itself or interacting directly with external matter [*e.g.* surface relaxation, reconstruction, and segregation (shown in Fig. 1.4)]. Hence, surface science has become an inherently attractive and essential aspect in both physical and chemical fields of materials studies.

- Surface relaxation

Relaxation is a subtle realignment of the surface layers which may nevertheless have drastic effects on system energy variation, and seems to be more ordinary for metal surfaces. It mainly highlights the adjustments in the layer spacings perpendicular to the surface instead of the distances parallel to the surface. Figure 1.4(b) shows a contraction instance of the first interlayer, namely, the first layer of atoms has a slight movement towards the second surface layer driven by a set

of imbalanced forces at the surface. Normally, the surface relaxations are found to take place in the first few layers with alternating-sign relaxations in the consecutive layers. A typical example is Al(110) surface at which the relaxations are -8.6 %, +5.0 % and -1.6 % measured by the LEED method [46].

- Surface reconstruction

Unlike surface relaxations, the physical phenomena of reconstruction contains a change in the periodicity of the surface structure. A reconstruction can influence one or more surface layers, and can either conserve the total number of atoms of one layer [a conservative reconstruction, one case is shown in Fig. 1.4(c)-(I), where two atoms are attracted together as pairs formed dimers] or have a greater/lesser number than in the bulk [a non-conservative reconstruction, a specific example with missing rows of atoms is shown in Fig. 1.4(c)-(II)]. Reconstructions can be also caused by the adsorption of alien atoms onto the surface illustrated in Fig. 1.4(c)-(III), and the adsorbed locations are preferentially near to high symmetry sites on the surface. The adsorption-induced reconstructions can be categorised as weak physisorption through van der Waals interactions and stronger chemisorption through the formation of chemical bonds between the substrate and adsorbate atoms.

- Surface segregation

Surface segregation refers to the enrichment of an alloy constituent at the surface as a result of diffusion of that element from the bulk to the surface region [seen Fig 1.4(b)]. The driving force of segregation is the difference of chemical potential of given component between the surface and the bulk.

1.7 Wood notation

There are two primary approaches in the description of surface superlattice structures. One is the matrix notation, proposed by Park and Madden in 1968 [47]. The other is Wood's notation, which is the simplest and most effective method to be used [48].

- The matrix notation

The reconstructed surface unit vectors ($\boldsymbol{a}'$, $\boldsymbol{b}'$) together with substrate unit vectors ($\boldsymbol{a}$, $\boldsymbol{b}$) can be written as:

$$\begin{aligned} \boldsymbol{a}' &= G_{11}\boldsymbol{a} + G_{12}\boldsymbol{b} \\ \boldsymbol{b}' &= G_{21}\boldsymbol{a} + G_{22}\boldsymbol{b} \end{aligned} \tag{1.2}$$

or

$$\begin{pmatrix} \boldsymbol{a}' \\ \boldsymbol{b}' \end{pmatrix} = G \begin{pmatrix} \boldsymbol{a} \\ \boldsymbol{b} \end{pmatrix}. \tag{1.3}$$

Then, the matrix coefficients G is used to describe the surface reconstruction.

$$G = \begin{pmatrix} G_{11} & G_{12} \\ G_{21} & G_{22} \end{pmatrix}. \tag{1.4}$$

This is a more general and powerful system which can be applied to all ordered overlayers.

- The Wood notation

Wood notation determines a definition of the ratio of the lengths between the overlayers vectors ($\boldsymbol{a}'$, $\boldsymbol{b}'$) and substrate unit cell ($\boldsymbol{a}$, $\boldsymbol{b}$) including the rotated angle, which is referred to:

$$M_{(hkl)}\,(m \times n) - R\phi^{\circ} \tag{1.5}$$

or

$$M_{(hkl)}\,(m \times n)\,R\phi^{\circ}. \tag{1.6}$$

Here, (hkl) stands for the direction of the crystal M; $'m'$ and $'n'$ are the proportionality coefficient of $\boldsymbol{a}'$ and $\boldsymbol{a}$, $\boldsymbol{b}'$ and $\boldsymbol{b}$, respectively; ϕ is the angle of surface unit cell rotating with the underlying substrate in an anticlockwise direction.

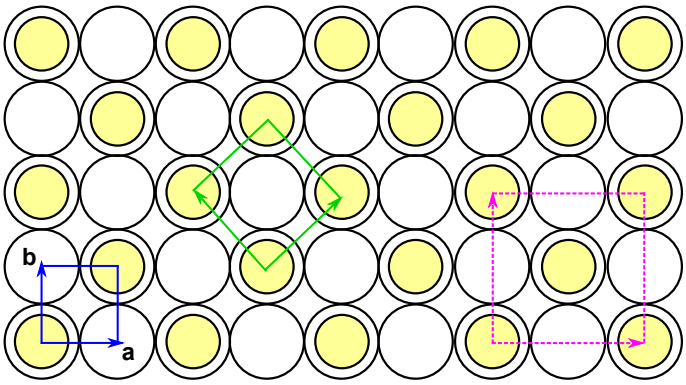

Figure 1.5: Some examples used to illustrate here by Wood and Matrix notation

Some visual examples of surface reconstruction are illustrated in Fig. 1.5. The smallest one (blue square) is the basis vector being aligned with the substrate basis vectors, then solid green line can be described as $(\sqrt{2} \times \sqrt{2})R45°$ (Wood notation) or $G = \begin{pmatrix} 1 & 1 \\ -1 & 1 \end{pmatrix}$ (matrix notation). In the same way, the dotted one can be written as (2×2) *and* G=$\begin{pmatrix} 2 & 0 \\ 0 & 2 \end{pmatrix}$ using wood and matrix notation, respectively. In this situation, there is no rotation between substrate and surface, so the angle should be dropped in the Wood notation format.

1.8 Convention for labelling crystallographic directions

In hexagonal structures, using the conventional three index notation readily leads to ambiguity. For example, figure 1.6(a) shows one case that the $[1\bar{1}0]$ direction is symmetrically equivalent to [120] but inequivalent to [110], which should be the other way around based on the literal expressions. Therefore, in order to eliminated such confusions, a four-index Bravais-Miller system is required to be used. In this scheme, four indices $(hkil)$ satisfy the constraint of $h+k+i = 0$, where h, k and l are corresponding to Miller indices, and i is an ostensibly redundant index. However, the similarity of highly symmetrical directions [such as the ones labelled in Fig. 1.6(b)] will have the same indices permutation when the redundant index is added (*i.e.* they are symmetrically equivalent $[01\bar{1}0] \approx [10\bar{1}0] \approx [1\bar{1}00] \approx [0\bar{1}10] \approx [\bar{1}010] \approx [\bar{1}100]$).

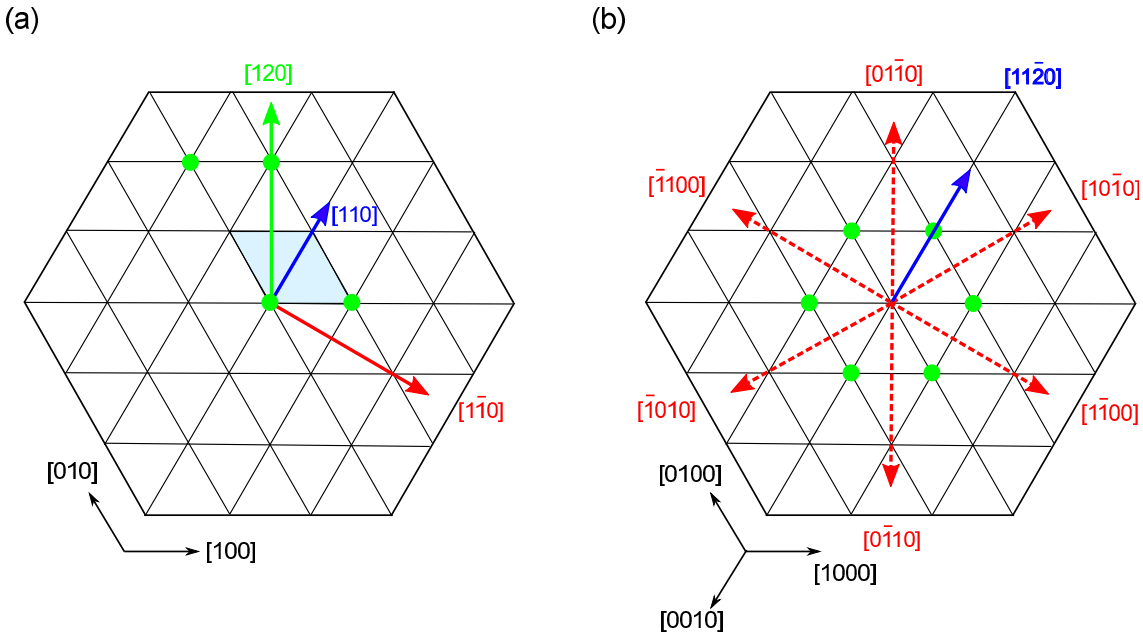

Figure 1.6: Crystallographic orientations in hexagonal lattices using (a) 3-index and (b) 4-index notations. The blue filled area represents the bulk-truncated (1×1) surface. The region enclosed by six green points in Fig. 1.6(b) is basal plane, which remains unchanged by a rotation of 120°.

1.9 Epitaxial growth and strain in thin films

Epitaxy is the deposition of single crystal films on a single crystal substrate/underlying layer with atomic precision. Subsequent development of a particular crystallographic orientation of the films is made along the crystal structure and in-plane lattice spacing of the substrate/underlying layer as the thin film grows. The epitaxy can be mainly classified into two fundamental types: homoepitaxy (a crystalline film grows on the substrate of the identical materials) and heteroepitaxy (both the crystalline film and the substrate are of dissimilar materials).

The degree of lattice mismatch between the film and the substrate can be defined as

$$\epsilon = \frac{a_{\mathrm{s}} - a_{\mathrm{f}}}{a_{\mathrm{f}}}. \tag{1.7}$$

where a_{s} (a_{f}) are the lattice parameter of the film (substrate). In homoepitaxial systems, there is no lattice mismatch between the thin film and the substrate. The homoepitaxy of thin film growth in a vacuum chamber is entirely dependent on growth

parameters such as temperature and ambient gas. In the case of heteroepitaxy, biaxial strain, ε, usually occurs due to a lattice mismatch at the overlayer/substarte interface (in general, less than 5 % [49]). Therefore, thin films are strained ($a_{\mathrm{s}} < a_{\mathrm{f}}$ or $\epsilon < 0$) or stretched ($a_{\mathrm{s}} > a_{\mathrm{f}}$ or $\epsilon > 0$) along the in-plane of thin films to match the dissimilar substrate. The elastic strain energy arising from the lattice mismatch, together with the energy due to the formation of a new interface are called interface energy (σ_{Inter}). It should be noted that, during thin film growth, minimising such an interface energy plays a crucial role in the variation in the growth mode, composition, and crystal structure of thin films.

Here, there are three different growth modes of thin film formation below:
(i) Frank-Van der Merwe Growth (a layer by layer growth): $\sigma_{\mathrm{Sub}} \geqslant \sigma_{\mathrm{Film}} + \sigma_{\mathrm{Inter}}$,
(ii) Volmer-Weber Growth (an island growth): $\sigma_{\mathrm{Sub}} < \sigma_{\mathrm{Film}} + \sigma_{\mathrm{Inter}}$,
(iii) Stranski-Krastanov Growth (a mixed growth mode): initially, $\sigma_{\mathrm{Sub}} \geqslant \sigma_{\mathrm{Film}} + \sigma_{\mathrm{Inter}}$; finally, $\sigma_{\mathrm{Sub}} < \sigma_{\mathrm{Film}} + \sigma_{\mathrm{Inter}}$.
where σ_{Sub}, σ_{Film}, and σ_{Inter} are the substrate, film surface and interface energies, respectively.

Chapter 2

Theoretical techniques

2.1 Density functional theory (DFT)

2.1.1 Earlier approximations

First-principles, or ab initio, is a basic and foundational method to understand the properties of materials by solving the Schrödinger Equation (SE), $\widehat{H}\psi = E\psi$ [50]. However, in the mathematical calculations it inevitably produce a big challenge to deal with complex many-body problems so that some approximations have to be introduced to simplify calculation procedures. This does not mean first-principles lose its real intention. In order to exert theoretical simulations to practice, making as few approximations as possible to attain the results close to the truth is the key idea. In the following part, some great triumphs of identifiable approximation treatments will be assumed.

The advancement of quantum mechanics has been considered as the potential tool to solve the SE, in which the main observation of applying quantum chemistry to atoms is the outer-shell electrons respond much more rapidly to changes in their circumstance than nuclei can owing to their lighter masses, *i.e.* the Born-Oppenheimer approximation [51]. Therefore, the SE can be subsequently divided into two parts on the basis of the position-fixed atomic nucleus and the moving electrons:

$$\begin{aligned}\widehat{H}\psi\left(\mathbf{r}_1...\mathbf{r}_N\right) &= E\psi\left(\mathbf{r}_1...\mathbf{r}_N\right) \\ &= \left[-\frac{\hbar^2}{2\mathrm{m}}\sum_{i=1}^{N}\nabla^2 + \sum_{i=1}^{N}V\left(\mathbf{r}_i\right) + \sum_{i=1}^{N}\sum_{j<i}U\left(\mathbf{r}_i,\mathbf{r}_j\right)\right]\psi\left(\mathbf{r}_1...\mathbf{r}_N\right). \quad (2.1)\end{aligned}$$

Here, $\widehat{H}$ is Hamiltonian operator composed of three terms, *i.e.* kinetic energy of electrons, the interaction energy between electrons and the atomic nuclei, and the interaction energy between electrons, respectively; m and $\hbar$ are the mass of electrons

and reduced Planck constant ($\hbar = h/2\pi$); $\psi(\mathbf{r}_1...\mathbf{r}_N)$ is the electronic wave function that is a function of the spatial coordinates of each of N electrons. E is the lowest energy configuration, or ground state, of the electrons which provides a precise quantum description of the physical behaviour of materials. In addition, the ground state is stationary state independent of time, so the SE here has no influence of time, namely so-called time-independent Schrödinger Equation. The form in Equ. 2.1 has also neglected electron spin. This separation of the nuclei and electrons immensely simplify the calculations in the course of solving the SE.

However, exorbitant computational demands are still needed simply because a single atom can normally carry more than one electron plus each electron inherently has three-dimensional wave function. For example, if we are interested in a nannocluster of 100 Pt atoms, the full wave function will require more than 23,000 dimensions [52]. This number suggests how difficult solving such a complicated Schrödinger equation is. Density functional theory (DFT) sidesteps this problem by reducing the complexity of the problem in a theoretically justified way. The crucial progress of DFT occurred in 1964 when the Hohenberg-Kohn theorem (elementary mathematical theorems) [53] and Kohn-Sham approximation (a set of equations) [54] emerged. As the name suggests, the fundamental physical quantity of density functional theory is represented by the charge density instead of electronic wave functions. By considering that, the number of degree of freedom can be reduced to only three spatial coodinations of charge density at a particular position. Consequently, the N-electron problem is transformed into N one-electron systems where the interactions between electrons is expressed by an effective exchange-correlation potential. The huge successes of DFT implementation have been reviewed by Walter Kohn in his chemistry Nobel prize lecture in 1999 [55].

2.1.1.1 Hohenberg-Kohn theorem

Due to the electrons' indistinguishability, the status of individual electrons become less important than the probability density $[\psi^*(\mathbf{r}_1...\mathbf{r}_N)\,\psi(\mathbf{r}_1...\mathbf{r}_N)]$ of N electrons at a particular set of coordinates, $\mathbf{r}_1...\mathbf{r}_N$. The closed quantity with prob-

ability is electron density,

$$n(\mathbf{r}) = 2\sum_{i=1}^{N} \psi^{*}(\mathbf{r})\,\psi(\mathbf{r}), \tag{2.2}$$

where the summation denotes all electron wave functions that are occupied by electrons; The factor of 2 means each electron wave function can be occupied by two separate electrons with different spins, namely, $n(\mathbf{r})$ includes two parts of $n_{\uparrow}(\mathbf{r})$ and $n_{\downarrow}(\mathbf{r})$. In order to clarify the descriptions, $n(\mathbf{r})$ will be only shown in the rest of the thesis.

From this point of view, Hohenberg and Kohn proposed two theorems (HK theorem) which are described as follows:

1. The ground-state energy, $E[n(\mathbf{r})]$, from Schrödinger's equation is a unique functional of the electron density.

2. The electron density, $n(\mathbf{r})$, that minimizes the energy of the overall functional is the true electron density corresponding to the full solution of the Schrödinger equation.

The first theorem demonstrates that there is a one-to-one mapping between the ground states wave function and the ground states electron density. Then, the complicated problems of solving the Schrödinger equation by finding the wave function of 3N variables can be easily transferred to an alternative way by searching the electron density distribution of three spatial variables. Unfortunately, although this is an unprecedented breakthrough, this theorem does not hint what the functional actually is. Subsequently, the second Hohenberg-Kohn theorem gives a decisive definition of the functional. The resultant Schrödinger equation is re-written by:

$$\begin{aligned} E(\psi_i) &= \left[-\frac{\hbar^2}{2\mathrm{m}}\sum_i \int \psi_i^{*}\nabla^2 d^3\mathbf{r} + \int V(\mathbf{r})\,n(\mathbf{r})\,d^3\mathbf{r} + \int V_H(\mathbf{r})\,n(\mathbf{r})\,d^3\mathbf{r}\right] + [E_{\mathrm{XC}}(\psi_i)] \\ &= [E_{\mathrm{known}}] + [E_{\mathrm{unknown}}]\,. \end{aligned} \tag{2.3}$$

The terms on the right are, in order, the kinetic energies of electrons, the Coulomb interactions between the electrons and the nuclei, the Coulomb interactions among electrons ($[E_{\text{known}}]$ term). The last term stands for the exchange-correlation energy, $[E_{\text{XC}}(\psi_i)]$ defined as $[E_{\text{unknown}}]$ term, which arises from the special concept of indistinguishability of identical particles in the quantum world. A more detailed description will be given in the Sec. 2.1.1.3.

There are two obvious simplification from Eqs. 2.1 to 2.3. In addition to the introduction of $n(\mathbf{r})$, the Hartree approximation is also applied to SE that determined the wave function of a quantum many-body system by a single stationary state, *i.e.* $\psi(\mathbf{r}_1, \mathbf{r}_2 ... \mathbf{r}_N) = \psi(\mathbf{r}_1)\psi(\mathbf{r}_2)...\psi(\mathbf{r}_N)$. This condition is the foundation of the development of Kohn-Sham theory, although the mission of solving the SE is still to be attempted.

2.1.1.2 Kohn-Sham theory

The Kohn-Sham (KS) equation, the practical realisation of DFT used in codes, is similar to the SE in form. Rather than dealing with the intricate real system as described by Equ. 2.3, the solution of the KS equations focus on single-election wave functions that only rely on three spatial variables. That is to say KS equation is a reduced SE of a fictitious system created by non-interacting particles which generate the identical charge density as the given system with interacting particles. In the consequence, solving KS equation would be more accessible than coping with the SE in the majority of cases, thus making much larger systems tractable computationally.

The SE can be reformulated as follows:

$$\left[-\frac{\hbar^2}{2\mathrm{m}}\nabla^2 + V(\mathbf{r}) + V_{\mathrm{H}}(\mathbf{r}) + V_{XC}(\mathbf{r})\right]\psi_i(\mathbf{r}) = \epsilon_i\psi_i(\mathbf{r}) \tag{2.4}$$

Here, every term has the similar meanings with the relative ones in Equ. 2.3, just the KS equation misses the summations that are shown in SE Equ. 2.3. $V(\mathbf{r})$ is the potential energy from the external field of positively charged nuclei. $V_{\mathrm{H}}(\mathbf{r})$,

is called the Hartree potential correspond to the Hartree approximation mentioned above, that describes the Coulomb repulsion among electrons and defined by

$$V_{\mathrm{H}}(\mathbf{r}) = e^2 \int \frac{n(\mathbf{r}')}{|\mathbf{r} - \mathbf{r}'|} d^3\mathbf{r}'. \tag{2.5}$$

It should be emphasised that the Hartree potential generated by the interaction between electrons also includes the self-interaction contribution. The part of $V_{\mathrm{H}}(\mathbf{r})$, therefore, contains a Coulomb interaction between the electron and itself [*i.e.* self − consistent field (SCF)]. This SCF operation is considered to be no physics meaning, and the relevant correction of it is one of a few effects which has already been dragged into the final potential, $V_{XC}(\mathbf{r})$, which defines the exchange and correlation potential:

$$V_{\mathrm{XC}}(\mathbf{r}) = \frac{\delta E_{\mathrm{XC}}(\mathbf{r})}{\delta n(\mathbf{r})}. \tag{2.6}$$

So far DFT has been presented in a formal mathematical framework, but the specific use of it in the physics context has to further require the more effecient approximations of exchange-correlation funcion, $E_{\mathrm{XC}}[n(\mathbf{r})]$.

2.1.1.3 Exchange-correlation function

The forms of the exchange-correlation function can be divided into numerous categories such as local density approximation (LDA), generalised gradient approximation (GGA), meta-GGA and hybrids, all of which provide slightly different treatments of $E_{\mathrm{XC}}[n(\mathbf{r})]$. Since LDA and GGA are commonly used, they will be introduced here.

- Local density approximation (LDA)

This approximation is the simplest and the most serviceable method in the functional classes. The core of LDA is that the electron density is viewed as a constant at all points in space: a uniform electron gas [54], $n(\mathbf{r}) = \text{constant}$, which

offers feasible means to virtually utilise KS equations. Because this approximation employs the local density to define the exchange-correlation functional, it is called local density approximation. Accordingly, the exchange-correlation energy is written as:

$$E_{\mathrm{XC}}^{\mathrm{LDA}}\left[n\left(\mathbf{r}\right)\right]=\int\epsilon_{\mathrm{XC}}^{\mathrm{electron-gas}}\left[n\left(\mathbf{r}\right)\right]d\mathbf{r}, \tag{2.7}$$

where $n\left(\mathbf{r}\right) = 2\sum_{i=1}^{N}\psi^{*}\left(\mathbf{r}\right)\psi\left(\mathbf{r}\right)$ has been mentioned in Sec. 2.1.1; $\epsilon_{\mathrm{XC}}^{\mathrm{electron-gas}}$ is the exchange-correlation energy per particle of a homogeneous electron gas of density n. The exchange-correlation energy can be decomposed into two terms : exchange part and correlation part, $E_{\mathrm{XC}} = E_{\mathrm{X}} + E_{\mathrm{C}}$. The exchange term is primary and given by [55],

$$\epsilon_{\mathrm{X}} = -\frac{0.458}{r}. \tag{2.8}$$

The correlation part was initially proposed by Wigner in 1938 [56],

$$\epsilon_{\mathrm{C}} = -\frac{0.44}{r+7.8}. \tag{2.9}$$

More estimations with a higher precisions have been continuously devised by Ceperley in 1978 [57]; Ceperley and Alder in 1980 using Monte Carlo methods [58]. The LDA method has been found to be implemented in a mathematical framework that can be effectively solved for the large numbers of atoms especially for metals and well-behaved covalent systems. However, it is widely accepted that LDA typically overestimates molecular bond energy, cohesive energies of solids, etc. and underestimates equilibrium atomic separations [59].

- Generalised gradient approximation (GGA)

Compared with the LDA, GGA includes more physical information, which adds the local gradient of the charge density as an independent variable. This

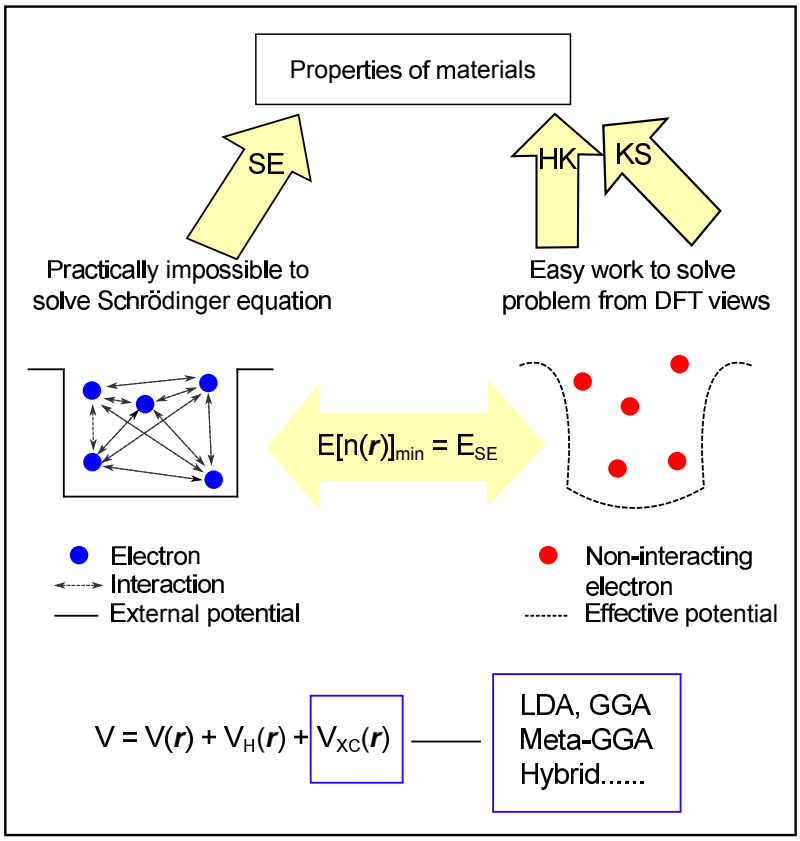

Figure 2.1: A sketch of quantum mechanics development process in the first-principles field

approach is more suitable for the situations where the density experiences swift changes. Symbolically this can be expressed by,

$$E_{\mathrm{XC}} = E_{\mathrm{XC}}\left[n\left(\mathbf{r}\right), \nabla n\left(\mathbf{r}\right)\right]. \tag{2.10}$$

This can result in a considerable improvement over LDA method in the accuracy of predicted energies and structures. The most generally used functionals of GGA are Perdew-Wang functional (PW91) [60] and Perdew-Burke-Ernzerhof functional (PBE) [61]. PBE is a simplified PW91 version, which produces almost identical numerical results such as lattice constants, bulk moduli, and atomisation energies with simpler formulas from simpler derivations and analytic forms. However, the large difference of calculating properties obtained by using PW91 and PBE arises

due to surface effects of material systems [62]. The PBE function has been utilised in this thesis. This is also recommended by CASTEP tutorials when on-the-fly pseudopotentials are required [63] (see section 2.1.2.4).

2.1.1.4 Summary of density functional theory

The main ideas of Sec. 2.1 as discussed above are illustrated in Fig 2.1 schematically. The segment on the left-hand side of this image stands for solving the SE. The right part is a more efficient approach to obtain the solutions using HK theorem and KS equations, which is equivalent to SE but simpler. Nevertheless, to simplify the calculation further, the exchange-correlation like LDA and GGA is used in the calculation.

2.1.2 Plane-wave pseudopetential methods

2.1.2.1 Introduce to CASTEP

One of the most successful software implementing DFT calculation is the Cambridge Serial Total Energy Package (CASTEP) programme, which was written by Prof M. C. Payne firstly and subsequently developed by University of Cambridge and other groups around the UK [64, 65]. CASTEP is based on density functional theory using plane wave pseudopetentials method to explore the microscopic properties ranging from total energy, band structure to density of states (DOS) of collections of atoms (*e.g.* crystalline solids, surfaces and interfaces, etc.) This approach allows researchers to inquire into the nature of a system without any demand of experimental input. In this context, a series of simulations can be carried on either to predict the properties of materials or to compare them with virtual experiments.

CASTEP was written to be highly portable by Fortran language, so it can run the simulations on all major platforms from a local PC to a supercluster. Additionally, it is also compiled in the Materials Studio software with a visualisation operational environment, which provides a comprehensive and user-friendly interface to model the three-dimensional periodic structures and exploit their quantum mechanics.

2.1.2.2 Bloch's theorem and plane wave basis sets

The quantum mechanical methods has resolved the many-body problem by using N one-electron approximation, however, there is still no mention of how to deal with practically infinite number of electrons over the entire space of a solid. Provided that ions are arranged in a highly ordered periodic crystal lattice, it is only necessary to concern the number of electrons within the unit cell. Bloch's theorem gives the form of a wave function for a particle in a periodically-repeating environment. By using this theorem, the form of the wave function of the infinite crystal can be written in terms of wave functions at reciprocal space vectors of a Bravais lattice. Periodic boundary conditions satisfy:

$$\psi(\mathbf{r}) = \psi(\mathbf{r} + N_1\mathbf{a}_1);\ \psi(\mathbf{r}) = \psi(\mathbf{r} + N_2\mathbf{a}_2);\ \psi(\mathbf{r}) = \psi(\mathbf{r} + N_3\mathbf{a}_3), \tag{2.11}$$

where $\mathbf{a}_1,\ \mathbf{a}_2,\ \mathbf{a}_3$ are the primitive lattice vectors of three-dimentional crystal; $N_1,\ N_2,\ N_3$ are the number of primitive cell along the three basis vectors direction. The total number of primitive cell is $N = N_1N_2N_3$.

According to the transitional symmetry operation (T) of wave function,

$$\psi(\mathbf{r} + N_1\mathbf{a}_1) = T_1^{N_1}\psi(\mathbf{r}) = \lambda^{N_1}\psi(\mathbf{r}) = \psi(\mathbf{r}), \tag{2.12}$$

the Eigenvalue λ can be obtained $\lambda_1 = e^{2\pi i\frac{l_1}{N_1}}$, $\lambda_2 = e^{2\pi i\frac{l_2}{N_2}}$, $\lambda_3 = e^{2\pi i\frac{l_3}{N_3}}$ ($l_1,\ l_2\ and\ l_3$ are integer).

The new vector $\boldsymbol{k}$ is expessed as,

$$\mathbf{k} = \frac{l_1}{N_1}\mathbf{b}_1 + \frac{l_2}{N_2}\mathbf{b}_2 + \frac{l_3}{N_3}\mathbf{b}_3, \tag{2.13}$$

Here, $\mathbf{b}_1, \mathbf{b}_2, \mathbf{b}_3$ are reciprocal basis set, which has the relationship with real basis sets as $\mathbf{a}_i \times \mathbf{b}_i = 2\pi\delta_{ij}$ ($\mathbf{a}_i = \frac{l_i}{N_i}$).

Therefore, the wave function of translation $\mathbf{R}_m$ ($\mathbf{R}_m = m_1\mathbf{a}_1 + m_2\mathbf{a}_2 + m_3\mathbf{a}_3$) satisfies

$$\begin{aligned}\psi(\mathbf{r}+\mathbf{R}_m) &= T(m_1\mathbf{a}_1+m_2\mathbf{a}_2+m_3\mathbf{a}_3)\,\psi(\mathbf{r}) \\ &= T(m_1\mathbf{a}_1)\,T(m_2\mathbf{a}_2)\,T(m_3\mathbf{a}_3)\,\psi(\mathbf{r}) \\ &= T_1^{m_1}T_2^{m_2}T_3^{m_3}\psi(\mathbf{r}) \\ &= \lambda_1^{m_1}\lambda_2^{m_2}\lambda_3^{m_3}\psi(\mathbf{r}) \\ &= e^{i\mathbf{k}\bullet(m_1\mathbf{a}_1+m_2\mathbf{a}_2+m_3\mathbf{a}_3)}\psi(\mathbf{r}) \\ &= e^{i\mathbf{k}\bullet(\mathbf{R}_m)}\psi(\mathbf{r})\,. \end{aligned} \tag{2.14}$$

The Bloch wave is expressed as

$$\psi_{\mathbf{k}}(\mathbf{r}) = e^{i\mathbf{k}\bullet\mathbf{r}}\mu_{\mathbf{k}}(\mathbf{r})\,. \tag{2.15}$$

Here, $e^{i\mathbf{k}\bullet\mathbf{r}}$ and $\mu_{\mathbf{k}}(\mathbf{r})$ are wavelike part and the periodic wave function with the same periodicity as the crystal lattice, respectively. Namely, Bloch wave can be divided into two parts: a plane-wave and a periodic function. The $\mu_{\mathbf{k}}(\mathbf{r})$ term can be expanded by means of spatial frequency:

$$\mu_{\mathbf{k}}(\mathbf{r}) = \sum_{\mathbf{G}} c_{\mathbf{G}} e^{i\mathbf{G}\bullet\mathbf{r}}. \tag{2.16}$$

Here, $\mathbf{G}$ are vectors in the reciprocal space $\mathbf{G} = n_1\mathbf{b}_1+n_2\mathbf{b}_2+n_3\mathbf{b}_3$ along with integer value for n_i. The sum of $c_{\mathbf{G}}$ is the reciprocal lattice vectors or $\mathbf{G}$-vectors.

Combining Eqs. 2.15 and 2.16 above gives:

$$\psi_{\mathbf{k}}(\mathbf{r}) = \sum_{\mathbf{G}} c_{(\mathbf{k}+\mathbf{G})} e^{i(\mathbf{k}+\mathbf{G})\bullet\mathbf{r}}, \tag{2.17}$$

$e^{i(\mathbf{k}+\mathbf{G})\bullet\mathbf{r}}$ is called plane wave basis sets, obviously, the wave functions can be described conveniently using basis sets. Hence, the nonlinear KS equation is able to be solved by representing the electronic wave functions by a linear combination of a set of basis functions.

2.1.2.3 K-points sampling and energy cutoff

- Cutoff energy

In principle, Fourier series is still infinite, nevertheless, Equ. 2.18 has the corresponding expression of kinetic energy

$$E_c = \frac{\hbar^2}{2\mathrm{m}} \left|\mathbf{k} + \mathbf{G}\right|^2 . \tag{2.18}$$

The energy cut-off is for determining the number of plane waves in the basis set, therefore, the increasing cut-off energy can result in the number of plane waves rising, which will promote the accuracy of results at the cost of more computational resources. In order to truncate the infinite sum into available optimal number of wave functions, the cutoff energy can be described as:

$$E_{\mathrm{cutoff}} = \frac{\hbar^2}{2\mathrm{m}} \mathbf{G}^2_{\mathrm{cutoff}}. \tag{2.19}$$

The energy cut-off is usually tested by evaluating the total energy difference when the cell size varies during the geometry optimisation. As long as the enhancement of the number of wave functions does not increase the value of charge density, the energy differences will remain the same.

- ***k***-point sampling

The wave functions would still be infinite because the number of ***k*** vectors can be set in a very dense way no matter how small the plane wave energy cut-off was selected. Hence, an essential shortcut arises when there is little change in $\psi_{\boldsymbol{k}}(\mathbf{r})$ with increasing ***k***-points, which means one calculation can be achieved at a finite number of ***k***-points. The idea of employing a manageable finite number of ***k***-points to sample the Brillouin zone is called ***k***-point sampling. The most famous method is developed by Monkhorst and Pack in 1976 to choose the appropriate ***k***-points [66].

The number of such ***k***-points demands to precisely determine the total energy is dependent on a few factors:

- The size of supercell: A larger supercell with a smaller reciprocal lattice requires fewer $\boldsymbol{k}$-points. More specifically, for a surface slab accompanied by large lattice parameter in the direction perpendicular to the surface, a single $\mathbf{k}_z$ value is generally sufficient.

- The species of materials: Metallic systems commonly require much denser $\boldsymbol{k}$-points than semiconducting or insulating systems to prevent potential probability of incorrect bands being occupied near the Fermi level.

- Symmetry of the system: a set of equivalent $\boldsymbol{k}$-points in reciprocal space have the same band energies, therefore, only a single $\boldsymbol{k}$-point is needed in the calculations. This symmetry-related reduction in the number of $\boldsymbol{k}$-points offers a direct computational speedup and accordingly save computing resources.

2.1.2.4 Pseudopotentials

It is well known that many physical features of materials are determined by more active valence electrons at the outermost layer rather than inner-shell electrons that are tightly bounded by nuclei. This facilitates the development of pseudopotential approximations. The specific treatment is that a new and effective potential will be constructed to take place of the atomic all-electron potential so that the potentials of inert core electrons and strong nuclear are eliminated and the valence electrons are described by a pseudo-potentional. In this method, only the chemically active valence electrons are considered in detail, whereas the core electrons are "frozen" being regarded along with the nuclei as fixed ion cores. Seen from Fig. 2.2, there is an identical trend between all electrons potential and pseudopotential beyond the region of $\mathbf{r}_c$, where $\mathbf{r}_c$ is the cutoff radius, which corresponds to the cutoff energy.

This approximation improves the convergence time and reduce the load of calculation immensely, however, the selection of pseudopotentials will influence the accuracy of calculations to large extent. Thus the choice of pseudopotentials needs to be matched to the material system.

The first application is the norm-conserving pseudopotential, which normally

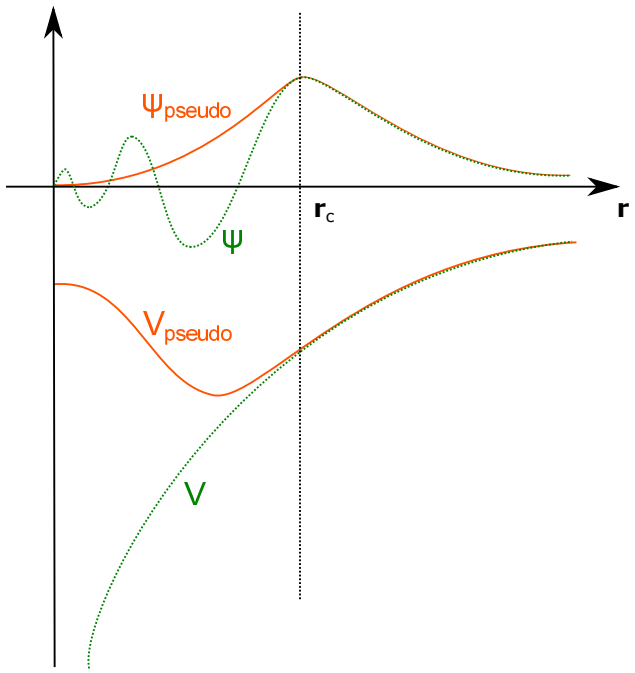

Figure 2.2: An illustration of the wave function (green curves) and potential (orange curves) of all electrons (dot lines) and pseudo electrons (solid lines). The all-electrons and pseudo electrons values are same above a the cut-off radius $\mathbf{r}_c$.

requires relatively large basis sets and high cutoff energy especially for transition metals and first-row elements [67, 68].

Norm-conserving pseudopotentials require two conditions:

1. The "*norm*" of every pseudo-wavefunction being the same with its corrsponding all-electron wavefunction below the cut-off radius $\mathbf{r}_c$ [69]:

$$\int_{\mathbf{r}<\mathbf{r}_c} d\mathbf{r}^3 \psi_{R,\mathbf{i}}(\mathbf{r})\,\psi_{R,\mathbf{j}}(\mathbf{r}) = \int_{\mathbf{r}<\mathbf{r}_c} d\mathbf{r}^3 \widetilde{\psi}_{R,\mathbf{i}}(\mathbf{r})\,\widetilde{\psi}_{R,\mathbf{j}}(\mathbf{r})\,, \tag{2.20}$$

where $\psi_{R,\mathbf{j}}$ and $\widetilde{\psi}_{R,\mathbf{j}}$ are wave function of all-electron and pseudo states on atom R.

2. Pseudo and all-electron wavefunctions are same beyond the cut-off radius $\mathbf{r}_c$.

In the following, ultrasoft pseudopotentials (USPPS) were designed by Vanderbilt to be carried out with the lowest possible cutoff energy [70, 71], which has the merit of making calculations of d- and f-orbital electron metals possible at an

admissible computation cost. Normally, pseudopotentials computationally requiring higher energy cutoff are called "*hard*", whereas more effective pseudopotentials with lower cutoff energy demands are "*soft*". As the name suggests, USPPs require substantially lower cutoff energy than other methods, so they have been widely employed so far. Recently, a non-local core correction was developed to describe spin-polarized states of the first row atoms in the periodic table of elements such as oxygen [72] and nitrogen correctly [73]. Previous researches ignored this effect for a long time, however, it is extremely important for predicting the magnetic properties of materials precisely.

Additionally, CASTEP code has its own build-in generator so that it can compute pseudopotentials on the fly during a calculation (the so-called on-the-fly pseudopotentials). This way can be effectively utilised to change the default core radius, thereby creating a softer (bigger core radius) or a more accurate and hard (smaller core radius) version of a pseudopotential for a considered element. The current set of the on-the-fly settings has been advanced to minimise an error by well converged all-electron DFT calculations. The error achieved by this set is 0.5 meV/atom, and its physics interpretation is provided by Lejaegher et al [74]. Hence, the calculations are more accurate compared with obtaining the pseudopotential from the database.

2.1.2.5 Solving Koh-Sham equation in CASTEP programme

CASTEP has two main approches to solve the Kohn-Sham equations: density mixing (DM) and ensemble density functional theory (EDFT).

- Density mixing (DM)

Instead of attempting to calculate the ground-state wave functions and density contemporaneously, DM method firstly compute the KS wave functions for a given input density, in the following, an independent algorithm of "*density mixing*" is employed to continue to calculate an estimate of the ground-state density. This estimate is then used as the input density for a new iteration. The algorithm continues till the estimated ground-states is closed to the real ground-state.

- Ensemble density functional theory (EDFT)

The density in this scheme is always updated no matter when the wavefunctions are changed and the variation is only allowed when the total energy is lowered by it. This approach is compeletely variational and thus robust but slow.

2.1.3 Geometry optimisation

The first job of any calculation employing the CASTEP programme is running geometry optimisation (also called energy minimisation or geometry minimisation). The essence of geometry optimisation is to derive the most stable atomic configuration using an iterative method, in which atomic position and possible lattice parameters will be changed until the magnitude of forces and total energy drop below defined convergence tolerances, thereby obtaining the minimal total energy. Normally, geometry optimisation leads to an ideal atomic arrangement according to their relative chemical bonding characteristics, which will minimise forces that either pulling atoms together or pushing them apart. The significance of performing a geometry optimisation is because the correspondent structure is found in nature and used in experimental and other theoretical investigations. The Broyden-Fletcher-Goldfarb-Shanno (BFGS) algorithm is generally used as the fastest and most effective method to find the lowest energy structure in CASTEP [75].

For the optimisation of bulk, any internal structure including atomic positions and lattice parameters of the unit cell must be optimised together. However, the geometry optimisation of nonperiodic systems such as surfaces, defects and interfaces can fix their lattice parameter to only deal with the new atomic arrangements. In the case of surface and interface, we have to ensure the models have sufficiently thick bulk layers and a sufficient vacuum space.

2.1.3.1 The convergence and parameters test of bulk and surface

Optimisation task is a time-consuming process, so convergence test become extremely necessary to enhance the work efficiency using small supercells' calculation, and then the fixed parameters can be transferred to some larger systems so as

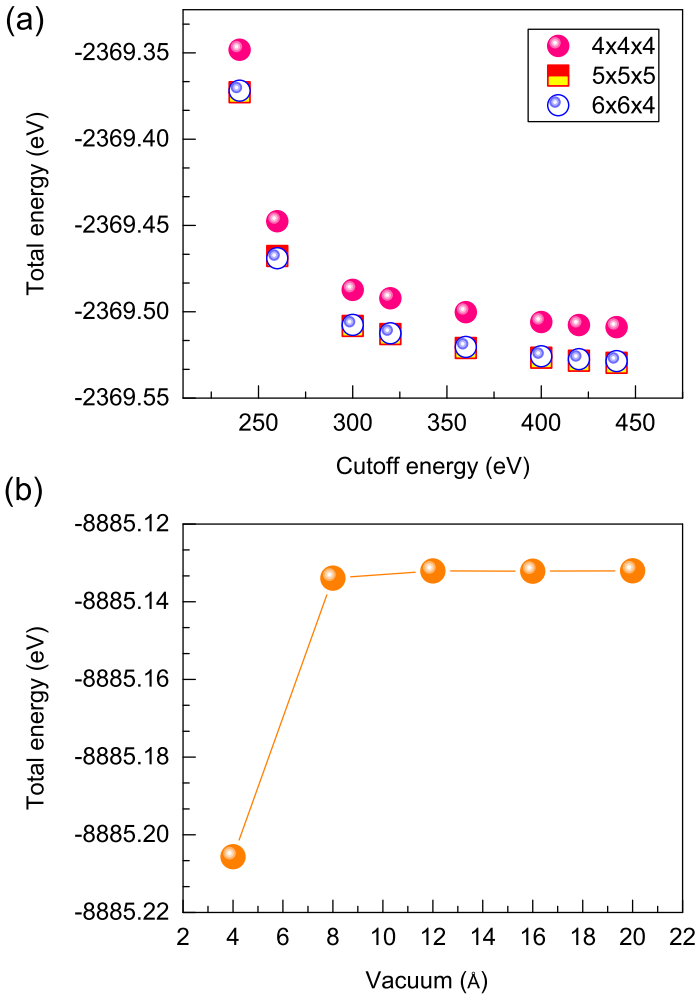

Figure 2.3: (a) A convergence test about n-MnSb with regard to different cutoff energy and $\boldsymbol{k}$-points. (b) A vacuum convergence test of n-MnSb (1×1) Sb-terminated surface.

to obtain more accurate results. During the process of an optimisation test, the two particularly crucial computational parameters, energy cutoff and $\boldsymbol{k}$-point sampling, needed to be examined.

Looking back to Equ. 2.19, when $E_{\mathbf{cutoff}}$ is large enough to satisfy the demands of accuracy, the gradient $dE_{\mathbf{tot}}/dE_{\mathbf{cutoff}}$ will be close to zero. Here, $E_{\mathbf{tot}}$ is the total energy of the supercell. As such, when $\boldsymbol{k}$-points is sufficient by rising the number of plane waves, the quantity of total energy has little change. This process is so-called energetic convergence test. Fig 2.3(a) illustrates an instance of n-MnSb bulk with the total energy as a function of different energy cutoff and $\boldsymbol{k}$-points convergence test. From this image, we can conclude that 400 eV of cutoff energy and

$6 \times 6 \times 4$ of $\boldsymbol{k}$-points are sufficient to be able to attain accurate results, since further increasing the number of $\boldsymbol{k}$-points or cutoff energy will hardly change the optimised total energy. An important point has to be emphasized here is that, owing to the use of pseudopotentials, absolute total energies are less meaningful than relative energies of different structures. It is therefore requisite to maintain the same calculation conditions when making the results of different systems comparable.

As for the surface models, some additional operations about geometry optimisation were taken into account. The following example uses the Sb-terminated (1×1) surface for n-MnSb(0001) shown in Fig. 3.1(c). Firstly, motivated by the desire to avoid the interaction between repeated slabs, a vacuum width selection test was calculated, which are showed in Fig. 2.3. The required vacuum gap is system dependent and should be investigated for the duration of subsequent property calculations. It is readily to observe that the total energy keeps level from 8 Å, so, in the case of clean n-MnSb surface, 8 Å is a suitable vacuum value to obtain the ideal results. However, for the further defect calculations on the surface, selecting a slightly higher vacuum value is always sensible.

Furthermore, the number of atomic layers performs a vital function for getting the right results. Normally, 3 - 7 layers is enough on the basis of different materials. Eight Sb atomic layers and seven Mn atomic layers were placed in the slab for our model seeing from Fig. 2.3(b). Apparently, since supercell is repetitive in 3D space, the supercell in fact defines two surfaces: upper and lower surface. The lateral parameters (lattice parameters and relative atomic position) will be commensurate with the ones in bulk, atoms will not relax too much along x and y axis due to the bulk-like symmetry.

2.1.4 Mulliken population analysis

Mulliken population analysis is developed by Robert S. Mulliken in 1955, and it has provided a common method for estimating partial atomic charges, bond population, charge transfer, etc. This model is based on the population of linear combined atomic orbitals (LCAO) bases [76–79]. Since the use of planewaves (delo-

calised nature) instead of LCAO is the selection of basis set in CASTEP, a projection of the planewave states onto atomic orbitals (localised) is required. This is applied in CASTEP by Segall et al [80,81] according to the approach of Sanchez-Portal [82].

Sanchez-Portal introduced the relationship between methods using planewaves and those using LCAO. The quality of the projection is assessed by the spilling parameter given by [82]

$$S = \frac{1}{N_{\boldsymbol{k}}} \frac{1}{N_\alpha} \sum_{\boldsymbol{k}}^{N_{\boldsymbol{k}}} \sum_{\alpha=1}^{N_\alpha} \left\langle \psi_\alpha \left(\boldsymbol{k}\right) \left| \left(1 - P\left(\boldsymbol{k}\right)\right) \right| \psi_\alpha \left(\boldsymbol{k}\right) \right\rangle , \tag{2.21}$$

where $N_{\boldsymbol{k}}$ and N_α are the number of calculated $\boldsymbol{k}$-points in the Brillouin zone and the number of planewave states, respectively. $\psi_\alpha\left(\boldsymbol{k}\right)$ are the KS Hamiltonian eigenstates. $P\left(\boldsymbol{k}\right)$ is the projection operator of Bloch functions. The essence of the projection apporach is that the spilling parameter (S) surveys the distinction between the eigenstates of the KS Hamiltonian and their projection onto the atomic basis. S varies between 0 (the projected wavefunctions perfectly stand for the planewave states) and 1 (the LCAO basis is orthogonal to the planewave states). The Mulliken analysis that turns the projection of planewaves into the quantification of charges is more detailedly described in Mullikens work [76–79].

2.2 Low energy electron diffraction (LEED)

2.2.1 Experimental Details

Low energy electron diffraction (LEED) was dicovered by Davisson and Germer in 1927 for the determination of surface structures. It was the first experimental evidence to prove electrons are waves and can be diffracted by crystal surfaces. Figure 2.4 shows a schematic drawing of standard LEED setup. Specifically, an electron beam with the energy of 20 - 500 eV is emitted from an electron gun, and then accelerated by an external potential directed to the sample. Subsequently, a number of diffracted beams of electrons are generated. These diffracted beams can be observed on a phosphorous screen, and also be recorded using a video camera, so-called external detector (Fig. 2.4). In addition, there are a series of hemispherical grids included

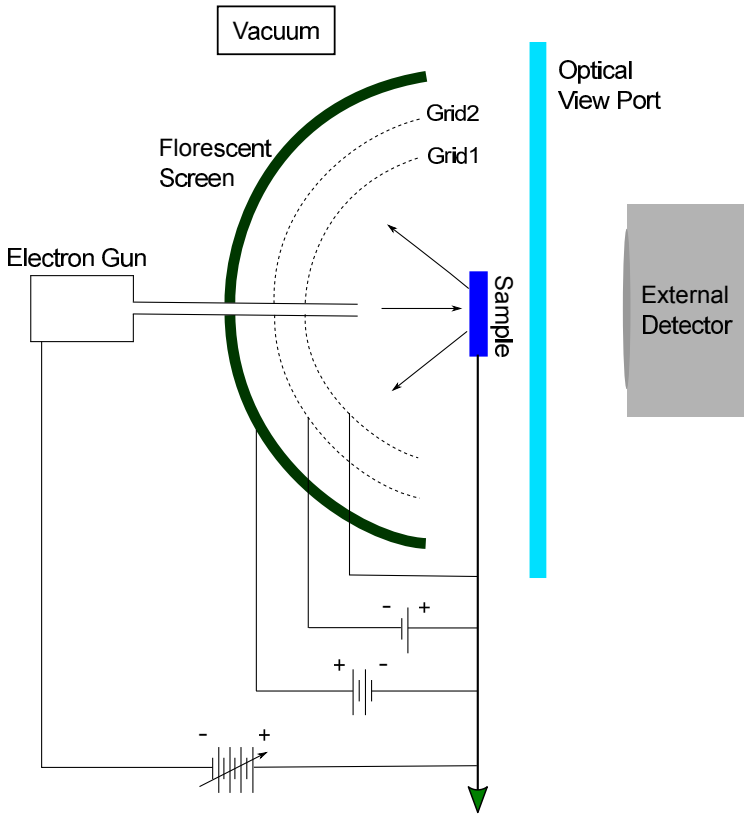

Figure 2.4: Schematic diagram of a LEED system.

in the LEED experiment setup. The first grid closed to the sample is connected to the earth ground to provide a free-field region. The second grid was imposed by a negative potential to enable electorns to be transmitted to the fluorescent screen. All of these parts are enclosed in a vacuum chamber with the pressures of 10^{-10} - 10^{-11} Torr.

The overall image of Fig. 2.4 is called the LEED pattern, and the diffracted beams are reffered to LEED spots shown in Fig. 2.5(a). These diffracted spots are formed when the elastic scattering takes place. That is simply to say energy and momentum must be conserved in the course of the diffraction, namely:

$$E = \frac{\hbar^2 \left|\boldsymbol{k}\right|^2}{2m_e}, \tag{2.22}$$

$$E' = E, \tag{2.23}$$

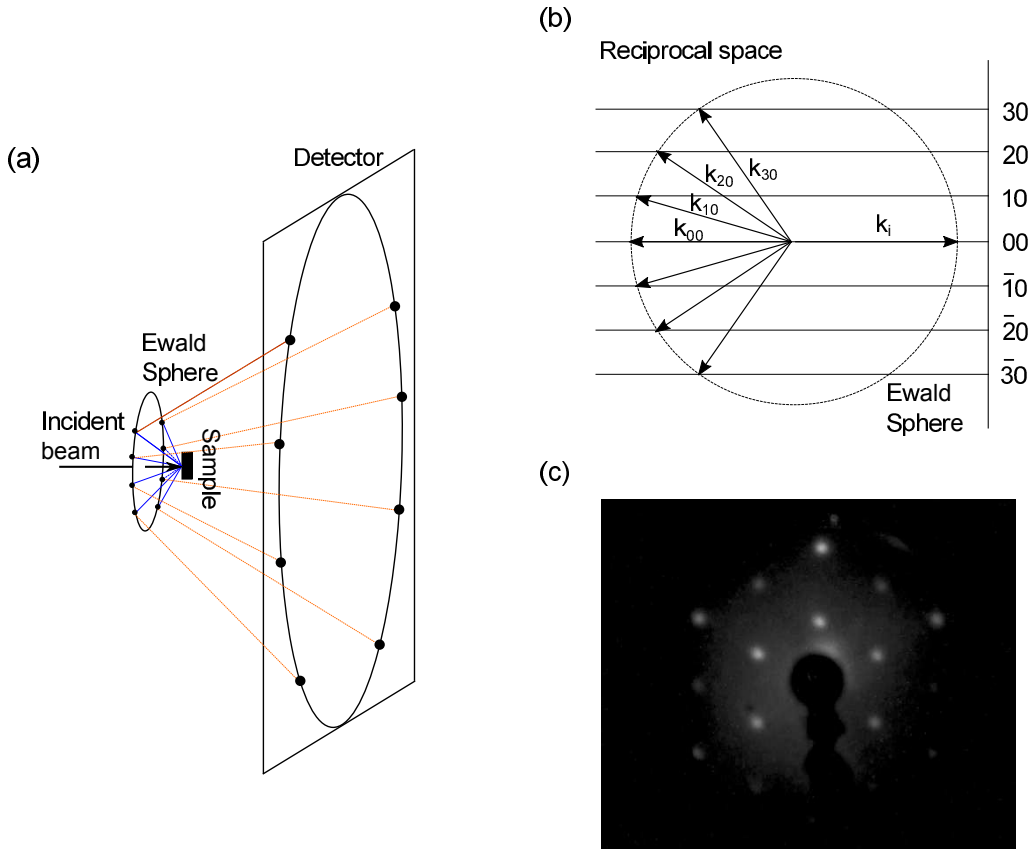

Figure 2.5: Ewald constructions for diffraction from (a) 3D periodic structure and (b) 2D periodic structure. (c) LEED pattern of Sb-capped MnSb(0001) sample [83].

$$|\boldsymbol{k'}|^2 = |\boldsymbol{k}|^2, \tag{2.24}$$

where E and $\boldsymbol{k}$ (E' and $\boldsymbol{k'}$) are the energy and wavevector of the incident (scattered) electrons, respectively. $\hbar$ is the reduced Planck constant. m_e is the mass of the electron. According to the Bragg law and Laue equations, $\boldsymbol{k'}$ can only vary by discrete amounts, *i.e* reciprocal lattice - $\boldsymbol{G}$, defined through

$$\boldsymbol{k'} = \boldsymbol{k} + \boldsymbol{G}. \tag{2.25}$$

Equations (2.24) and (2.25) lead to the Laue diffraction condition:

$$|\boldsymbol{G}|^2 + 2\boldsymbol{k}\boldsymbol{G} = 0. \tag{2.26}$$

These conditions can be grapically described by Ewald sphere construction shown in Fig. 2.5. The points of the reciprocal net are depicted as rods shown in the 3D image of Fig. 2.5(a). For the case of 2D surface, the resulting dffracted beams $\boldsymbol{k'}$ are marked as $\boldsymbol{k}_{00}$, $\boldsymbol{k}_{10}$. based on the indices h, k of the relative reciprocal net vector. An experimental LEED pattern result for MnSb(0001) surface as an example was shown in Fig. 2.5(c) [83].

The quantitative structure investigation of LEED consists of recording diffraction patterns and plotting the spot intensity (I) as a function of gun voltage (V) or electron energy (E) (described as LEED I-V or LEED I-E curves).

2.2.2 Theoretical discussion: LEED I-V calculation

Unlike X-ray diffraction (XRD), the strong electron-solid interaction in LEED gives multiple scattering and structure specificity for surfaces. In reality, it is impossible to invert an observed LEED pattern to get a surface structure. There has to be a forward calculation using trial structures to attain LEED I-V curves.

The scattering factor dependent on multiple scattering, $f(\boldsymbol{s})$, is the vital physical quantity to attain the intensity of a diffracted wave. For the convenience of observing the correspondence between the intensity (amplitude) of a diffracted beam and the scattering factor, the amplitude of single scattering is demonstrated as [84],

$$\boldsymbol{A_s} = \boldsymbol{A}_0 \left[\sum_n \alpha f_n(\boldsymbol{s}) e^{i\boldsymbol{s}\cdot\boldsymbol{r}_n} \right] e^{i\boldsymbol{k'}\cdot\boldsymbol{r}}. \tag{2.27}$$

Here, $f_n(\boldsymbol{s})$ is the scattering factor for the nth atom located at $\boldsymbol{r}_n$. $\boldsymbol{s} = \boldsymbol{k'} - \boldsymbol{k}$ is the momentum transfer, $\boldsymbol{k'}$ and $\boldsymbol{k}$ are the wave vectors of the scattered and incident waves. α is a constant.

In LEED calculations, one approximation is extensively appllied to make the computation more accessible: muffin tin [85]. Specifically, the largest non-overlapping spheres are drawn to represent atomic nucleus. The ion-core potential is spherically symmetry, and the potential between spheres is constant, V_0. V_0 is composed of real part V_{0r} and imaginary part V_{0i}. The introduce of V_{0i} is to correct the energy loss (or gain), such as plasmon excitation (or de-excitation),

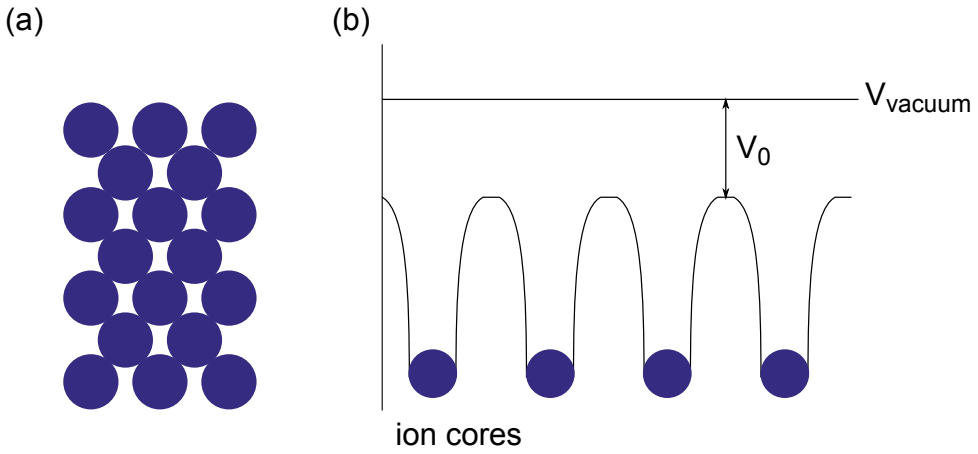

Figure 2.6: (a) Cross-section of a crystal divided by muffin tin models. (b) A schematic of the muffin-tin potential. Note that the potential of vacuum is treated as the external reference, *i.e.* zero-energy level in vacuum. Ion cores are surrounded by spherically symmetrical potential, and the potentials between ion cores are constant (V_0).

caused by inelastically scattered electrons. Figure 2.6(a) shows a cross-section of a crystal represented by muffin-tin models. Figure 2.6(b) gives the cross-section of the potential in a crystal.

On the basis of a spherically symmetric potential, the scattering factor can be described by a phase shift [84],

$$f(\theta) = \frac{1}{2i\boldsymbol{k}} \sum_{l=0} (2l+1) \left[e^{2i\delta_l} - 1 \right] P_l(\cos\theta), \tag{2.28}$$

where $\boldsymbol{k}$ is the magnitude of the wave vection, l is angular momentum, δ_l is called the scattering phase shift, and P_l is the Legendre polynomial. In theory, this equation includes a sum over l from zero to infinity, while it can be truncated at a finit limit, $l_{\max}$. This is also because of the spherical symmetry approximation. Namely, the $l_{\max}$ can be derived when the radius is equal to the one of the non-overlapping sphere. Here, the Equ. 2.28 enabled us to calculate the scattering factor by phase shift combining the muffin tin sphere models without having to solve the Scherödinger equation. Hence, acquaring phase shifts becomes another critical point to attain the scattering factor and to further attain the intensity. The simulation of phase shifts will be shown in the Sec. 2.2.3.

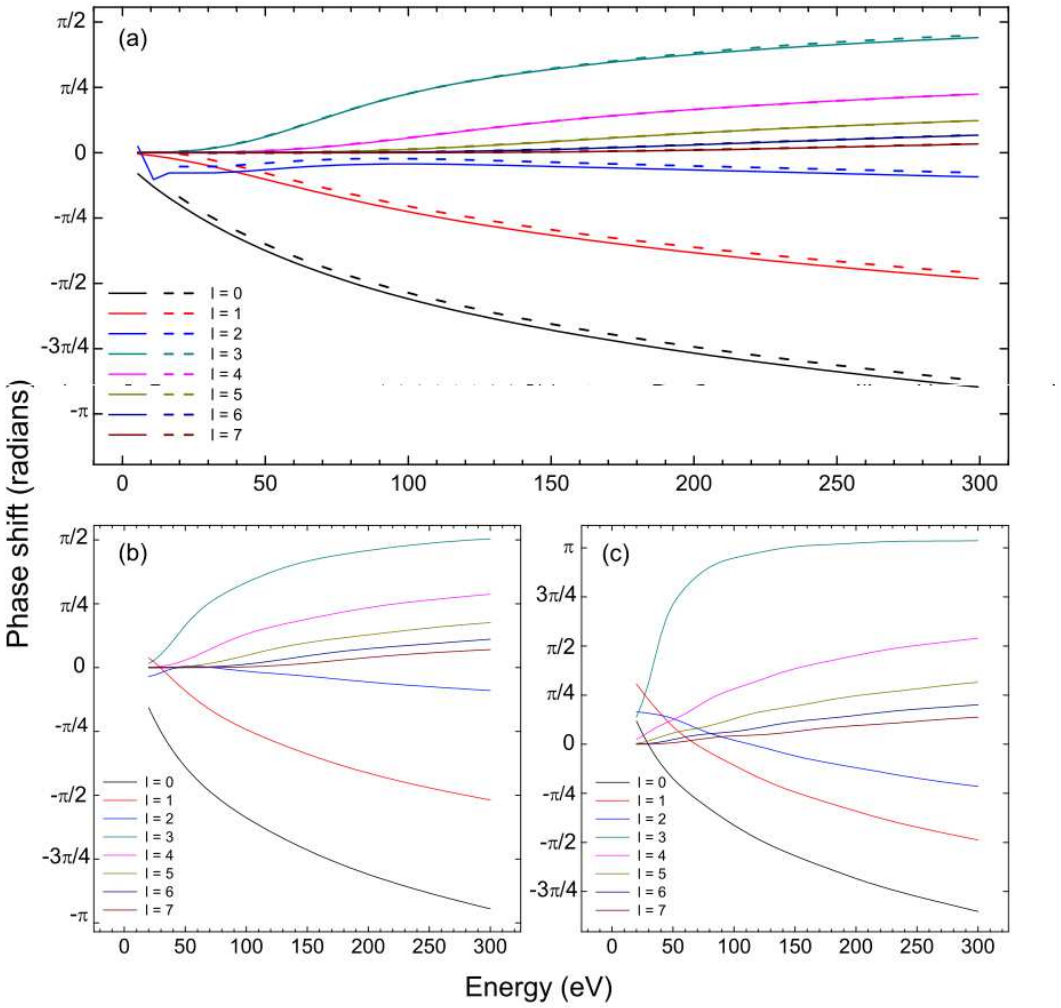

Figure 2.7: (a) Calculated (dashed line) and reference (solid line) phase shifts for nickel. (b) and (c) are calculated phase shifts for Mn and Sb in MnSb [83].

2.2.3 Comparing experiment and theory

The calculated LEED I-V curves are required to be compared with experimental data, and a reliability factor (R-factor) is correspondingly obtained. This R-factor parameter can quantify the agreement between measurement and simulation. The range of R-factor is between 0 and 1, and a lower R-factor value denotes better agreement. It is expressed by

$$L(E) = \frac{I'}{I} = \frac{\partial I/\partial E}{I}. \tag{2.29}$$

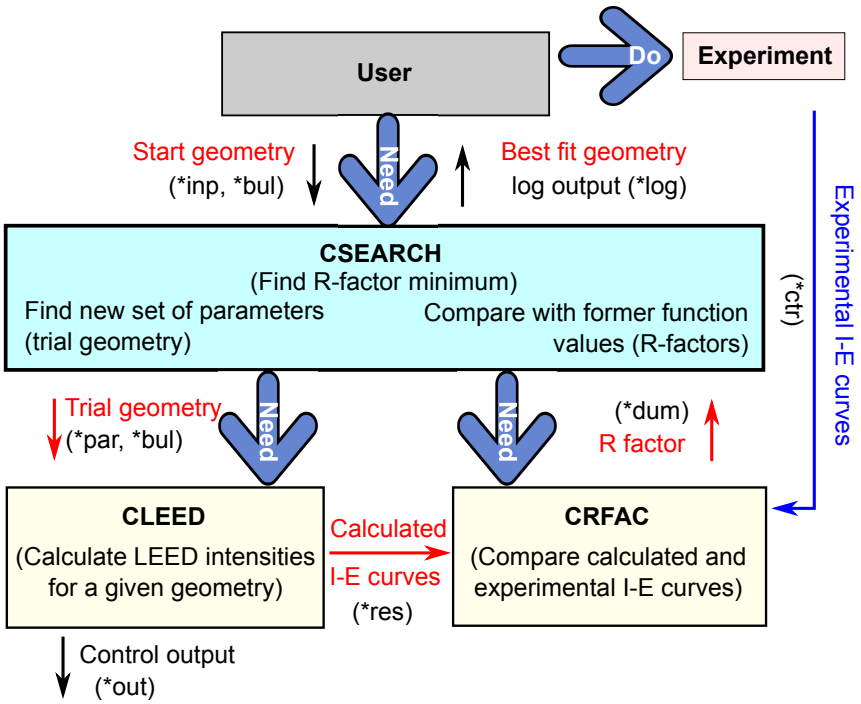

Figure 2.8: The flow chart of the LEED I-V simulation processes.

However, the destructive interference deriving from multiple scattering can readily result in zero intensity. It would cause an infinitely large $L(E)$. Therefore, the Pendry's R-factor defined by the $Y(E)$ function was proposed [86],

$$Y(E) = \frac{L^{-1}}{L^{-2} + V_{0\mathrm{i}}^2} = \frac{L}{1 + (LV_{0\mathrm{i}})^2}, \tag{2.30}$$

where $V_{0\mathrm{i}}$ is the imaginary part of the electron potential. The Pendry R-factor is then given by,

$$R = \frac{\sum_{\boldsymbol{G}} \int \left(Y_{\boldsymbol{G},\mathrm{theory}} - Y_{\boldsymbol{G},\mathrm{experiment}}\right)^2 dE}{\sum_{\boldsymbol{G}} \int (Y^2_{\boldsymbol{G},\mathrm{theory}} + Y^2_{\boldsymbol{G},\mathrm{experiment}}) dE}, \tag{2.31}$$

Empirically, $R = 0.2$ is regarded as a good agreement, $R = 0.35$ is mediocre, and $R = 0.5$ is a bad agreement [86].

2.2.4 Codes used in this work

In order to carry out LEED I-V simulations, there are two main packages were employed:

- Phase shift package developed by van Hove/Barbieri [87].
- Cambridge LEED or CLEED package developed by G. Held [88].

The phase shift package can calculate any structure at an energy range 0 - 300 eV for $l = 0$ to the specified maximum ($l_{\max}$). The phase shifts of MnSb used in this work were calculated by Dr. James Aldous. He attained the consistent results of the phase shift for nickel performed by Van Hove/Barbier package and previous available phase shift [83]. The results of these calculations are shown in Fig. 2.7. Therefore, the calculations can be considered reliable for MnSb.

The CLEED package, which has been successfully applied into the surface structure determination [89–91], includes three separate programs. The first LEED I-V calculation programme, *cleed_nsym*, is responsible for inputing the initial structure and getting back the simulated I-V curves. The second one, *cfrac*, calculates the R-factor between the simulated and experimental data. The third programme, *csearch*, takes this R-factor, and optimise the trial structure until the best R-factor has been achieved. In order to perform a structure opimisation, three input files are required: *.inp* file - taking the overlayer structure information; *.bul* file - taking the bulk structure information; *.ctr* file - a control file to define the relationship between theoretical and experimental LEED I-V curves. The calculation processes described above are outline in Fig. 2.8.

Chapter 3

Phase equilibrium of transition metal pnictides surfaces-(1 × 1)

First-row transition metal compounds exhibit rich variety of intrinsic magnetic ordering. However, the detailed electronic and magnetic properties of two-dimensional TMP are still unexploited. Here, surface layered structure simulations of several representative TMP materials with different magnetic characteristics (CrAs and CrSb - antiferromagnetism; MnAs and MnSb - ferromagnetism; NiAs and NiSb - paramagnetism) are investigated. This will provide fundamental understanding of TMP, and in particular, will contribute to the development of interface and thin film growth.

This chapter starts with a discussion of the crystallography of different terminated n-MnSb(0001) surfaces, proceeds with the summary of the relationship between the surface stability and their magnetic property of given TMP materials. The remainder of this chapter will introduce a more complicated $(1\bar{1}00)$ surface of n-MnSb for comparison with the (0001) surface stability. The comprehensive models will be designed and the Gibbs free energy as well as the magnetic moment will be calculated.

3.1 Phase equilibrium of MnSb(0001) surface

3.1.1 Computational details and models

The exchange correlation functional of generalised gradient approximation (GGA) type [92] and the pseudopotentials of CASTEP-generated on-the-fly were applied. Spin polarisation as an additional degree of freedom has been utilised in all of our designed models below so as to describe their magnetic characters. The energy cut-off value was set at 400 eV after a careful convergence testing for bulk

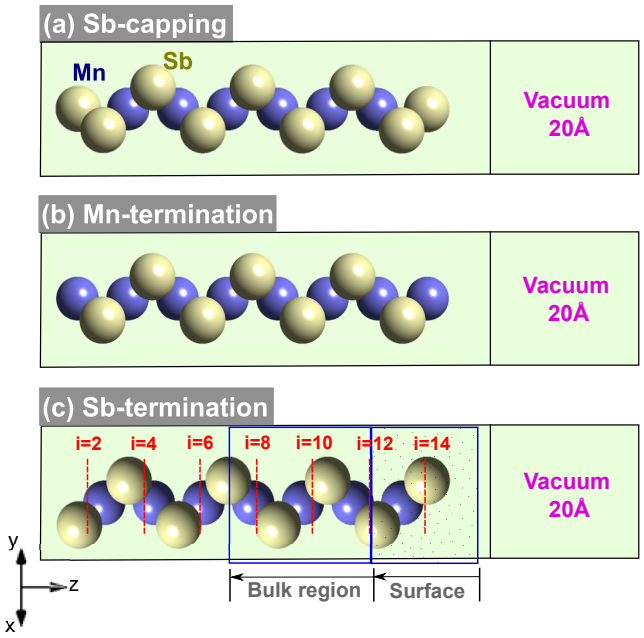

Figure 3.1: Sketch of slab models of (1 × 1) *n*-MnSb(0001) surface (the yellow cycles stand for Sb atoms, and the purple cycles represent Mn atoms): (a) Sb capping on Sb-terminated; (b) Mn-terminated; (c) Sb-terminated surfaces.

phase of *n*-MnSb (see Sec. 2.3.1) and all of calculated materials below including MnAs, CrAs, CrSb, NiAs and NiSb. Fifteen atomic layers with 20 Å vacuum of MnSb(0001) surface as a periodic slab are taken into account in order to ensure high accuracy. Based on the surface relaxation calculations (details in section 3.2), the top three layers of both sides are regarded as surfaces, and the rest of nine layers without significant atomic movement are considered as materials bulk. The ***k***-point sampling for the Monkhorst-Pack scheme (5×5×1) was used, and all of atomic positions were allowed to fully relax until each force component on the atoms reduced below 0.03 eV/Å.

The unreconstructed (1 × 1) *n*-MnSb(0001) surface has alternating layers of cations and anions, leading to the polar structure in the perfect bulk-truncated surface. Therefore, two basal surfaces terminated by Mn and Sb with the hexagonal layers along *c*-axis have been created shown in Fig. 3.1(b) and (c). Meanwhile, experiments also investigate a new *n*-MnSb surface passivated by antimony capping layer, finding that the capping Sb procedure is not only able to prevent surface oxidation after being exposed to the air, but also able to maintain the ferromagnetic

properties [83]. Considering this film structure, an antimony-coated model has been taken into account as well [see Fig. 3.1(a)]. The purpose of this section is to calculate the relative Gibbs free energy of different terminated n-MnSb surfaces and then compare their stability.

3.1.2 Chemical potential and Gibbs free energy

The n-MnSb(0001) surface is polar, which contains a different number of Mn and Sb atoms in each unit cell. Therefore, the chemical potential as a function of Gibbs free energy must be introduced into the calculation to compare the stability of these three considered (1 × 1) surfaces.

The general expression for Gibbs free energy (G) of ground states is given by

$$G = E_{\text{total}} - \text{TS} - \text{PV} - \sum_i \mu_i N_i. \tag{3.1}$$

The two quantities of μ_i and N_i are chemical potential and the number of atoms for species i in the slab, respectively. E_{total} is the total energy of three slabs at zero temperature and pressure, where entropy (S) is a quantity being capable of measuring the randomness of one system, which is therefore equal to zero for a stably ordered crystal at absolute zero temperature. In the meantime, such low pressure is commonly difficult to change the volume of solids. Hence, in general, these two terms on the right side, TS and PV, tend to be neglected. G then can be simplified, as shown below, with only two degrees of freedom corresponding to μ_{Mn} and μ_{Sb}:

$$G = E_{\text{total}} - \mu_{\text{Mn}} N_{\text{Mn}} - \mu_{\text{Sb}} N_{\text{Sb}}. \tag{3.2}$$

In order to avoid the condensate of elemental Sb and Mn crystallising at the surface, a upper bound for each chemical potential must be given by the respective bulk phase ($\mu_{\text{Sb}}^{\text{bulk}}$, $\mu_{\text{Mn}}^{\text{bulk}}$) [93, 94],

$$\mu_{\text{Sb}} \leq \mu_{\text{Sb}}^{\text{bulk}} \tag{3.3}$$

and

$$\mu_{\mathrm{Mn}} \leq \mu_{\mathrm{Mn}}^{\mathrm{bulk}}. \tag{3.4}$$

By defining another thermodynamic relation:

$$\mu_{\mathrm{Mn}} + \mu_{\mathrm{Sb}} = \mu_{\mathrm{MnSb}}^{\mathrm{bulk}} = \mu_{\mathrm{Mn}}^{\mathrm{bulk}} + \mu_{\mathrm{Sb}}^{\mathrm{bulk}} - \Delta H_f, \tag{3.5}$$

the constraints of Sb chemical potential can be written as:

$$-\Delta H_f \leq \mu_{\mathrm{Sb}} - \mu_{\mathrm{Sb}}^{\mathrm{bulk}} \leq 0 \tag{3.6}$$

or

$$\mu_{\mathrm{Sb}}^{\mathrm{bulk}} - \Delta H_f \leq \mu_{\mathrm{Sb}} \leq \mu_{\mathrm{Sb}}^{\mathrm{bulk}}. \tag{3.7}$$

The chemical potential of n-MnSb, Mn, and Sb in their bulk phase are presented in Table 3.2. The heat of formation (ΔH_f) of 0.31 eV can be estimated by Equ 3.5 and the data from Table 3.2, which is in agreement with the magnitude of other calculation about 0.36 eV [95]. These derived chemical potentials and heat of formation values, together with the limitation requirements of Eqs. 3.6 and 3.7, allow us to acquire accurate restrictions on the range of Sb chemical potential:

$$0.31 \leq \mu_{\mathrm{Sb}} - \mu_{\mathrm{Sb}}^{bulk} \leq 0 \tag{3.8}$$

and

$$-593.03 \leq \mu_{\mathrm{Sb}} \leq -592.72. \tag{3.9}$$

Furthermore, after this mathematical treatment of Eqs. 3.2 and 3.5, one unknown quantity (μ_{Mn}) will be eliminated and the Gibbs free energy will be given by,

$$\begin{aligned} G &= E_{\mathrm{total}} - N_{\mathrm{Mn}} \left(\mu_{\mathrm{MnSb}}^{\mathrm{bulk}} - \mu_{\mathrm{Sb}}\right) - \mu_{\mathrm{Sb}} N_{\mathrm{Sb}} \\ &= E_{\mathrm{total}} - N_{\mathrm{Mn}} \mu_{\mathrm{MnSb}}^{\mathrm{bulk}} + (N_{\mathrm{Mn}} - N_{\mathrm{Sb}}) \mu_{\mathrm{Sb}}. \end{aligned} \tag{3.10}$$

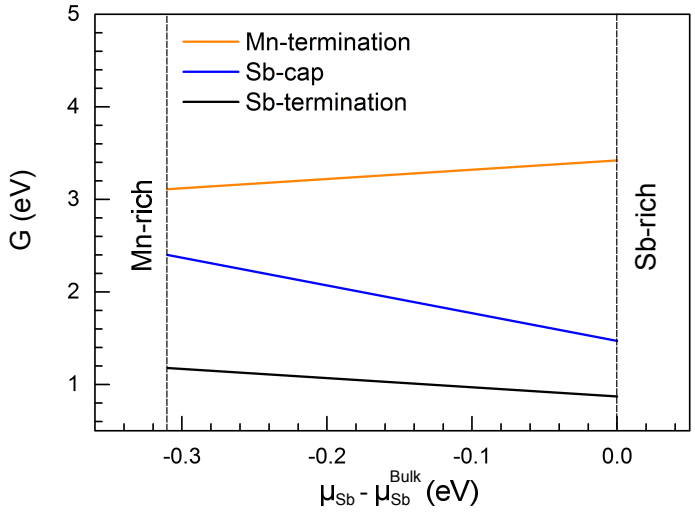

Figure 3.2: The Gibbs free energy (G) of (1 × 1) surfaces versus $\mu_{\mathrm{Sb}} - \mu_{\mathrm{Sb}}^{\mathrm{bulk}}$, the dashed lines illustrate the position of heat of formation. When μ_{Sb} is equal to $\mu_{\mathrm{Sb}}^{\mathrm{bulk}}$, the surrounding is defined as Sb-rich. From the opposite direction, it is the Mn-rich environment.

Equation 3.10 provides valuable evidence that a linear logical correlation between Gibbs free energy (G) and the chemical potential of Sb (μ_{Sb}) exists. The relative values of E_{total}, N_{Mn}, N_{Sb}, and $\mu_{\mathrm{MnSb}}^{\mathrm{bulk}}$ are described in Table 3.1 and 3.2, respectively. For the sake of clarity, we take the Sb-terminated surface slab as an example. In this case, Equ. 3.10 can be expressed using the given values,

$$\begin{aligned} G &= -8885.13 - 7 \times (-1184.76) + (7-8)\mu_{\mathrm{Sb}} \\ &= -\mu_{\mathrm{Sb}} - 591.81. \end{aligned} \tag{3.11}$$

Following the subsidiary conditions in Eqs. 3.9 and 3.11, the range of G can be retained:

$$0.92 \leq G \leq 1.23. \tag{3.12}$$

Performing the same calculation on the Mn-terminated ($3.11 \leq G \leq 3.42$) and Sb-covered ($1.47 \leq G \leq 2.40$) surfaces, we plot the free energy, G, against $\mu_{\mathrm{Sb}} - \mu_{\mathrm{Sb}}^{\mathrm{bulk}}$ shown in Fig. 3.2. The obvious conclusion is that the Sb-terminated surface

Table 3.1: The total energy and the number of different atoms for these three (1 × 1) surfaces.

	N_{Mn}	N_{Sb}	Total energy (eV)	G (eV)	
				Mn-rich	Sb-rich
Mn-termination	8	7	-8881.89	3.11	3.42
Sb-capping	6	9	-8885.21	2.40	1.47
Sb-termination	7	8	-8885.13	1.18	0.87

is exclusively favourable over the whole range of the chemical potential permitted, which is consistent with the work of Jenkins [96]. Based on the calculation results, we also conclude that Sb-covered layers although are able to avoid the oxidisation, yet it will sacrifice the stability of system.

In order to verify the accuracy of the calculation of the non-stoichiometric slabs in this thesis, fourteen layers of stoichiometric slabs of the MnSb(0001) surface is also calculated. The corresponding free energy can be expressed as $G = E_{\mathrm{total}}^{\mathrm{stoichimometric}} - nE_{\mathrm{total}}^{\mathrm{bulk}}$, where $E_{\mathrm{total}}^{\mathrm{stoichimometric}}$ is the total energy of the stoichimometric slab; $E_{\mathrm{total}}^{\mathrm{bulk}}$ is the bulk energy per Mn-Sb; n is the number of Mn-Sb atoms in the slab. The average free energy is $G = -8291.140 - 7 \times (-1184.784) = 2.094\mathrm{eV}$. In the case of the non-stoichimomentric slab, the average values of the free energy of the Sb-terminated and Mn-terminated surfaces are 1.075 eV ($0.92 \leq G \leq 1.23$) and 3.265 eV ($3.11 \leq G \leq 3.42$), respectively. Therefore, the average free energy is 2.170 eV, which is in a good agreement with that of the stoichimomentric slab (2.094 eV).

3.2 The comparison of stability and magnetic properties for transition metal pnictides (0001) surface

For the motivation of achieving the correlation between surface energy and magnetic moment of different TMPs (here, TMP can be defined by a general formula

MX, M = transition metals, and X = As or Sb), layered surface structures with representative ferromagnetic (MnAs and MnSb), antiferromagnetic (CrAs and CrSb) and non-magnetic materials (NiAs and NiSb) have been investigated. The structure information of all of required phases, as well as their chemical potential and heat of formation (ΔH_f) are listed in Table 3.2. It is well-known that TMPs basically crystallise at NiAs-type (B81) strucuture, albeit different growth temperature can induce orthorhombic MnP-type (B31) crystals. Here, we focus just on NiAs-type structures and summarise the generality of rules of the correspondence between the structural stability and magnetic properties. In this section, 19 atomic monolayers with a vacuum gap of 20 Å were selected to make sure that there are enough layers behaving a bulk-like interior.

The Gibbs free energy calculation is generated by following the same way with Sec. 3.2.2. Thereinto, the heat of formation in Equ. 3.5 is generalised to $\mu_{\mathrm{M}}+\mu_{\mathrm{X}} = \mu^{\mathrm{bulk}}_{\mathrm{Binary}} = \mu^{\mathrm{bulk}}_{\mathrm{M}} + \mu^{\mathrm{bulk}}_{\mathrm{X}} - \Delta H_f$, and free energy in Equ. 3.10 becomes

$$\begin{aligned} G &= E_{\mathrm{total}} - N_{\mathrm{M}}\left(\mu^{\mathrm{bulk}}_{\mathrm{Binary}} - \mu_{\mathrm{X}}\right) - \mu_{\mathrm{X}} N_{\mathrm{X}} \\ &= E_{\mathrm{total}} - N_{\mathrm{M}}\mu^{\mathrm{bulk}}_{\mathrm{Binary}} + (N_{\mathrm{M}} - N_{\mathrm{X}})\mu_{\mathrm{X}}. \end{aligned} \tag{3.13}$$

In order to compare their stability, surface energy (σ), has to be introduced in this scheme to address the thermodynamic stability, which is the Gibbs free energy per surface area, $\sigma = \dfrac{G}{2A}$. The factor $\dfrac{1}{2}$ is because of two equivalent surfaces presence in the slab. Using the data listed in Table 3.2 and 3.3, the surface energies of different MX are plotted as function of $\mu_X - \mu^{\mathrm{bulk}}_{\mathrm{X}}$ in Fig. 3.3. It is observed that in the thermodynamically allowed region of the chemical potential all surfaces prefer the X (As or Sb)-terminated configurations in each binary compound even though all of them have completely different magnetic properties. That is to say magnetic properties are not the direct determinant of the surface stability preference. Nevertheless, the magnetic materials (CrAs-CrSb and MnAs-MnSb) seem to have similar stability mechanism. Note that Sb-terminations are always more energetically favourable surfaces than As-terminations in both Cr- and Mn-based binaries. And also the Cr-terminated surface in CrSb is lower in energy than Cr-terminated

Table 3.2: Structure parameters of various acquired bulk materials, and the chemical potentials & heat of formation (ΔH_f).

Compounds	Space group	Lattice parameters (Å)			Chemical potential	ΔH_f
		a	b	c	$\mu_{\mathrm{MX}}^{\mathrm{bulk}}$ (eV)	(eV)
CrAs	P63/MMC	3.630	3.630	5.810	-3273.208	0.648
CrSb	P63/MMC	4.123	4.123	5.470	-3039.744	0.247
α-MnAs	P63/MMC	3.725	3.725	5.703	-1418.157	0.644
n-MnSb	P63/MMC	4.120	4.120	5.510	-1184.756	0.306
NiAs	P63/MMC	3.617	3.617	5.038	-2021.359	0.571
NiSb	P63/MMC	3.928	3.928	5.120	-1788.307	0.582
As	R-3M	3.760	3.760	10.441	-825.783	—
Sb	R-3M	4.307	4.307	11.273	-592.720	—
α-Mn	I-43M	8.910	8.910	8.910	-591.730	—
Ni	P63/MMC	2.481	2.481	4.064	-1195.005	—
Cr	Im3m	2.468	2.468	2.468	-2446.777	—

surface in CrAs. Mn-terminations behave similarly in MnSb and MnAs. Therefore, Sb can create more stable surface by combining with transition metal than As can. However, in the case of Ni-based non-magnetic system, Ni-terminated surface has lower energy in NiAs than the one in NiSb. Some enegy trends will be analysed by surface relaxation later.

All surfaces calculated in an energetic minimisation process undergo an atomic arrangement. In order to detect how the surface energy is effected by surface structure, the displacements of coordinated atomic positions on the surface are provided, which is quantitatively defined by $\Delta d_i = d_{i,i+1} - d_{\text{bulk}}$. Here, Δd_i is the change of the interlayer spacing between i^{bulk} and $(i{+}1)^{\text{bulk}}$ layers relative to the unrelaxed interlayer spacing, and $d_{i,i+1}$ is the difference between i^{th} and $(i{+}1)^{\text{th}}$ of relaxed interlayer spacing. Negative values represent a contraction, while positive values indicate an expansion. Since MnSb is the dominate material this thesis mostly concentrates on, the surface relaxation as well as corresponding surface energy of MnSb and other Sb-based compounds are compared and illustrated in Fig. 3.4. From the energy perspective, it appears likely that the energetic order follows the converse tendency for M- and Sb-terminated materials. Specifically, the lowest energy surface is found to be terminated by Sb atom in NiSb, and the second-most stable state is formed by Sb-terminated surface in MnSb. Sb terminated in CrSb is the worst case. Another cleaved Mn-terminated surface system has slightly higher surface energy, but stabilised at Cr-termination in CrSb and following at Mn-termination in MnSb. These observations can be effectively explained by the surface relaxations presented in Fig. 3.4(b). In the M-terminated system, Cr-terminated surface possesses the smallest oscillations with 0.11 Å contractions at the outmost atomic layer and 0.116 Å expansions of subsurface layer, while Mn-terminated surface has a much larger movements which has been reflected in first four layers. The highest relaxation is observed on Ni-terminated surface in connection with 0.333 Å. Evidently, the surface stability correlated with the surface relaxation. The origin of the relaxation can be explained by the electrostatic model proposed by Fennis and Heine in 1974 [97]. It states that the electrons at the surface will be pushed out to the vacuum in order

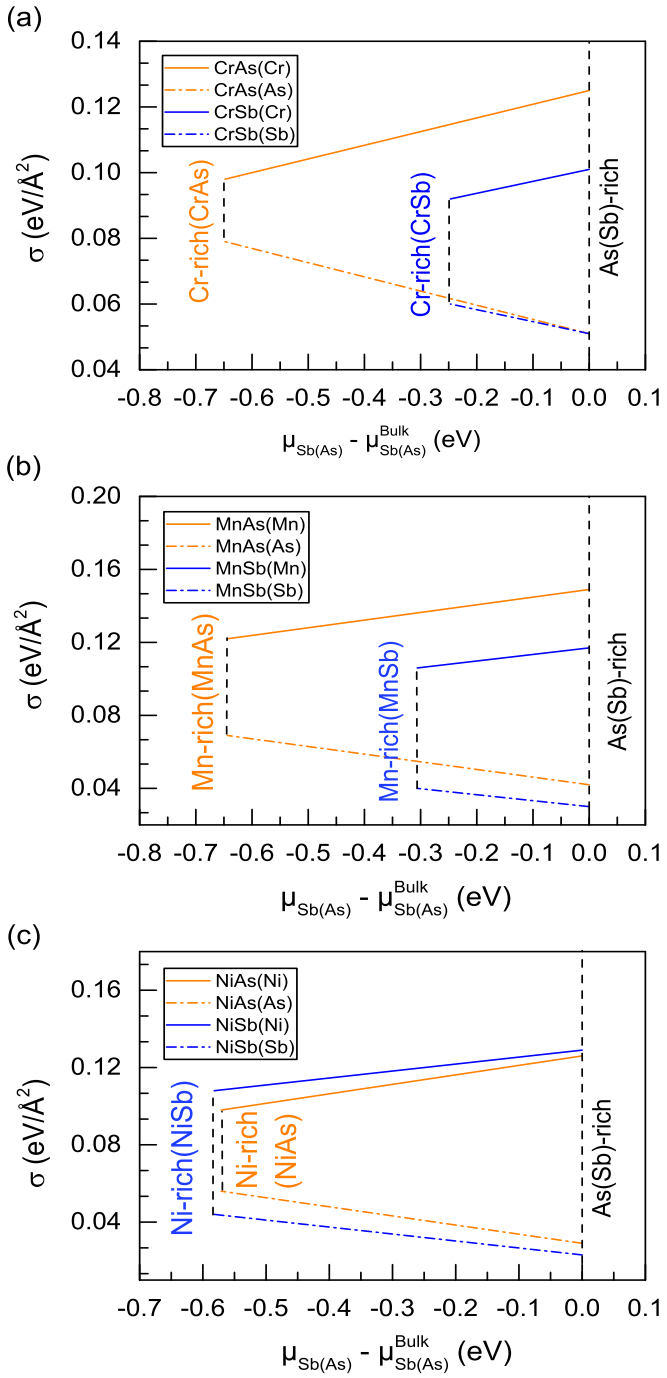

Figure 3.3: Surface energy of different MX (001) surfaces (a) CrX, (b) MnX, and (c) NiX (X = As and Sb) plotted versus $\mu_X - \mu_X^{\text{bulk}}$. The surface energy of M- and X-terminated surfaces is represented by the solid and dot-dashed lines respectively. The orange and blue lines indicate As- and Sb- compounds.

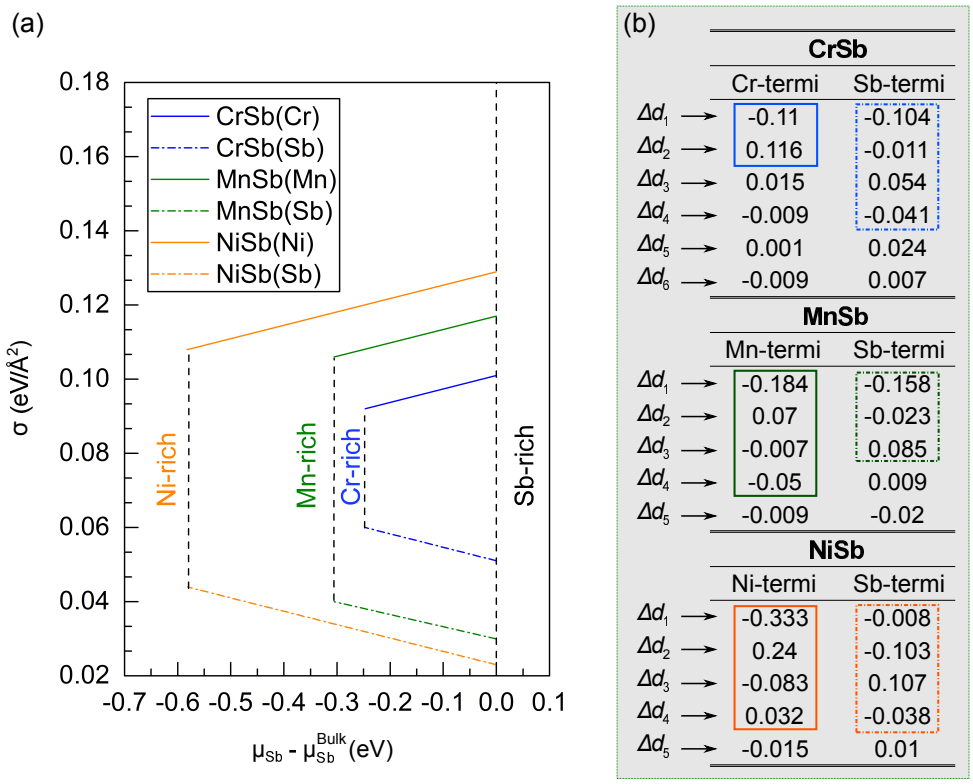

Figure 3.4: (a) Surface energy of different MSb(0001) surfaces (M = Cr, Mn, Ni) plotted versus $\mu_X - \mu_X^{bulk}$. The surface energy of M- and X-terminated surfaces is represented by the solid and dashed lines respectively. The blue, green and orange lines indicate Cr-, Mn-, and Ni-compounds. (b) The surface relaxation of the first few atomic layers for different terminated surfaces presented in Fig. 3.4(a). The data framed in the box refers to the relaxed surface layers. The maximum number of the relaxed layers is four, which will save another 10 layers to behave as a bulk region due to the big enough slabs (19 layers).

to acquire a uniform electron density. Here, the atom configurations of Cr, Mn, and Ni are $3d^5 4s^1$, $3d^5 4s^2$, and $3d^8 4s^2$, respectively. Ni has the maximum number of electrons, which should spread more electrons out to smooth the surface electron density compared with Mn and Cr. Hence, Ni-terminated surface obtains the largest surface relaxation. As the consequence of the minimum number of electrons for Cr, Cr-terminated surface experiences the smallest relaxation. The Sb-terminations in different compounds conform to the same rules exactly. The lowest Sb-terminated surface energy of NiSb has the smallest surface relaxation only about -0.111 Å for the first two layers.

For the purpose of exploring the nature of the most-stable Sb-terminated surface of MnSb, spin-polarised layer-projected density of states (LDOS) has been

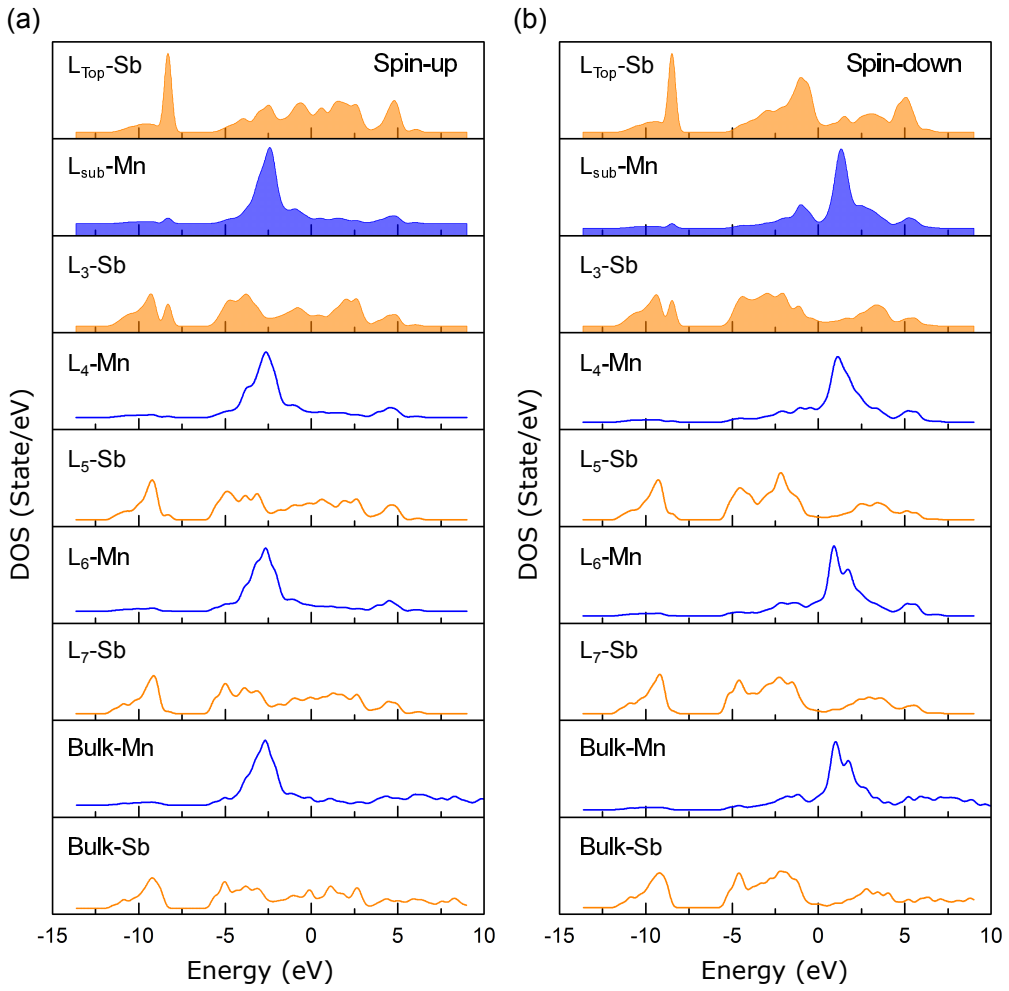

Figure 3.5: Layer-resolved LDOS of Sb-terminated surface and bulk of MnSb. The spin-up and spin-down of the LDOS is represented by the (a) Left and (b) right panels. The orange and blue colour plots indicate the LDOS of Sb and Mn atomic layers. For comparison, the surface region within the slab is presented by the shadow part, while the bulk area is presented by the solid lines.

calculated and shown in Fig. 3.5. It shows that charge distribution has been almost limited in first three layers for both spin-up and spin-down due to the significantly different DOS curves comparing with bulk layers. This agrees with the surface relaxation demonstrated in Fig. 3.4(b). The surface relaxation is mainly delocalised over the first three layers in the vicinity of the surface. In addition, both of spin-up and spin-down DOS indicate the splitting exchange at the surface. Therefore, the broken symmetry is not related to the magnetisation direction.

The magnetic moment of bulk and (0001) surfaces are listed in Table 3.3 as well. It shows that, even if surfaces have been created, the magnetic proper-

Table 3.3: Stoichiometries and calculated total energy for representative candidates, as well as magnetic moments at the bulk phases and their corresponding surfaces.

		N_{M}	N_{X}	Total energy (eV)		Magnetic moment (μ_B)	
						Bulk	Surface
CrAs	Cr-termination	10	9	-31903.415	Antiferromagnetic [12]	2.870	3.109
	As-termination	9	10	-30283.410			2.581
CrSb	Cr-termination	10	9	-29801.851		3.015	3.291
	Sb-termination	9	10	-27948.972			2.908
MnAs	Mn-termination	10	9	-13352.284	Ferromagnetic [12]	3.284	3.356
	As-termination	9	10	-13588.142			3.144
MnSb	Mn-termination	10	9	-11251.374		3.454	3.607
	Sb-termination	9	10	-11254.632			3.342
NiAs	Ni-termination	10	9	-19385.006	Paramagnetic [12]	0	0
	As-termination	9	10	-19017.323			0
NiSb	Ni-termination	10	9	-17286.798		0	0
	Sb-termination	9	10	-16686.853			0

ties of all of the MX compounds are still preserved from their bulk phase. The earlier experimental results suggest that there is strong connection between crystal structures (lattice parameters) and magnetic properties for CrX compounds. The magnetic moment (*e.g.* 2.870 and 3.015 for CrAs and CrSb), generally, increases with the increasing of their lattice parameter b (3.610 and 4.123 Å for CrAs and CrSb) [11]. This criterion of bulk magnetic moment is satisfied by the majority of MnX compounds.

NiSb surfaces remain paramagnetic feature like the NiSb bulk. For the other surfaces, all of the energetically less stable M- terminated surfaces are characterised by an enhancement of the magnetic moment compared with it in the bulk (*e.g.* for the case of CrAs, the Cr magnetic moment increases from 2.870 per Cr atom in bulk to 3.105 per Cr atom in Cr-terminated surface.) This increase of magnetic moment of M-terminated surfaces is partly attributed to the lower coordination of *3d*-orbital dominated transition metal surfaces (valence electron configuration of Cr: $3d^5 4s^1$ and Mn: $3d^5 4s^2$). Generally, the reduced coordination related with atoms at the surface gives rise to the reduced overlap of d electron wave function and to a resulting narrow d band. At the surface of $3d$ transition metals, the $3d$ bands narrow and are more localised. Hence, the density of states at Fermi level increase in the vicinity of the crystal surface and lead to an enhancement of magnetic moment. That is to say both the reduced overlap and relatively narrow bands result in the magnetic moment enhancement [98, 99]. For the preferred X-terminated surfaces (valence electron configuration of As: $4s^2 4p^3$ and Sb: $5s^2 5p^3$), the reduced dimensionality has no narrow bands becasue of *sp* orbital hybridisation. This induces a decreased magnetic moment of X-terminated surfaces compared with the one in the bulk.

3.3 Stability comparison of MnSb(0001) and (1$\bar{1}$00) surface

It is well-known that the MnSb(0001) surface can be grown on GaAs(111)B substrate, namely As-terminated surface, in an atomically flat interface [101]. However, some hexagonal nano-islands were observed in the initial growth process with the nominal thickness between 3 and 5 ML, showing the result of $w >> h$ in experi-

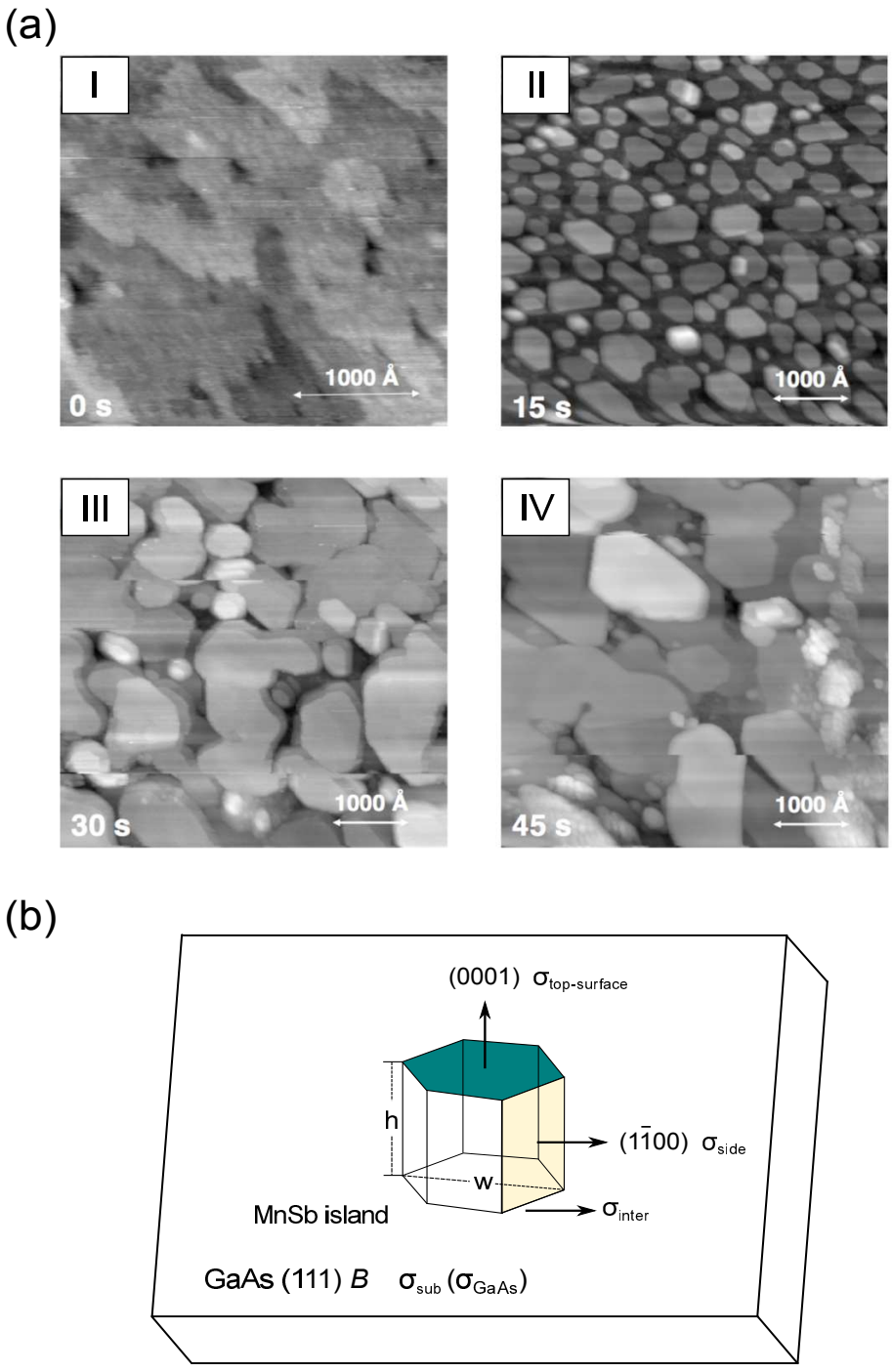

Figure 3.6: (a) STM images for MnSb/GaAs(111)B thin film. The growth time is (I) 0 s, (II) 15 s, (III) 30 s, and (IV) 45 s [100]. (b) Schematic diagram of three dimensional MnSb(0001) island formed on GaAs(111)B surface.

Table 3.4: Measurements from Fig. 3.6(a) [100]. $t_{\mathrm{Mn+Sb}}$ is the co-deposition time. The total growth time is defined as $t = t_{\mathrm{Mn+Sb}} + t_{\mathrm{Mn}}$. $c\%$ is the percentage of the island. h_{max} and h_{av} are the maximum and average island heights, respectively.

Panel	$t_{\mathrm{Mn+Sb}}$ (s)	t_{Mn} (s)	$c\%$	h_{max} (Å)	h_{av} (Å)
(I)	0	0	0	3 ± 1	3 ± 1
(II)	10 ± 1	5 ± 1	70 ± 5	48 ± 5	20 ± 5
(III)	20 ± 2	10 ± 1	92 ± 2	86 ± 5	45 ± 10
(IV)	30 ± 3	15 ± 1	97 ± 2	114 ± 5	60 ± 10

ment [101,102]. The scanning tunnelling microscope (STM) with $t = 15$, 30 and 45 s growth was carried out by Dr. Stuart Hatfield presented in Fig. 3.6(a). The surface in Fig. 3.6(a)-(II) exhibits flat-topped islands with around 500 nm in diameter, and an average of 20 Å in height covering approximately 70 % of the surface. These islands reveal clear preferential edge directions at 60° rotations, suggesting hexagonal symmetry. With the more material growth, the 3D islands increases to about 95 % after 30 s growth [Fig. 3.6(a)-(III)] and 97 % after 45 s [Fig. 3.6(a)-(IV)]. Once the islands have coalesced, the growth mode will change to layer-by-layer growth.

In this section, we attempt to use DFT to explain the reason for the island formation. The film consisting of MnSb nanocluster (island) fabricated on GaAs is illustrated in Fig. 3.6(b). w and h are the width and height of the island, respectively. $\sigma_{\mathrm{top-surface}}$, σ_{side}, $\sigma_{\mathrm{sub}}(\sigma_{\mathrm{GaAs}})$ and σ_{inter} denote the surface energy of top (0001), side $(1\bar{1}00)$ of MnSb, As-terminated $(111)B$ GaAs surface and the interface energy between n-MnSb/GaAs. Compared with Sb-Ga, Mn-Ga, and Mn-Ga types, Mn-As has been confirmed as the most stable interface configuration. This was calculated by another PhD student Collins Ouserigha under Dr. Gavin Bell's group. Hence, the interface energy of n-MnSb/GaAs is only calculated for Mn-As system here.

These phenomena of the initial 3D island formation (including their growth

shape) and continuous 2D layer-by-layer growth are expected to be driven by several factors in theory:

(1) $\sigma_{\mathrm{Sub}} < \sigma_{\mathrm{top-surf}} + \sigma_{\mathrm{inter}}$. The growing layers tend to be more favourable for minimising the interface energy first to trigger islands formation, which is shown in Sec. 1.9 [103].

(2) $\sigma_{\mathrm{top-surface}} << \sigma_{\mathrm{sub}}$. The As-terminated GaAs surface should be a highly active surface as well (*i.e.* high surface energy) in order to make MnSb covering almost the whole substrate surface [97 % coverage after 45s growth shown in Fig. 3.6(a)-(IV)].

(3) $\sigma_{\mathrm{top-surface}} < \sigma_{\mathrm{side}}$. In an island, the more (less) stable surface with the lower (higher) surface energy should grow a broader (narrower) surface. It means that the perfect (0001) surface should have lower surface energy than that of the $(1\bar{1}00)$ surface to realise the experimental observation of $w >> h$. In other words, the height (h) of these formed islands related to the higher surface energy of the $(1\bar{1}00)$ facet should be shorter than the width (w) corresponding to the lower surface energy of the (0001) facet in order to create the much broader (0001) surface.

As a consequence, the calculations of surface energy for (0001) and $(1\bar{1}00)$ of MnSb, as well as As-terminated (111) GaAs surfaces and the interface energy are of importance to be considered. The calculation procedures of the surface energy presented in the Sec. 3.2.2 can be extended to MnSb$(1\bar{1}00)$ surface and GaAs(111) surfaces for comparing their surface stability. Figure 3.5 shows the bulk truncated $(1\bar{1}00)$ oriented surface models exposing (a) Mn, (b) Sb-termination, and (c) As-terminated surfaces. Unlike (0001) surface, there are four possible positions for Sb atom as the termination labelled by Sb-termination I, II, III and IV. Atoms framed in the red boxes are fixed as a bulk environment. The stoichiometric surface energy are calculated by subtracting from the total energy of the slabs of the corresponding number of formula units in the bulk crystal, and adding the chemical potential of several number of Sb atoms in the slab as described in Equ. 3.13. The interface energy is defined as $\sigma_{\mathrm{inter}} = \frac{1}{A}\left(E_{n-\mathrm{MnSb/GaAs}} - E_{\mathrm{MnSb-Mn-termi}} - E_{\mathrm{GaAs-As-termi}}\right)$ where $E_{n-\mathrm{MnSb/GaAs}}$, $E_{\mathrm{MnSb-Mn-termi}}$, and $E_{\mathrm{GaAs-As-termi}}$ are the total energy of the

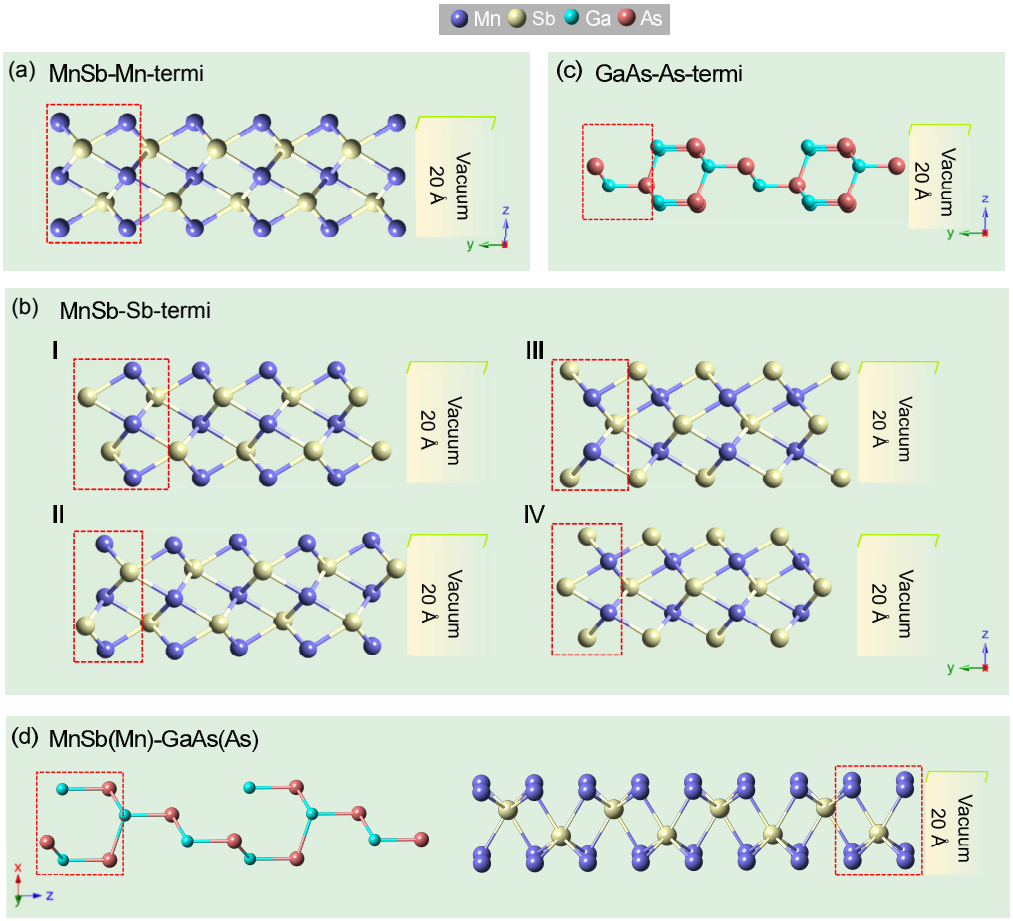

Figure 3.7: Slab models for n-MnSb $(1\bar{1}00)$ surface: (a) Mn-terminated, (b) different Sb-terminated, (c) As-terminated GaAs surfaces, and (d) n-MnSb(0001)/GaAs(111) interface. The layers in the red boxes are fixed.

slabs of n-MnSb/GaAs, Mn-terminated surface in MnSb, and As-terminated surface in GaAs.

In Table 3.5, we summarised the required total energy, the surface energy, interface enegy and the number of Mn and Sb atoms in different $(1\bar{1}00)$ and (0001) surface slabs. The corresponding information of As-terminated surface and n-MnSb/GaAs interface slab have also been tabulated in Table 3.5. In order to make results more clear, surface energies within the condition of Sb(As)- and Mn(Ga)-rich are simplified by an average value. Obviously, the σ_{GaAs} (0.470 eV/Å^2) is less than the sum of $\sigma_{\mathrm{top-surf}}$ and σ_{inter} (0.605 eV/Å^2) [satisfy condition (1)]. And the surface energy of top surface (0.095 eV/Å^2) is much lower than the surface energy of substrate surface (0.470 eV/Å^2) [satisfy condition (2)]. Finally, $(1\bar{1}00)$ Sb-terminated

surface has lower surface energy with 0.095 eV/Å^2 than Mn-terminating, but it is slightly higher than Sb-terminated (0001) surface (0.072 eV/Å^2) [satisfy condition (3)]. Therefore, the nano-islands nucleation is the result of surface and interface energy competition.

The morphology of MnSb nucleation is also affected by its growth kinetics. Therefore, the mobility of Mn and Sb atoms is influenced by the temperature, and the sequent total Gibbs free energy change, ΔG, for the nuclei formation can be expressed as

$$\Delta G = \Sigma \mathrm{A}_{\mathrm{MnSb}}\gamma_{\mathrm{MnSb}} + \Sigma \mathrm{A}_i\gamma_i + \Delta G_{\mathrm{Vol}}^{\mathrm{MnSb}} - \Sigma \mathrm{A}_{\mathrm{GaAs}}\gamma_{\mathrm{GaAs}}, \tag{3.14}$$

[104], where $\Sigma \mathrm{A}_{\mathrm{MnSb}}\gamma_{\mathrm{MnSb}}$ is the island surface energy [A_{MnSb} and γ_{MnSb} are the surface area and surface tension (resulting from greater attraction) of MnSb islands]; $\Sigma \mathrm{A}_i\gamma_i$ is the interfacial strain energy; $\Delta G_{\mathrm{Vol}}^{\mathrm{MnSb}}$ is the volume energy for the formation of the MnSb nucleus dependent on the temperature, T, and solute supersaturation, S, according to $\Delta G_{\mathrm{Vol}}^{\mathrm{MnSb}} = k_{\mathrm{B}}Tln(S)/v_{\mathrm{m}}$, v_{m} is the volume of the inclusion; and $\Sigma \mathrm{A}_{\mathrm{GaAs}}\gamma_{\mathrm{GaAs}}$ is the surface energy of GaAs before MnSb growth.

The lattice mismatch between islands and the substrate results in the occurrence of an interface strain field. This causes significant influences on the island growth kinetics during the thin film growth, *i.e.* an excess in activation energy barrier for the atomic diffusion to islands [105]. In the case of MnSb thin film growth, such increased energy barrier could limit the diffusion of Mn or Sb atoms, leading to the island formation on the surface of dissimilar underlying layers/substrates. The diffusion coefficient, D, can be determined via an Arrhenius relationship, $D \sim e^{\frac{E_{\mathrm{a}}}{kT}}$, where E_{a} is the activation energy for migration, k is the Boltzmann constant, and T is temperature. Therefore, the growth characteristics of the MnSb islands commonly rely on the interfacial energy distribution, temperature, and supersaturation condition.

Table 3.5: The total energy, the number of Mn and Sb atoms in the Mn- and Sb-terminated $(1\bar{1}00)$ surfaces, and their surface energies within Sb- and Mn-rich conditions.

	MnSb	Total energy	N_{Mn}	N_{Sb}	Surface energy		Surface energy
					Sb-rich	Mn-rich	Average
		(eV)			(eV/Å^2)		(eV/Å^2)
$(1\bar{1}00)$	Mn-termi	-13025.381	12	10	0.267	0.239	0.253
	Sb-termi-(I)	-10661.686	8	10	0.076	0.103	0.090
	Sb-termi-(II)	-11845.178	10	10	0.101	0.101	0.101
	Sb-termi-(III)	-10068.739	8	9	0.086	0.099	0.093
	Sb-termi-(IV)	-10068.687	8	9	0.088	0.101	0.095
(0001)	Sb-termi	-10069.847	8	9	0.061	0.082	0.072
	Mn-termi	-10066.639	9	8	–	–	–
	GaAs	Total energy	N_{Ga}	N_{As}	As-rich	Ga-rich	Average
		(eV)			(eV/Å^2)		(eV/Å^2)
(111)	As-termi	-18635.4608	6	7	0.424	0.519	0.470
	n-MnSb/GaAs	Total energy	N_{Mn}	N_{Sb}	N_{Ga}	N_{As}	Interface energy
		(eV)					(eV/Å^2)
	(0001)/(111)	-28694.647	9	8	6	7	0.51

3.4 Conclusion

Firstly, in the case of (1 × 1) n-MnSb(0001) surface, the present calculations show a Sb-terminated surface is more energetically favourable than Mn-terminated and Sb-monolayer-coated surfaces. Secondly, the As- and Sb-based TMP has been determined to understand the rule of surface stability and magnetic moment. The results with available candidates calculations show that the more stable structures are normally along with a lower magnetic moment except that the surface of NiAs and NiSb still keep the same paramagnetic characteristic. In addition, we also compared the surface energy and surface relaxation of Sb-based compounds. Finally, the reason of island formation when MnSb grows onto GaAs(111)B surface was explained by comparing the surface energy of (0001) and (1$\bar{1}$00) surface of n-MnSb, (111) GaAs surface and the interface energy of n-MnSb/GaAs. Of course, the growth mode depends not only on the properties of materials but also on the growth conditions (*e.g.* substrate temperature and flow-rates) experimentally.

Chapter 4

Surface reconstruction of (0001) n-MnSb surface - (2 × 2)

4.1 Introduction

This chapter describes a structual solution for the MnSb(0001) (2 × 2) based on DFT and LEED I-V techniques. First we review previous MnSb(0001) work at University of Warwick. We then compare to MnAs(0001) surface structure work reported in the literature.

The initial Warwick-based thin film growth of (0001) MnSb on different semiconductors has been done by Dr. Stuart Hatfield. He not only concluded the optimum growth conditions such as the best temperature of substrate ($T_{\mathrm{sub}} = 400$ °C) and beam equivalent pressure (BEP) ratio ($J_{\mathrm{Sb/Mn}} = 8$) [100], but also, as his main study, observed a number of surface reconstructions [*e.g.* characteristic (2 × 2), td(1 × 4), and ($2\sqrt{3}\times\ 2\sqrt{3}$)] of the MnSb(0001) during the growth of MnSb thin films onto GaAs(111)B substrates [106]. It has been shown that (2 × 2) reconstruction is the most favourable structure, and it can be acquired from other surface reconstructions by annealing at about 400 °C. Therefore, comprehensively understanding the atomic rearrangement of (2 × 2) surface and the resulting properties is of great importance for spintronic devices.

Subsequently, Dr. James Aldous carried on this job to try to solve the quantitative structure of (2 × 2) surface by using co-axial impact collision scattering spectroscopy (CAICISS) and LEED I-V simulations. He calculated four potential models including adatom, trimer, missing atoms and mixed structures on both Mn- and Sb-terminated surfaces, but all of the trial configurations had relatively high R-factors, and therefore bad agreement between experiments and simulations. Nevertheless, there is still one obvious trend which has been clarified based on his

calculations, namely these LEED simulations favour Sb-terminated structures [83].

More broadly, MnAs has been extensively studied, and several (0001) reconstructures [*e.g.* (2 × 2), (1 × 3) and the mixture of (2 × 2) + (1 × 3) phases] identified [20]. The (1 × 3) reconstructions are clearly related with (1 × 4) of MnSb, which are believed to be composed of long and narrow chain structures. For the dominant (2 × 2) phase, Ouerghi et al. inferred that the As-trimer and As-adatom model are promising compositions based on their scanning tunneling microscope (STM) results [20]. They then simulated (2 × 2) structures with As-trimer on Mn-terminated surface using ab initio calculations on account of their previous speculation [21]. But so far, there is no unambiguous answer about the exact surface atomic structures of (0001) (2 × 2) MnAs and MnSb surfaces.

In this chapter, possible (2 × 2) surface reconstructions have been proposed and comprehensively examined by structural modeling and theoretical calculations. The best (2 × 2) structure is found with lowest free energy and the lowest R-factor. Further interpretation of the mechanism of the surface reconstructions will be presented together with the bond characteristics, charge density difference of the surface atoms and density of states (DOS).

4.2 CASTEP calculations of (2 × 2) n-MnSb(0001) surface

4.2.1 Proposed models and computational conditions

4.2.1.1 Models

Four different kinds of surface models (adatom, trimer, vacancies and mixed terminations) of the (2 × 2) *n*-MnSb(0001) surface have been proposed in previous work [106]. Apart from calculating the models mentioned above, our calculations also considered dimer structures and the different adsorbed sites (HCP, FCC, and TOP) for all of the models. In total, thirty-two possible atomic configurations of (2 × 2) surface reconstruction have been taken into account, and the details are presented in Appendix A.

Here, all of the (2 × 2) structures are built up based on the Sb-terminated

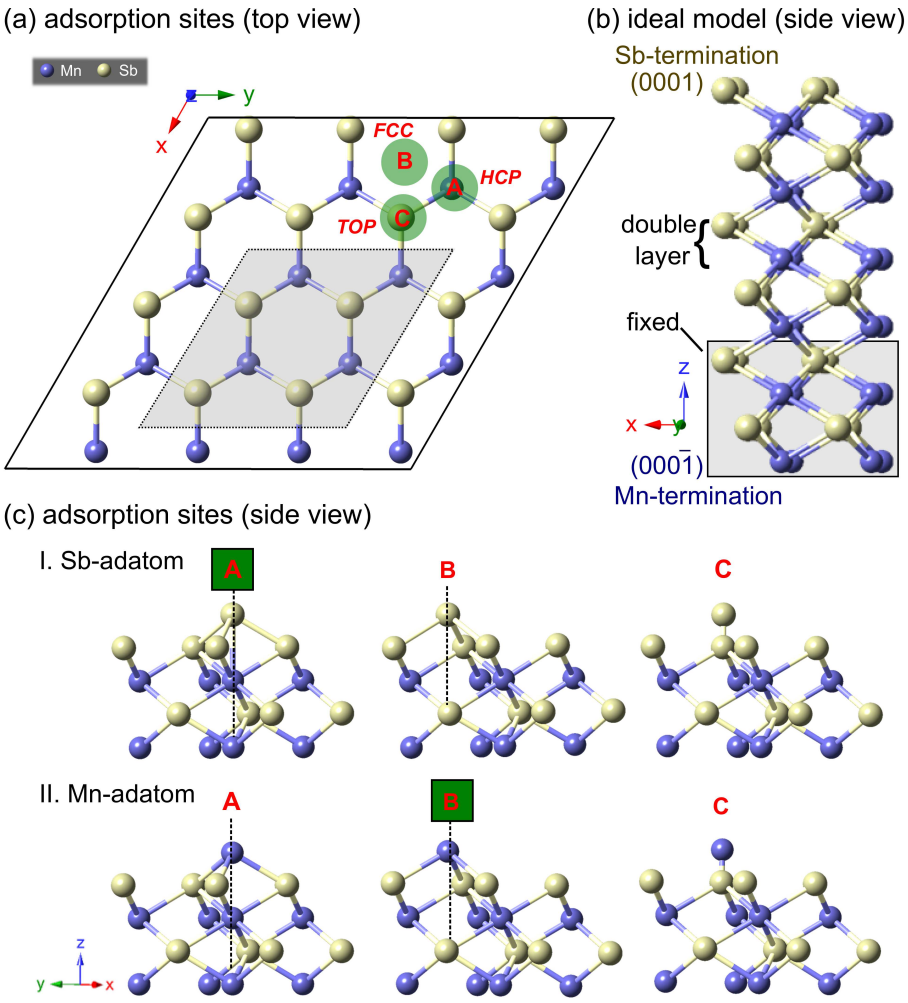

Figure 4.1: Clean atomic models of (2 × 2) *n*-MnSb(0001) surface (a) top view and (b) side view. (c) Schematic representation of one atoms (Mn or Sb) adsorbed onto Sb-terminated (2 × 2) surface with possible sites after geometry optimisation. Purple and yellow balls represent respectively manganese and antimony atoms. Green squares highlight the energetically favourable adsorption sites for Mn and Sb adatoms

(0001) surface, namely, we will adsorb Mn or Sb atoms on the Sb-terminated surface. This can be supported via three following evidences: (i) Dr. Aldous found the Sb-terminated structures are favourable for (1 × 1) and (2 × 2) identified by both LEED I-V calculations [83, 106], although he still could not solve the structure of (2 × 2). (ii) DFT favours Sb-(1 × 1) over Mn-(1 × 1) confirmed by our calculations shown in Sec. 3.1.2. (iii) Dr. Stuart Hatfield confirmed the Mn- or Sb-rich growth conditions are related with the beam equivalent pressure (BEP) ratio ($J_{\mathrm{Sb/Mn}}$), *i.e.* below (above) $J_{\mathrm{Sb/Mn}} = 6$ the growth is Mn (Sb) rich. In the experiment, $J_{\mathrm{Sb/Mn}} = 6.5$ was used so that the growth is Sb rich. This suggests that there should be sufficient

Sb for all the Mn arriving at the surface to form MnSb [83]. Therefore, trial (2 × 2) structures will be formed by some adatoms on the Sb-terminated bulk crystal.

Additionally, In order to quantitatively reflect surface film states caused by adsorption, the acceptor with even layers has to be chosen to ensure the same number of Mn and Sb atoms in the reference slabs. That means the Mn-rich conditions will be produced after adding different number of Mn atoms, and Sb-rich conditions is only correspond with adsorbed Sb atoms. Here, the surface was modeled by slabs consisting of six-double layers, as shown in Fig. 4.1(b), termed Sb surface (0001) and Mn surface ($000\bar{1}$), respectively.

Figure 4.1(c) demonstrates representative models with three possible adsorption positions: (i) a HCP site: placing the sites above atoms in the subsurface layer; (ii) a FCC site: placing at the centre of the hexagonal regions without atoms beneath; (iii) placing on the top of Sb atoms. Considering that every structure in either group I or II [shown in Fig. 4.1(c)] contains the same number of constituent atoms, the most stable surface structure can be determined by comparing their total energies directly. As a result, the optimal Sb-adatom place has been found to be the HCP site in Sb-adatom group, while the Mn adatom in group II prefers the FCC site (more details are shown in Appendix A). Six representative models ("1Mn-FCC", "2Mn-FCC", "3Mn-FCC", "1Sb-HCP", "2Sb-HCP", and "3Sb-HCP") are selected to be compared in the following section using the same approach.

4.2.1.2 Computational conditions

Four bottom layers (Mn-termination) were fixed to create a bulk-like environment, and the rest of layers were allowed to fully relax until each force component on the atoms reduce below 0.03 eV/Å. The basic parameters were: vacuum of 20 Å, cut-off energy 400 eV, $\boldsymbol{k}$-points (2 × 2 × 1), GGA exchange correlation functional, and on-the-fly pseudopotentials. Spin polarisation as an additional degree of freedom has been utilized in all of our designed models below so as to describe their magnetic characters.

Table 4.1: The total energy and the number of different atoms for the representative (2 × 2) surface reconstruction.

	N_{Mn}	N_{Sb}	Total energy (eV)	G (eV)	
				Mn-rich	Sb-rich
1Mn-FCC	29	28	-33756.073	8.757	9.067
2Mn-FCC	30	28	-34347.299	9.255	9.875
3Mn-FCC	31	28	-34938.459	9.819	10.749
1Sb-HCP	28	29	-33757.502	8.634	8.324
2Sb-HCP	28	30	-34350.117	9.050	8.430
3Sb-HCP	28	31	-34942.252	9.944	9.014

4.2.2 Gibbs free energy

The (2 × 2) surface reconstruction models with different number of constituent atoms are considered, which requires calculation of the full Gibbs free energy. The calculation procedures were carried out using the method outlined in Sec. 3.1.2. Reiterating briefly, the upper and lower limits of μ_{Sb} which are used for establishing the allowable ranges of chemical potential are given by,

$$\mu_{\mathrm{Sb}}^{\mathrm{bulk}} - \Delta H_f \leq \mu_{\mathrm{Sb}} \leq \mu_{\mathrm{Sb}}^{\mathrm{bulk}}. \tag{4.1}$$

$$G = E_{\mathrm{total}} - \mu_{\mathrm{Mn}} N_{\mathrm{Mn}} - \mu_{\mathrm{Sb}} N_{\mathrm{Sb}}. \tag{4.2}$$

The final correspondence between G and μ_{Sb} is

$$\begin{aligned} G &= E_{\mathrm{total}} - N_{\mathrm{Mn}} \left(\mu_{\mathrm{MnSb}}^{\mathrm{bulk}} - \mu_{\mathrm{Sb}}\right) - \mu_{\mathrm{Sb}} N_{\mathrm{Sb}} \\ &= E_{\mathrm{total}} - N_{\mathrm{Mn}} \mu_{\mathrm{MnSb}}^{\mathrm{bulk}} + (N_{\mathrm{Mn}} - N_{\mathrm{Sb}}) \mu_{\mathrm{Sb}}. \end{aligned} \tag{4.3}$$

Again, ΔH_f is the heat of formation on MnSb bulk; μ_{Mn} and μ_{Sb} stand for the chemical potential for Mn and Sb in the slab; $\mu_{\mathrm{Sb}}^{\mathrm{bulk}}$ is the chemical potential

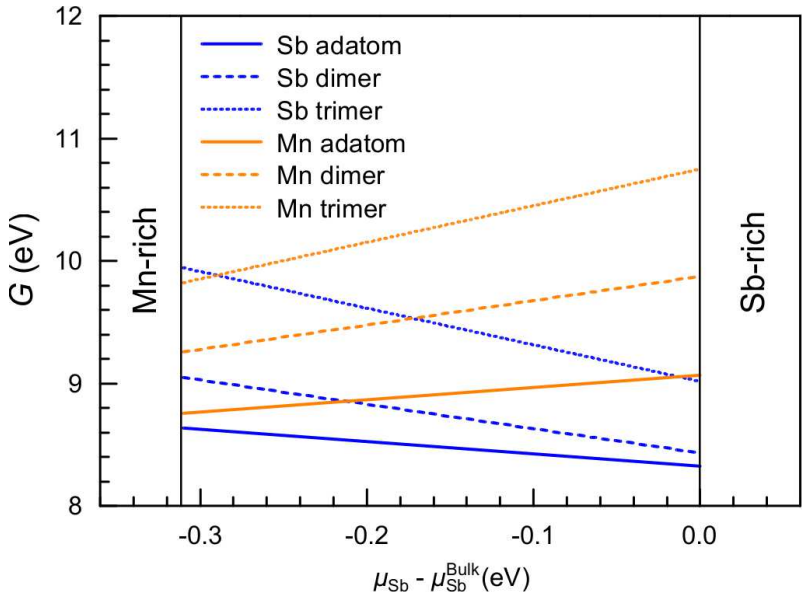

Figure 4.2: The Gibbs free energy for (2 × 2) surface reconstruction of *n*-MnSb(0001) as the function of the chemical potential of Sb. Blue and red colour stand for Sb and Mn adsorbed onto the reference surface, respectively. Solid, dash and dot lines are adatom, dimer, and timer models.

in Sb bulk system; E_{total} is the total energy of the slabs with different adsorption atoms; N_{Mn} and N_{Sb} are the number of Mn and Sb atoms in the individual slab. The geometry optimisation information arising from CASTEP as well as the derived Gibbs free energy (G) for the most stable models of adatom, two and three adatoms of Mn and Sb have been summarised in Table 4.1. The relevant Gibbs free energy (G) as the function of chemical potential were plotted in Fig. 4.2.

The most noticeable result obtained from Fig. 4.2 is single Sb atom plays an important role of (2 × 2) surface reconstruction, which exhibits the lowest free energy within the whole allowed range of chemical potential. More specifically survey these results, we can note that Mn-adatoms producing postive ΔN, $\Delta N = N_{\text{Mn}} - N_{\text{Sb}}$, slope up (three orange lines), while Sb-adatoms slope down (three blue lines). Additionally, comparing the configurations with the same coverage of adsorbed atoms of Sb and Mn (*i.e.* three categories here: Sb and Mn adatom; Sb and Mn dimer, as well as trimer), the Sb adsorbed structures are always energetically more favourable under the Sb-rich conditions in each category. A similar result appeared in a Mn-rich environment except that Mn-trimer starts to be more stable

than Sb-trimer. That suggests adsorbed Sb atoms are the predominant elements which contribute to the stablisation of the whole system. This phenomenon will be explained by band characteristics and density of states in the following sections.

4.2.3 Bond characteristics and charge density difference

For gaining further insight into the energy results corresponding to the stabilisation, bond characteristics together with charge density difference for trial structures has been shown in Fig. 4.3. Firstly, compared with Sb-dimer and trimer, Sb-adatom composition has the shortest bond length of d_1, which unsurprisingly made it become the most stable structure. Specifically, the adatom Sb atom tries to relax toward ideal bond position which creates the distance between Mn and Sb atom similar with bulk-like MnSb bonds (2.782 Å). For the case of Mn atom adsorption, all of the configurations show similar local arrangements [Fig. 4.3(d), (e) and (f)]. Manganese atoms tend to move down to the top surface and form the planar bonds with the three neighbouring Sb atoms at the distance of approximate 2.5 Å. The bond angle of Sb-Mn-Sb in the planar model is approximately 120° in average. It has been illustrated in the inset in Fig. 4.3(d). This movement is attributed to a significant amount of charge transfer (approximately 0.09e) from Mn-adsorbed atoms to Sb atoms just beneath in the third layer. In other words, Mn-adatom has to be squeezed in tightly bound with Sb atoms in the first layer to realise the charge transfer with the third-layer Sb atoms, thereby leading to Mn-Sb bond length far away with bulk equilibrium bond length (2.787 Å). These shorter bonds may cause repulsion force in Mn-adatom model rending it less stable in contrast to Sb-modified models. Overall, the most favourable configuration is constructed by one Sb adatom which is bonded to a complete Sb-layer at HCP site.

Figure 4.3 also displays the charge density difference of six proposed adsorption models in $(01\bar{1}0)$ plane. We find a small portion of charge depletion around adsorbed Sb atoms, however, the main bond characteristics is still strong covalent hybridisation between adsorbed atoms and their adjacent atoms of the first layer. It is evidential to conjecture that this bonding properties with partially covalent char-

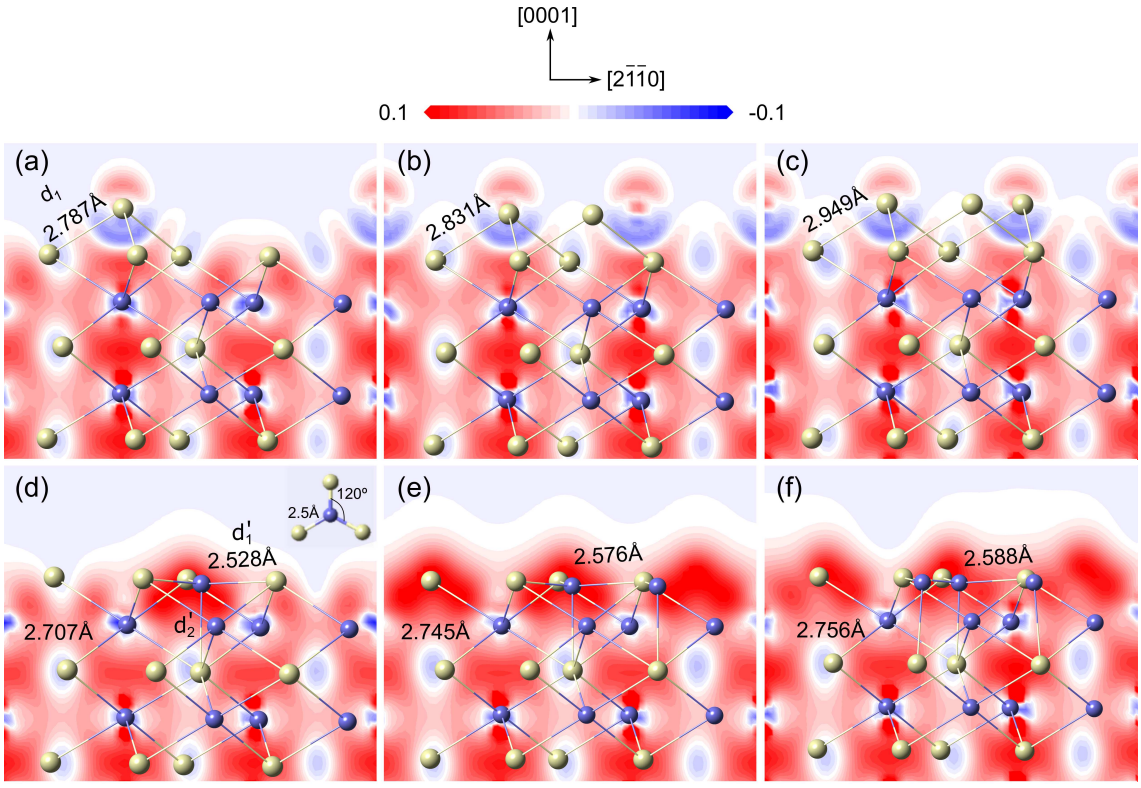

Figure 4.3: The charge density difference contours (unit of eV/Å^3) on (a) Sb-adatom, (b) Sb-dimer, (c) Sb-trimer, (d) Mn-adatom, (e) Mn-dimer, and (f) Mn-trimer in the (01$\bar{1}$0) plane. Blue and red denote charge depletion and accumulation. The bonding information for those trial structures is also illustrated in Fig. 4.3. d_1 is the bond length of adding Sb and the surrounding Sb atoms at the top layer. d_1' (d_2') is the bond length of adding Mn atoms with first layer Sb atoms (the third layer Sb atoms). The inset is the triplaner MnSb3 unit found at fcc sites on the top Sb surface.

acter assume a crucial role in surface reconstruction. As we know metal surfaces usually have no reconstruction except for metal Au [107–109], while semiconductors readily shows various reconstructed surfaces. From the perspective of formed covalent bond, it seems likely that MnSb surfaces incline to reconstruct in a way similar to how semiconductor surfaces reconstruct.

4.2.4 Density of states

Another important compensation for this stabilisation mechanism is evaluating the spin-polarised total density of states (DOS). Since the change in DOS is confined to the top three layers, the DOS of those layers in conjunction with adsorbed atoms has been analysed and shown in Fig. 4.4. It is widely accepted

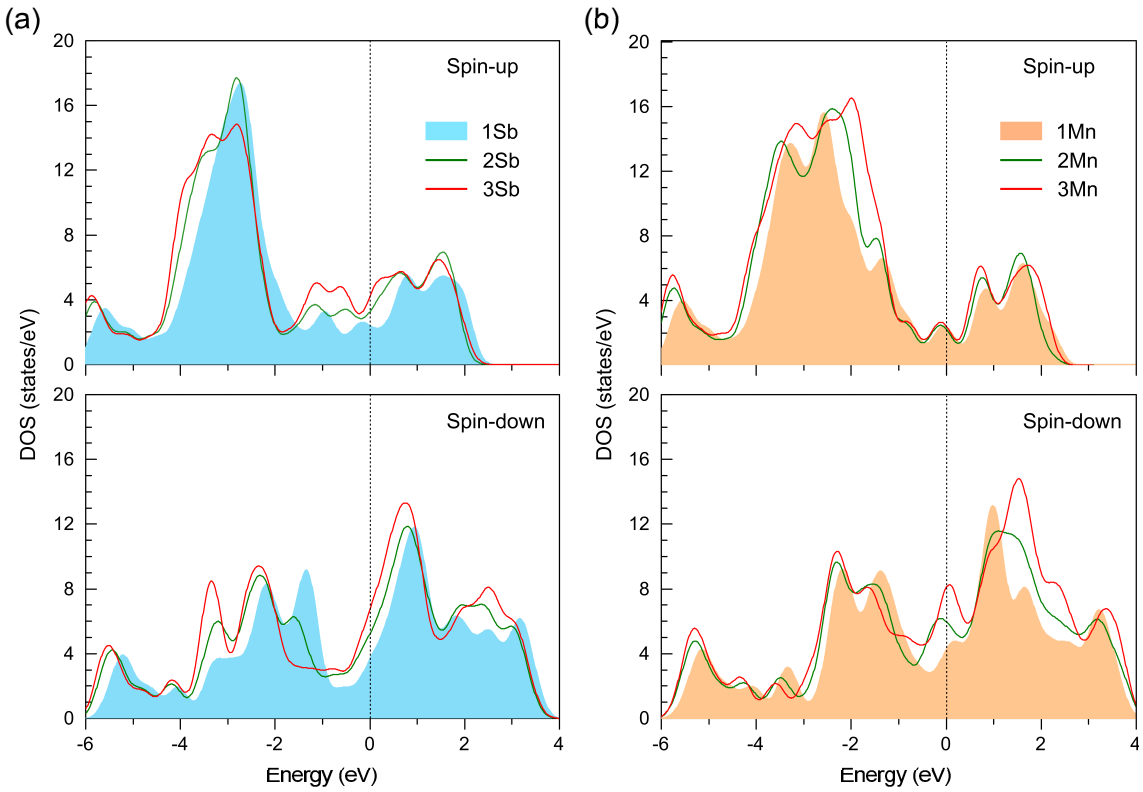

Figure 4.4: The total density of states of top three layers plus the adding atoms for trial six structures. (a) and (b) are spin-up and spin-down states of Sb- and Mn-adsorbed configurations. Blue hatched regions in all subfigures represent the states of single atomic adsorption; Green and red solid lines stand for dimer and trimer adsorption, respectively.

that the location of Fermi level relative to peaks and pseudogap in DOS determines the occupation of states and nature of bonding [110], which unsurprisingly will further influence the stability of the system. More explicitly, Jahn proved that orbital nonlinear molecule with a spatially degenerate molecules can not be stable, which states that systems normally tend to experience a geometrical distortion to remove the degeneracy, so-called Jahn-Teller effect [111]. Namely, if there is a peak, *i.e.* degenerate electron states, at Fermi level, the system will not be stable in order to remove the degeneracy. From our results shown in Fig. 4.4, the E_f of all of Mn-adsorbed compositions including spin-up and spin-down [Fig. 4.4(b)] almost lies at peaks, while that of Sb-adsorbed compositions especially for spin-down region falls at the deep valley. This suggests that the compounds of Mn as adsorbate are metastable. Recently, Pickard [112] also pointed out that the more stable configuration has the lower DOS value at the Fermi level using the Fermi-surface theory

proposed by Jones to interpret the distorted structure of bismuth [113,114]. Hence, our DOS results show that single-Sb adsorption is the most stable structure due to the lowest DOS for both spin-up and spin-down at Fermi level, following by Sb-dimer. The highest DOS at E_f is Sb-trimer seen in Fig. 4.4(a) and (b). This conclusion is in a good agreement with the stability results confirmed by Gibbs free energy. Furthermore, for the case of Mn-adsorbed systems, taking no account of spin-up DOS due to the same value of DOS at E_f, the DOS values follow the same rule in the spin-down. The individual Mn adsorption system with the lowest DOS value at the Fermi level is the most stable structure, whereas the Mn-timer compound is the most unfavourable configuration together with the highest DOS value at E_f.

4.3 CLEED analysis of n-MnSb(0001) - (2 × 2)

In order to experimentally check the atomic structure for (2 × 2)-reconstructed surface, the CLEED package [115] has been used to simulate existing LEED I-V data. Here, the atomic configurations discussed in Sec. 4.2.2 have been simulated, and the corresponding atomic coordinates fixed into CLEED files are generated after first-principles (CASTEP) calculations. All of the trial models include five reconstructed surface layers and four bulk-like layers, of which the input files of one example (Sb-adatom model) have been summarised in Appendix B. In this work, the entire atomic layers are permitted to fully relax in both lateral and vertical directions. Experimental results for LEED and phase shift calculation of Mn and Sb atoms have been carried out by Dr. James Aldous [83].

4.3.1 Sample preparation and LEED intensity measurements & calculations

A clean MnSb(0001) surface was firstly prepared in 10 second HCl etch in 18 M strength acid followed by rinsing in deionised water. This was blown dry under dry nitrogen source and immediately inserted into vacuum. The subsequent procedure was degassing at 300°C for 30 minutes, in situ Ar^+ ion bombarding at 500 eV for 10 minutes, and final flash annealing to 375°C. A typical (2 × 2) LEED

pattern with low background intensity was produced [116].

LEED intensity data was recorded at the normal incidence under computer control so that symmetrically equivalent diffracted beams indicate the same intensity [117]. LEED I-V curves was measured from 30 to 290 eV with 1 eV energy interval. Five symmetrically nonequivalent beams of (-1,0), (-2,1), (0,-0.5), (-1,0.5), and (0,-1.5) spots were measured.

4.3.2 R-factor and IV-curves

R-factor for the six adatoms structures considered in this chapter are shown in Fig. 4.5(a). It can be seen that Mn-adsorbed configurations have higher R-factor value than that of Sb-adsorbed structures overall. The best R-factor of 0.243 is "Sb-adatom" model in agreement with DFT results. The worst configuration is single Mn adatom with R-factor of 0.337.

The R-factor of Sb-adatom model (less than 0.35) is low enough to reflect the surface geometrical and chemical structure [86]. That means experimental and simulated I-V curves have good agreement. There are two main reasons that R-factor has been improved compared with Dr. James Aldous results (R-factor = 0.57) done in 2011. First one is that DFT calculations produce much more reliable structural information to establish more realistic surfaces for CLEED. Second one is that Aldous gave in-plane displacements forbidden, however, current job allowed three direction relaxation.

Figure 4.5(b) shows the atomic structures as well as interplayer spacing (Δd) derived from CASTEP and CLEED, respectively. Here, Δd_i ($\Delta d_i'$) (i = 1 - 5) stand for the interlayer spacings in CASTEP (CLEED). The relaxations along z direction from CASTEP to CLEED is calculated by $\Delta z = |\Delta d_i - \Delta d_i'| / \Delta d_i$, which are 2.4 %, 0.47 %, 0.85 %, and 0.51 % illustrated in Fig. 4.5(b). These low relaxation percentages suggest there is a good agreement between CASTEP and CLEED results.

In addition, the best (Sb-adatom model) and worst fit (Mn-adatom model) of experimental and calculated I-V curves has been shown in Fig. 4.6. A reliable R-factor is particularly sensitive to peak position but insensitive to the amplitude

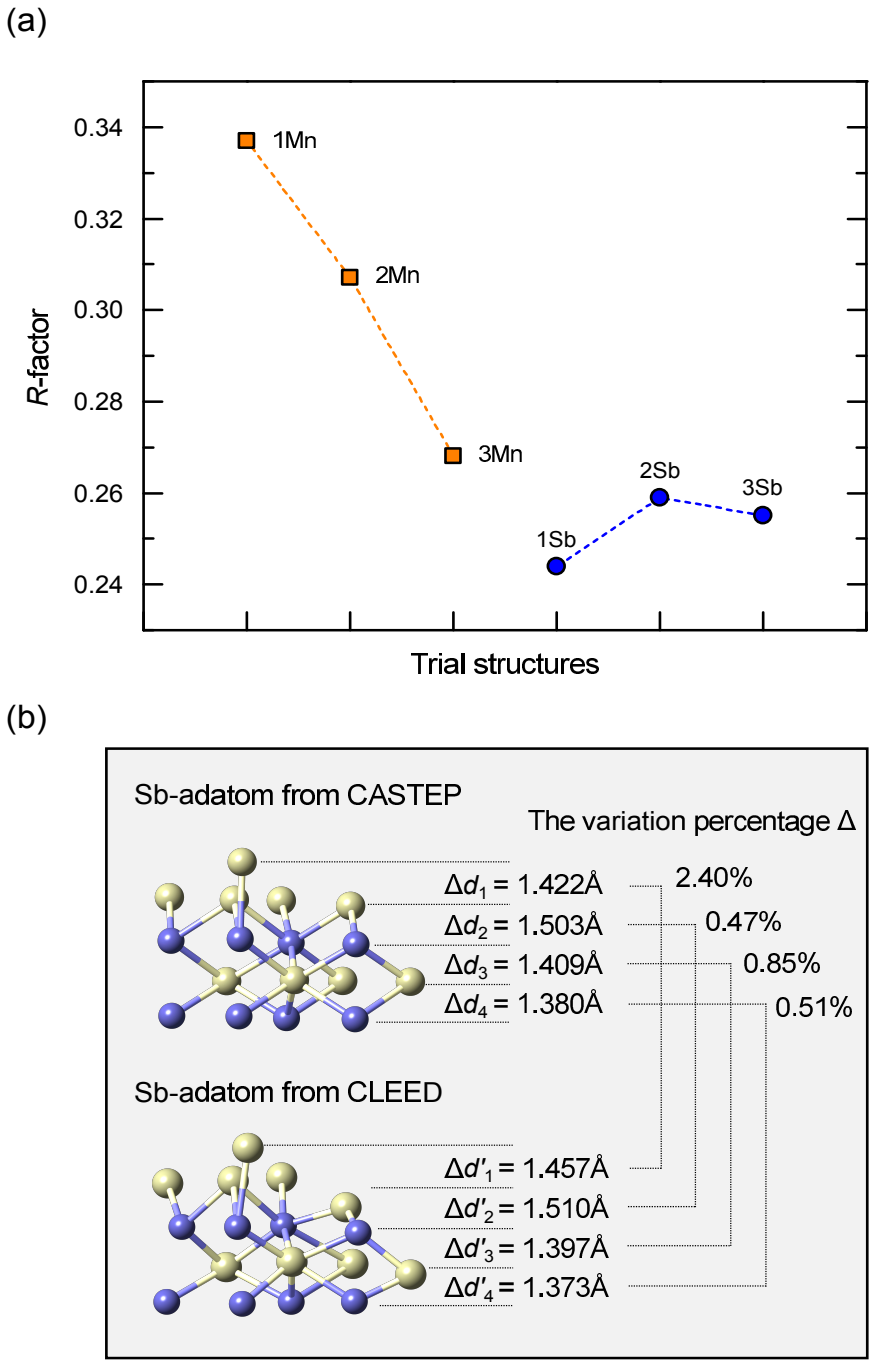

Figure 4.5: (a) The R-factor values of six proposed models (Sb- and Mn-adatom, dimer, and trimer) (b) The atomic structures as well as the interlayer spacing of the best-fit model derived from CASTEP and CLEED, respectively.

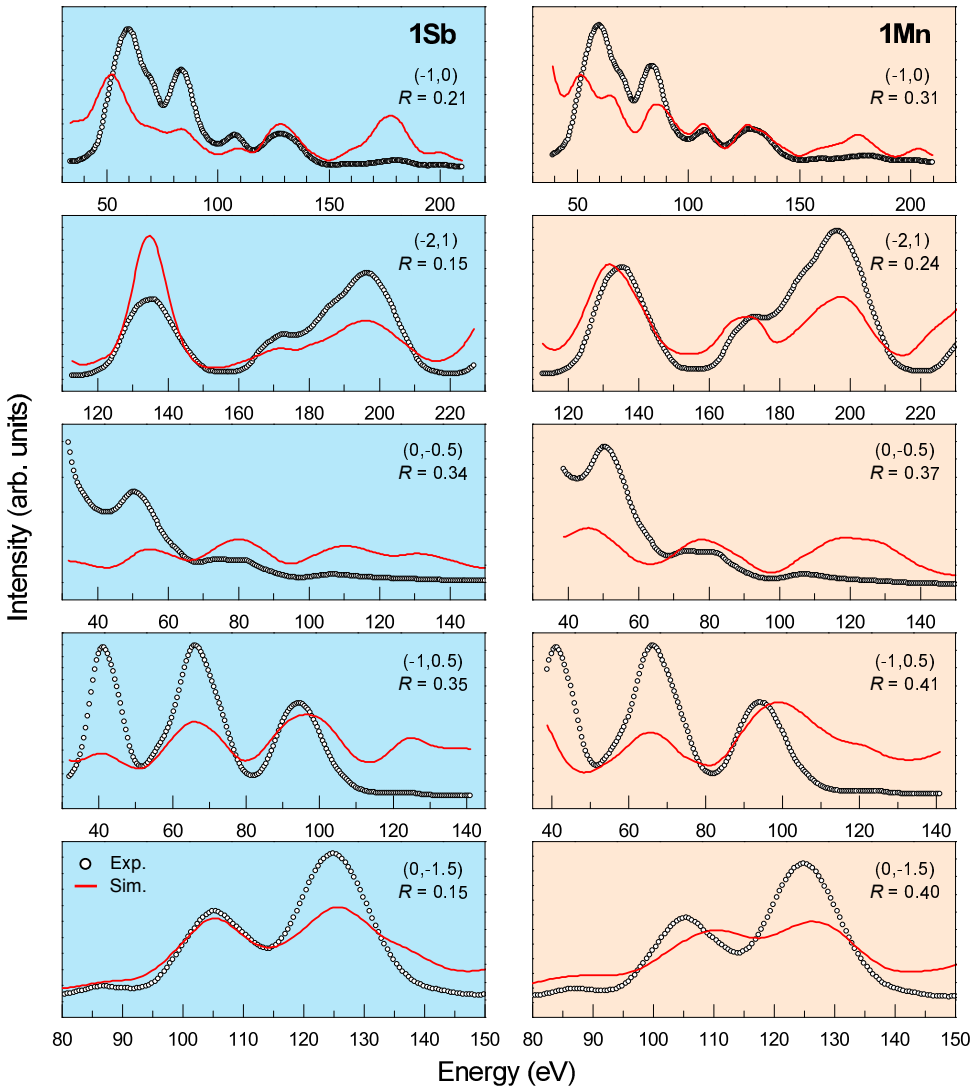

Figure 4.6: The best (Sb-adatom model) and worst fit (Mn-adatom model) of experimental and calculated I-V curves.

and the peak width of the signal [86]. It is because the positions of peaks (energies) are directly related to the geometry and well reproduced by theory, while intensities influenced by thermal vibrations, inelastic losses, and sometimes data collection techniques are less accounted for. Obviously, almost all peaks are shown at the same energy position in the calculated curves especially for Sb-adatom case. The indicates the R-factor is good enough to warrant the structure model.

4.4 Conclusion

Quantitative structures of (2 × 2) reconstructed MnSb(0001) surfaces have been determined employing a combination of DFT and LEED I-V methods. Overall, 32 possible configurations of different modification on Sb-terminated surface have been simulated in DFT, nevertheless, only 6 representative models were analysed and transferred to CLEED calculations. Our results clearly show that Sb adatom at HCP site significantly stabilise the Sb-terminated surface of MnSb forming the Sb-on-Sb (2 × 2) reconstruction. This is corresponds to both the lowest Gibbs free energy in DFT and the best R-factor in LEED simulation. Additionally, the atomic structures after CASTEP and CLEED calculations are compared. The low surface relaxations of 2.4 %, 0.47 %, 0.85 % and 0.51 % from the first interlayer spacing to the fourth one further confirmed the reliable results from both CASTEP and CLEED.

For the case of the most favourable Sb-adatom surface, the electronic properties of its bond characteristics and DOS shows the shortest bond length and lowest DOS value at the Fermi level based on DFT calculations. In addition, the surface bonding is found to have a strong covalent behavior in terms of charge density difference contour plotting. This suggests that MnSb surfaces incline to reconstruct in a way similar to how semiconductor surfaces reconstruct.

Chapter 5

Ga segregation from MnSb(0001)/GaAs(111)B system

5.1 Introduction

Molecular beam epitaxy (MBE) gives excellent control over layer thickness and composition but epitaxial materials do not always have the desired structure and composition profile. This can be due to competing epitaxial orientations [118, 119] or polymorphs [120, 121], or due to chemical intermixing between layers [122–124]. Segregation of atomic species across an interface or to the surface is common [125, 126]. This is potentially very important for spintronic devices which rely on sharp and well-controlled interfaces.

Segregation of Ga atoms from the substrate to the surface of the growing film has been observed for MnSb(0001) grown on GaAs(111) [17]. However, until now, there is no direct reason indicating the thermodynamic stabilisation mechanism, and no clear evidence revealing detailed structure for surface Ga enrichment. In this study, the X-ray photoelectron spectroscopy (XPS) and medium energy ion scattering (MEIS) methods were firstly employed by Dr. Aldous to observe the Ga segregation signal. Furthermore, first-principles calculations systematically demonstrate the reason for surface segregation by considering segregation energy. We also provid a detailed investigation of the optimal concentrations for diffused Ga dopants by comparing the substitution energy/surface energy change. Finally, structural and electronic information such as symmetry characteristics (bond length/bond angle), charge density difference, and density of states (DOS) for the Ga incorporation system are analysed. These calculated results can complement the corresponding experimental observations and also identify the underlying microscopic mechanism of Ga segregation the MnSb(0001)/GaAs(111)B system. This chapter will also carry

forward to the further defect of Ga segregation on a MnSb(0001) surface using the surface reconstruction reported in Chapter 4. This will give a more complete image of the real MnSb(0001) surface.

5.2 Experimental results

5.2.1 X-ray photoelectron spectroscopy (XPS), Medium energy ion scattering (MEIS)

To obtain the chemical information with regard to the composition of MnSb (0001)-(2 $\times$ 2) surface, a series of XPS and MEIS experiments were performed by Dr. James Aldous. In XPS measurements, samples were etched in HCl and annealed for 1 hour, followed by sputtering with Ar^+ ion bombard (IB) for 10 minutes [83]. With these treatments, all of data has been used to produce the XPS results in Fig. 5.1(a). It shows that an obvious and strong Ga 2p signal appears on the (2 $\times$ 2) surface, whereas there is no As appearence shown in the survey scan results. A zoomed image with the Ga signals is given in the inset of Fig. 5.1(a).

From the MEIS side, we used a double blocking geometry, whereby an incident H^+ beam was directed down a bulk high symmetry direction and the scattered H^+ ions were collected in a 2D detector. This detector records the energy of the scattered ions within 30 degree windows. These two dimensional datasets are analysed using kinematic scattering theory.

From Fig. 5.1(b), a number of important features are readily seen. The first is the two high intensity reflections which correspond to H^+ scattering from surface-bound Sb and Mn atoms. Both of these curves contain dips in the data at the same angle, with the angles of these dips corresponding to an exit trajectory along a high symmetry direction. However, there exists a small but clear signal between the Mn and Sb curves. The energy of this additional curve is consistent with H^+ scattering from a Ga atom. What is important to note is that the intensity of this additional curve does not diminish along the blocking angles, as we see for both Mn and Sb. This provides clear evidence of an ultra thin layer of Ga at the surface. It also exhibits two additional blocking dips [displayed by the arrows in Fig. 5.1(b)], which

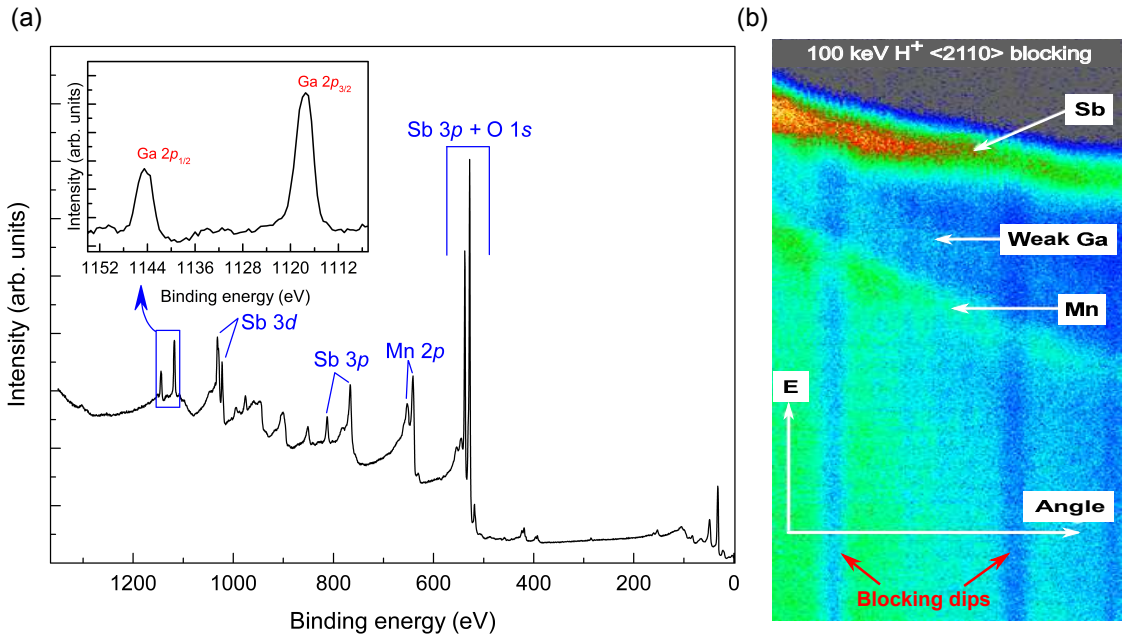

Figure 5.1: (a) XPS spectra for MnSb(0001)/GaAs(111)B sample. The zoomed image of Ga signals are shown in the inset; (b) Depth profiles of MEIS for MnSb(0001)/GaAs(111)B

means the Ga atoms are in the lattice sites. Namely, the substitution of Ga to Mn atoms might occur in order to follow the crystallography.

5.3 Theoretical results

5.3.1 Computation details

The exchange correlation functional of the generalized gradient approximation (GGA) type and the pseudopotentials of on-the-fly type were employed. Spin polarisation has been utilized as an additional degree of freedom in all of our models below so as to describe their magnetic characters. The energy cut-off value was set at 400 eV after a careful convergence testing for various bulk phases in this chapter including MnSb, GaSb, GaMn, Mn, Sb and Ga bulk. Fifteen atomic layers with 20 Å vacuum of Sb-terminated MnSb(0001) surface as a periodic slab are taken into account in order to ensure high accuracy. However, for the segregation energy section, 19-layered model structures were employed to present a clear segregation energy variation with more calculated date points. A (2 × 2) supercell was selected

correspond to experimental (2 × 2) reconstructed observation to be a pure host for creating new models from Ga substitution [106]. A 2×2×1 of $\boldsymbol{k}$-point sample by the Monkhorst-Pack scheme was used, and the atoms at the four bottom layers were fixed in all of models, other atomic positions were allowed to fully relax until each force component on the atoms reduced below 0.03 eV/Å.

5.3.2 Segregation energy

The surface segregation energy is the energy change when an impurity atom is transferred from interior sites towards the surface. A list of models have been built up by substituting one Mn atom using Ga from the first Mn layer (L_1) to the center Mn layers (L_6) shown in Fig 5.2(a).

The segregation energy can be given by

$$E_{\mathrm{Seg}} = E_i - E_1, \tag{5.1}$$

where E_i is the total energy of impurity-included (Ga substitution) slabs. i is the number of layer from the first Mn surface labelled by $P(1)$ in Fig. 5.2(a) to the inner Mn layer [$P(6)$], here $i = 1, 2...6$. E_1 is the total energy of the slab when Ga atom is doped into the first Mn layer.

Figure 5.2(b) indicates that the segregation energy increases significantly until the Ga atom is substituting at the third layer just acounting by Mn atom layers. The third, fourth till sixth Mn layer substitution shows the similar total energy. It is suggested that Ga atoms prefer to segregate to the surface areas (lower total energy) instead of staying inside the bulk (higher total energy).

Two initial reasons for explaining the basic nature of the Ga atom segregation are straightforwardly presented here: the annealing temperature and the lattice mismatch of MnSb/GaAs. Previous study suggests that the annealing temperature must be above 600 °C for achieving the As atoms diffusion from GaAs wafer [127]. However, for the Ga diffusion case, 420 °C can lead to GaAs decomposition to release Ga atoms [128]. In our experiment, the annealing temperature of 400 °C was used, thus outward diffusion of Ga atoms take place. Furthermore, the diffused Ga atoms would be dominately bonded with Sb atoms to form energetically more favourable

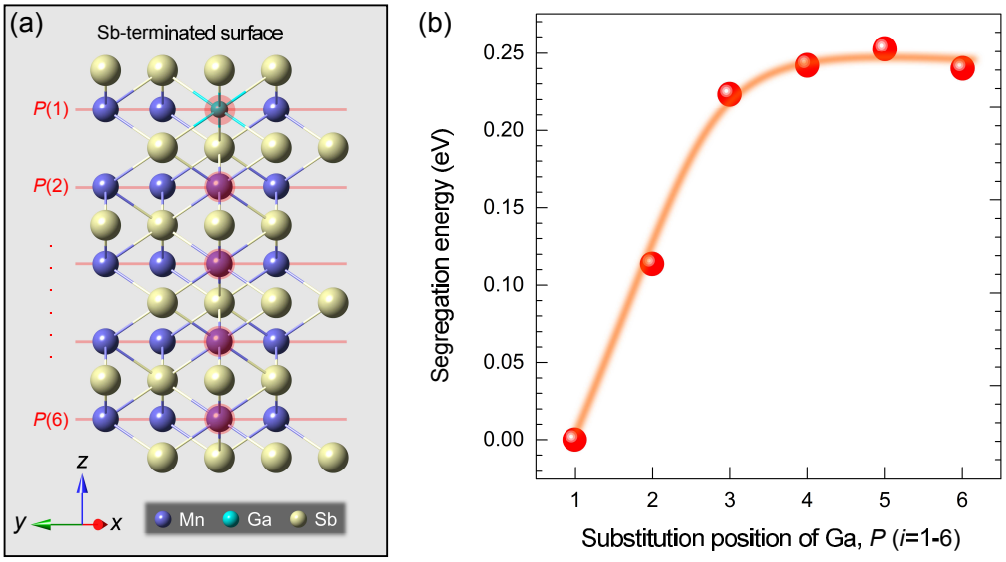

Figure 5.2: The side view of slab model with Ga substitution on the different Mn layers. Purple, green and yellow balls stand for Mn, Ga and Sb, respectively. (b) The Ga segregation energy profile calculated for six different Ga substitution positions (P = 1-6) in the different Mn monolayers of the MnSb slab.

GaSb bulk-like phase [ΔH_f(GaSb) = -0.42 eV] compared with the less stable MnSb [ΔH_f(MnSb) = -0.31 eV]. The relative heat of formation values ($\Delta H_f = E_{\mathrm{AB}}^{\mathrm{bulk}} - E_{\mathrm{A}}^{\mathrm{bulk}} - E_{\mathrm{B}}^{\mathrm{bulk}}$) have been shown in Fig. 5.3. Concurrently, vacancies created by Ga outward diffusion, near the MnSb/GaAs interface layers, could be theoretically compensated by the inward migration of Mn atoms to form MnAs on the basis of the relatively lower heat of formation about -0.64 eV. However, a high flux of Sb was used during growth, which results in no chance for MnAs formation experimentally. Here, one point which has to be highlighted is that the TEM result [Fig. 5.3(c)] done by Dr. Ana Sanchez clearly manifests the presence of GaSb at the n-MnSb/GaAs interface. And the GaSb huts are observed to be approximately 20 nm in height and orientated (111). The formation of the GaSb islands at the n-MnSb/GaAs interface is not due to the diffused Ga atoms but to excess Ga droplets resulting from the surface preparation. From the other angle, even though GaAs (-0.67 eV) possesses the most stable structure of these four materials, nevertheless, it has to provide the Ga atoms to recrystallise and to minimise the total energy of the MnSb/GaAs system. This dynamical process includes the formation of new phases (GaSb) and

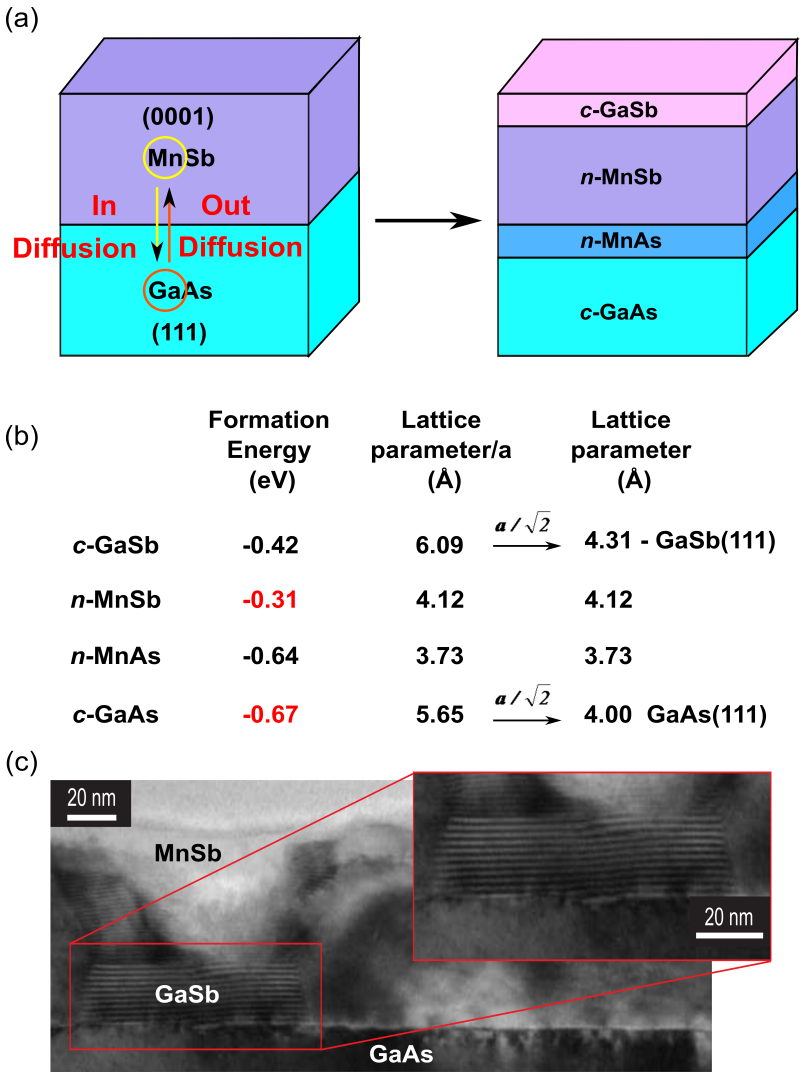

Figure 5.3: (a) The schematic diagram of MnSb thin film growing onto GaAs substrate, and the possible coexisted phases after Ga(Mn) diffusion (out-diffusion) based on theoretical prediction. (b) The formation energy of the relative phases, and their lattice parameters along x direction as well as the lattice parameters of (111) plane for GaSb and GaAs. (c) The TEM image of the GaAs/MnSb interface indicating the presence of GaSb phase. The inset shows a zoom view of the crystallite.

the dissociation of initial phase (MnSb).

Additionally, a certain stress can be readily induced due to the existence of different sizes for various elements in the MnSb(0001)/GaAs(111)B system, which will lead to the entire crystal lattice being distorted subsequently causing strain. In order to alleviate the strain, some misfit atoms in these composition have to be sent to the surface. Here, the lattice mismatch between n-MnSb(0001) and GaAs(111) is $\epsilon = (a_{\mathrm{GaAs}} - a_{\mathrm{MnSb}})/a_{\mathrm{MnSb}} \approx -2.91\%$ ($a_{\mathrm{MnSb}} = 4.12$ Å and $a_{\mathrm{GaAs}} = \sqrt{2}/a = 4.00$ Å). Therefore, in the course of the strain relaxation, the elastic energy could be minimised by pushing Ga atoms to the surface.

Overall, we infer that the whole system will intermix with GaAs, GaSb and MnSb from the substrate to the surface if Ga segregation arises.

5.3.3 Chemical potential, substitution energy and surface energy change

Based on the calculation of segregation energy, we have confirmed the experimental observation that Ga atoms segregate to the surface. In this section, we will go a further step to inspect the surface segregation quantity by analysing substitution energy and surface energy change. Considering the materials of MnSb(0001) and segregated Ga atom which can be regarded as ternary compounds to some extent, a graphical triangle method will be helpful to present chemical potential. The three axes stand for the three elemental chemical potentials [96]. In chapter 3, the allowable ranges of chemical potential for Mn and Sb in MnSb bulk phase are demonstrated. By analogy, the chemical potential of Ga and Sb atoms in GaSb phase, as well as Ga and Mn in GaMn phase can also be calculated. The heat of formation and the derived chemical potential ranges in different bulk phases are listed in Table 5.2. Additionally, the structure information and calculated chemical potential of required materials are summarized in Table 5.1, apart from the relative information for Mn, Sb and MnSb bulk which are shown in Table 3.2 in Chapter 3.

Using information from Table 5.2, the equilibrium phase diagrams of these three binaries are plotted in Fig. 5.4. Specifically, line 12, line 34 and line 56 correspond to MnSb, GaSb and GaMn phase, respectively. This new created region

Table 5.1: Structure parameters of the most stable phase for various bulk materials and the chemical potentials calculated by DFT total energies per unit cell.

Compounds	Space group	Lattice parameters (Å)			Chemical potential (eV)
		a	b	c	$\mu^{\text{bulk}}_{\text{AB/A}}$
Ga	CMCA	4.49	7.63	4.52	-2148.97
GaSb	F-43M	5.94	5.94	5.94	-2742.11
GaMn	R-3M	12.61	12.61	8.04	-2741.02

Table 5.2: The heat of formation for MnSb, GaSb, and GaMn, and the allowed range of chemical potentials for every element in the environment of MnSb, GaSb, and GaMn.

Species	Heat of formation (eV)	The range of chemical potentials (eV)
MnSb	0.31	-592.04$\leq \mu_{\text{Mn}} \leq -591.73$
		-593.03$\leq \mu_{\text{Sb}} \leq -592.72$
GaSb	0.24	-2149.39$\leq \mu_{\text{Ga}} \leq -2149.15$
		-592.96$\leq \mu_{\text{Sb}} \leq -592.72$
GaMn	0.14	-2149.29$\leq \mu_{\text{Ga}} \leq -2149.15$
		-591.87$\leq \mu_{\text{Mn}} \leq -591.73$

Table 5.3: The data of μ_{Mn}, μ_{Sb}, and μ_{Ga} about six special point

	point	μ_{Mn} (eV)	μ_{Sb} (eV)	μ_{Ga} (eV)	$\mu_{\mathrm{Mn}} + \mu_{\mathrm{Sb}} + \mu_{\mathrm{Ga}}$ (eV)
line1-2	1	-592.04	-592.72	-2148.94	-3333.70
(MnSb)	2	-591.73	-593.03	-2148.94	
line3-4	3	-591.59	-592.96	-2149.15	-3333.70
(GaSb)	4	-591.59	-592.72	-2149.39	
line5-6	5	-591.73	-592.68	-2149.29	-3333.70
(GaMn)	6	-591.87	-592.68	-2149.15	

surrounded by the highlighted blue lines defines an allowed scope within which Mn-Ga-Sb will be stable. The chemical potential varied by the elemental constitution can be extrapolated numerically following the basis vectors (denoted by green arrows) as illustrated in Fig. 5.4. The chemical potential values of Ga, Mn and Sb atoms at the six extreme conditions are tabulated in Table 5.3. It is also noted that the gradations of each axis have the equivalent magnitude, so the summation values of three chemical potentials at every point in the triangle figure must be constant. This constant value is approximately equal to the chemical potential of Mn-Ga-Sb which is -3333.70 eV listed in Table 5.3.

After acquiring the specific values of chemical potentials at six extreme points, the substitution energy (E_{Sub}) and surface energy change ($\Delta\gamma$) can be calculated. Several models of different Ga concentrations (0.25 ML, 0.5 ML, 0.75 ML and 1 ML) substituted on the subsurface Mn layer have been designed. The reason that substitutional geometries are entirely focused upon is because of their lower formation energy when compared with the the interstitial defect case, which will be shown in Sec. 4.3.5. Here, a single Ga atom implantation stands for 0.25 ML coverage. Note that the total energy calculations for 1Ga and 4Ga substitution will not rely on the impurity sites due to the symmetry of the pure (2×2) supercell. However, two

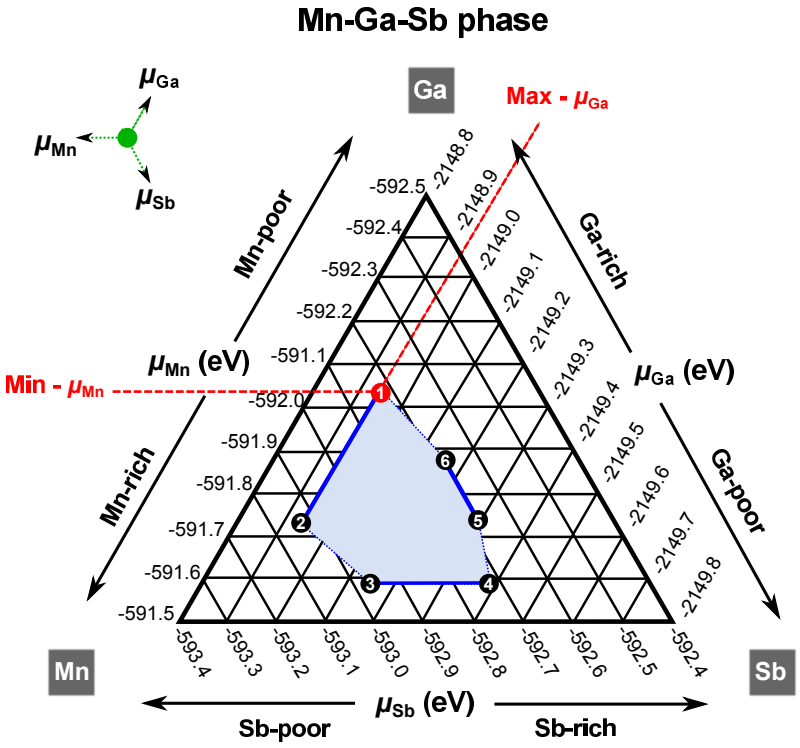

Figure 5.4: The chemical potential of Mn, Sb, and Ga being thermodynamically stable in GaMn, MnSb and GaSb phase. Three edges of a triangular image signify these three elemental chemical potentials μ_{Mn}, μ_{Sb}, and μ_{Ga}. The environment is denoted by "*poor*" and "*rich*" conditions on the basis of the magnitude of the chemical potential.

different isomers along with distinct Ga replaced positions have to be taken into granted of 0.5 ML and 0.75 ML coverage, respectively, and the configurations with lower total energy were chosen to calculate the substitution energy and compare with other coverages.

The substitution energy [129] and surface energy change [130] of Ga implantation can be defined by

$$E_{Sub} = \frac{1}{n}(E_{\mathrm{total}}^{n\mathrm{Ga-defect}} - E_{\mathrm{total}}^{\mathrm{MnSb}} + n\mu_{\mathrm{Mn}} - n\mu_{\mathrm{Ga}}), \tag{5.2}$$

and

$$\Delta\gamma = E_{\mathrm{Sub}} \times \frac{n}{A}, \tag{5.3}$$

Here, n and A are the number of Ga atoms in the system and the surface area

of the slab, respectively. $E_{\text{total}}^{n\text{Ga}-\text{defect}}$ is the total energy of the surface slab where defect occurs. $E_{\text{total}}^{\text{MnSb}}$ is the total energy of a defect-free surface.

The substitution energy results of different Ga coverages are illustrated in Fig. 5.5(a). It can be seen that the Ga-substituted derivatives prefer to stabilise at point 1 and 6 environment. If we turn back to Fig. 5.4, we could see these two points have relatively similar elemental conditions of poor Mn and rich Ga. That is to say Ga replacing Mn can indeed reduce the total energy of the whole system and produce more stable structures. Hence, the Ga substitution energy and surface energy change with the most stable conditions at point 1 were selected to be plotted in Fig. 5.4(a) inset and 5.4(b). The point 1 is expected to be more favourable of Ga substitution on Mn atoms obviously for Min$-\mu_{Mn}$ and Max$-\mu_{Ga}$.

The insert of Fig. 5.5(a) and Fig. 5.5(b) show that negative signs are derived from both substitution energy and surface energy change, which straightforwardly means that the replacement Ga from Mn can improve the structural stability of thin films. More specifically, one Ga atom integration leads to the total energy decreasing by 0.19 eV seeing from Fig. 5.4(a) inserting figure. However, with the increasing number of Ga atoms, the absolute value of substitution energy, which is the ability of each Ga atom contributing toward the system stability, drops down from 0.15 eV, 0.1 eV to 0.03 eV associated with the coverage of 0.5, 0.75 and 1 ML, respectively. This might be because the Coulomb repulsive interaction between Ga atoms canceled out a portion of substitution energy [131]. Considering the entire Ga substitutions instead of per Ga atom, the effect of Ga integration (*i.e.* making the system have lower energy) is greater than the one created by repulsive force between Ga atoms (*i.e.* counteracting the energy reduction) until 0.75 ML on the basis of surface energy change calculation. At the full defect concentration, the influence of repulsive force has surpassed that of substitution, which makes the surface become less stable again even more Mn atoms have been replaced. Hence, the final stability of the surface can be directly reflected by surface energy change including the overall interaction of the whole surface system. Consequently, 3Ga replacement is the thermodynamic equilibrium phase.

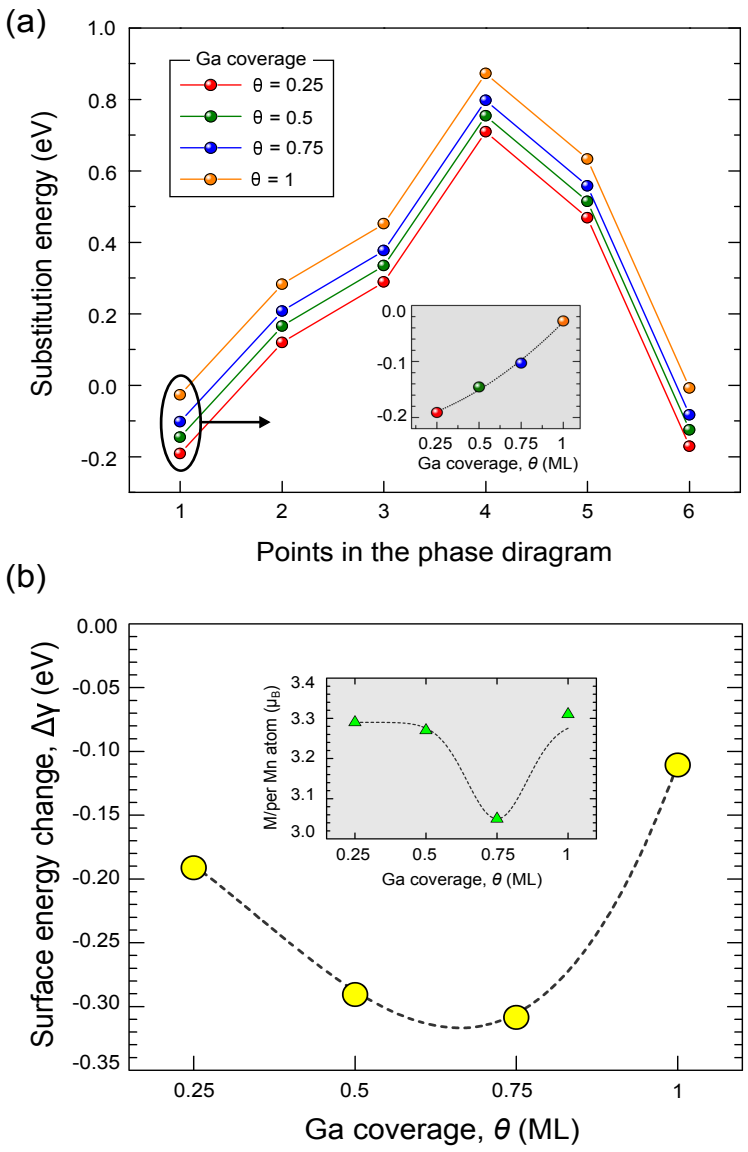

Figure 5.5: (a) The substitution energy created by Ga under the different coverage of 0.25 ML (red balls), 0.5 ML (green balls), 0.75 ML (orange balls), and 1 ML (blue balls) has been calculated by six readable and representative points in Fig. 5.4(a). The inset represents the formation energy for point 1. (b) The surface energy change for the diverse Ga coverage at point 1, and the inserted figure in Fig. 5.5(b) shows the magnetic moment per Mn atoms (M_{Mn}).

Furthermore, we also found that the calculated magnetic moment has a similar trend to surface energy change, which suggests that the system with relatively higher magnetic moment is more unstable. This is generally related with the spin of unpaired electrons, which are responsible for carrying magnetic moment. The magnetic moment typically becomes stronger as the number of unpaired electrons increase, while the stability of the system correspondingly decreases. Hence, full coverage of Ga atoms incorporated into Mn subsurface sites possesses the highest magnetic moment ($3.31\mu_{\mathrm{B}}$) as well as the highest surface energy change. This means that 3Ga atom substitution system has both the lowest magnetic moment and the lowest surface energy change.

5.3.4 Atomic structure after geometry optimisation

To show the Ga segregation effect for the MnSb/GaAs system, the geometric modification information of cubic MnSb and GaSb phase, as well as the most favourable configuration for each concentration are illustrated in Fig. 5.6. The bond length ($d_{\mathrm{Mn-Sb}}$ and $d_{\mathrm{Ga-Sb}}$) is calculated as the average distance between Mn/Ga atoms and the neighbouring Sb atoms. It is visible that the integration of Ga atoms causes a significant structural distortion and lattice change on the surface. From the coverage of 0.25 ML image, we can see that all three Sb atoms around the implanted-Ga on the top surface expanded out to try to make both the distance (2.665 Å) and the angle among Sb-Mn-Sb (108.794°) become *c*-MnSb-like (2.685 Å and 109.471 Å, respectively). These distance and angle were initially 2.777 Å and 96.428° before implanting Ga, which is because the impurities as well as surrounding Sb atoms in the slab prefer to be arranged following the zinc-blende structure of GaSb. It is expected that the resulting *c*-MnSb phase will possess a crystalline structure that resembles with GaSb. Specially, all of the bond distances between Mn and Sb for 0.25, 0.5 and 0.75 ML (2.665, 2.620, and 2.667 Å, respectively) tend to reduce to *c*-MnSb (2.685 Å) phase from 2.777 Å. Based on this atomic structural analysis, we speculate that *c*-MnSb formation can be induced by the segregated Ga atoms.

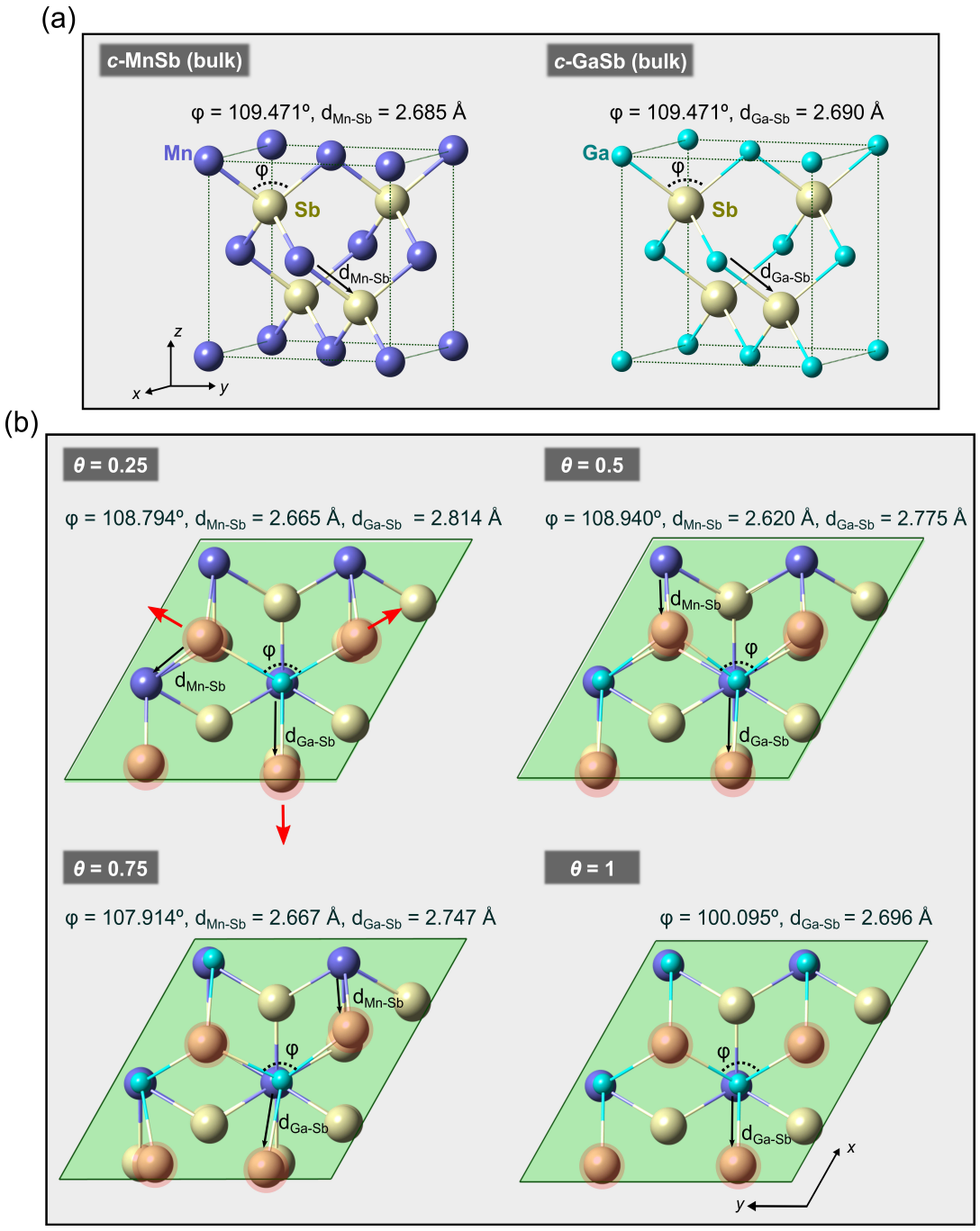

Figure 5.6: (a) The unit cell of cubic MnSb and GaSb with the bond length of Mn-Sb and Ga-Sb as well as the relative bond angle (ϕ). (b) Relaxed structures of selected Ga-substitution on Mn sites at the subsurface. Purple, yellow and green balls are corresponds to Mn, Sb and Ga atoms, respectively. The shade covered atoms are located on the top surface.

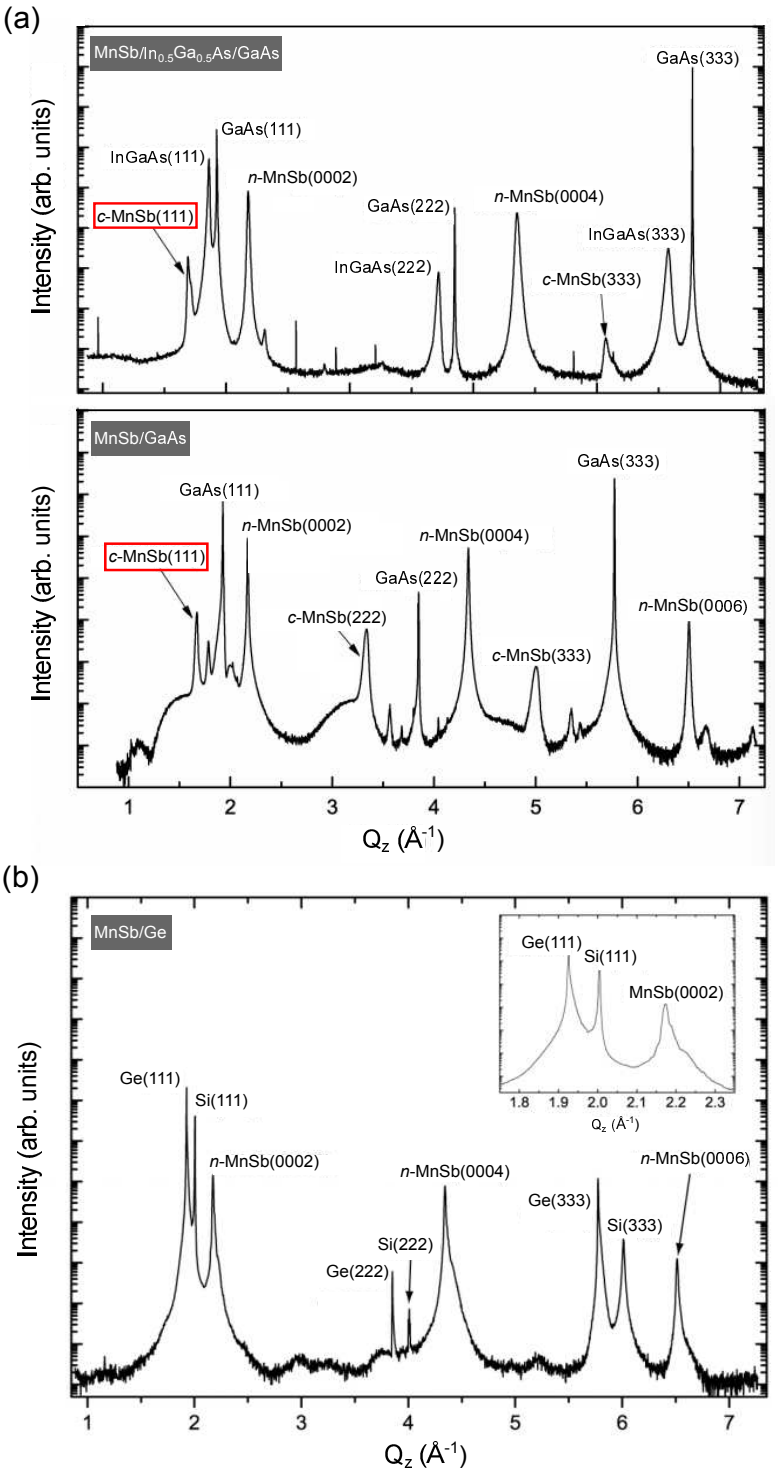

Figure 5.7: Triple axis out-of-plane XRD data for (a) MnSb/$In_{0.5}Ga_{0.5}As$/GaAs, MnSb/GaAs [132] and (b) MnSb/Ge [133] substrate.

The bond length between Ga and Sb atoms reduces to 2.696 Å at full coverage which is almost identical with the one in the bulk c-GaSb (2.690 Å). Obviously, to decrease the bond length of $d_{\mathrm{Ga-Sb}}$ from 2.777 Å, Ga atoms have to be pushed out to the surface, causing the corresponding bond angle (ϕ) to increase to 100.095° when compared with the one in the pure surface (96.428°). However, due to the limitation of hexagonal geometrical symmetry, the bond angles ϕ are not able to continuously increase to a c-GaSb-like angle. To the contrary, the mixture of Mn and Ga atoms leads to a geometrical symmetry breaking, subsequently creating an environment that ϕ can stretch freely and approach the c-GaSb-like value. In other words, Ga can be treated as a seed for growth of new phase c-MnSb.

Experimentally, Bell et al have published several papers related to MnSb growth on different substrates (*e.g.* GaAs, InGaAs [132] and Ge [133], which can be collected here to support our conclusion. On account of their XRD results illustrated in Fig. 5.7, it clearly shows that c-MnSb has appeared on both GaAs and InGaAs substrates including Ga elements, whereas it was not present on the Ge substrate. Namely, c-MnSb is readily formed when Ga atoms out-diffuse from GaAs and InGaAs substrates. To further confirm the function of Ga in promoting c-MnSb growth, some more simulations related with the n-MnSb/c-MnSb interface will be carried out in Chapter 6.

5.3.5 Charge density difference

Figure 5.8 displays the charge density difference contour maps of Ga substituted Mn sites at the different concentrations. A wide range of charge accumulation exist between Mn (Ga) and Sb atoms, leading to the dominant covalent chemical bonding formation along the ligands. Meanwhile, the small amount of electron depletion taking place around Ga atoms indicates their ionic characteristics. These charge redistribution of GaSb is attributed to the strong electronegativity and smaller size of Ga atoms, which is to say electrons simultaneously accumulate to Ga sites. As can be seen in Fig. 5.8, the strongest electron accumulation takes place at $\theta = 0.75$ML. This is further evidence for supporting 0.75 ML being the most stable system.

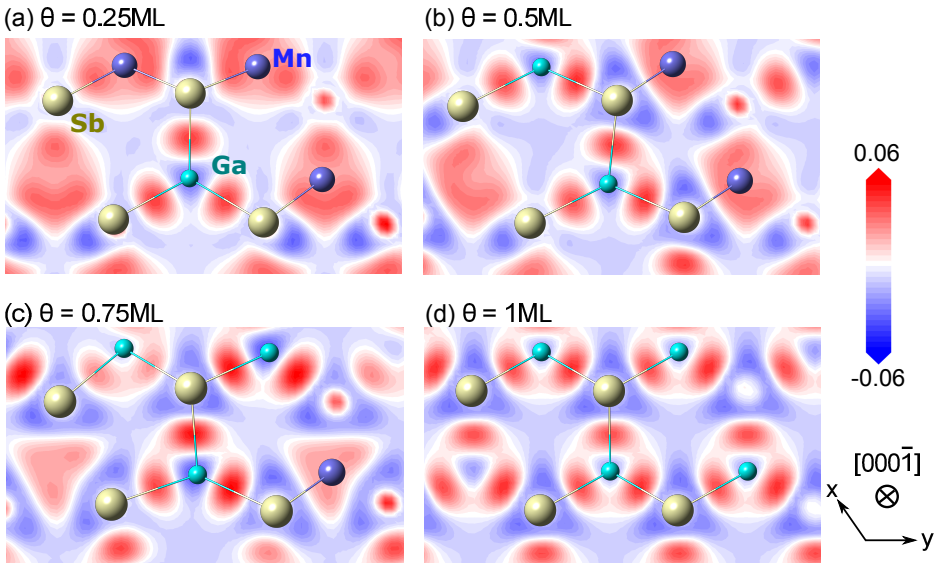

Figure 5.8: The charge density difference maps (unit of eV/Å^3) of the relaxed (0001) Sb-terminated surface with different coverage (a) $\theta = 0.25$, (b) $\theta = 0.5$, (c) $\theta = 0.75$, and (d) $\theta = 1$. Blue and red region stand for electron depletion and accumulation.

5.3.6 Preferred segregation positions (substitution and interstitial)

Another factor which has to be considered in this chapter is which sites diffused Ga atoms will tend to occupy. Dominant species of Ga implantation are substitution (Ga_{Mn}) and interstitial (Ga_i) cases, where several structures for both Ga_{Mn} and Ga_i have been constructed and structurally optimised. Figure 5.9 illustrates the representatives with the lower total energy for interstitial case from the concentrations of 0.25 to full coverage. Note that the initial interstitial Ga atoms are located at the center of the hexagonal channel without atoms beneath.

The site preference of Ga addition to MnSb(0001) surface either substitution or interstitial can be identified by comparison of the formation energy per Ga atom. The formation energy of substitution which is so-called substitution energy has been given in Equ. 5.2, while that of interstitial is defined as

$$E_{\mathrm{Int}} = \frac{1}{n}(E_{\mathrm{total}}^{n\mathrm{Ga-defect}} - E_{\mathrm{total}}^{\mathrm{MnSb}} - n\mu_{\mathrm{Ga}}), \tag{5.4}$$

where $E_{\mathrm{total}}^{n\mathrm{Ga-defect}}$ is the total energy of Ga-integrated structures on interstitial sites, $E_{\mathrm{total}}^{\mathrm{MnSb}}$ denotes the total energy of defective-free MnSb (0001) slabs, μ_{Ga} is the chem-

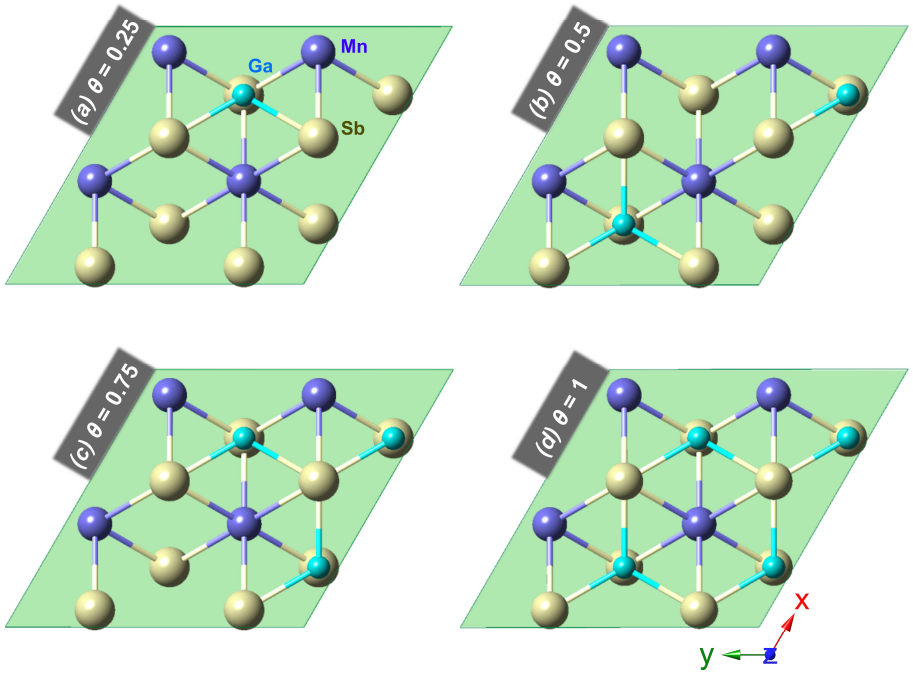

Figure 5.9: Schematic illustration of the proposed Ga interstitial compositions on the top-Sb surface for (a) $\theta = 0.25$, (b) $\theta = 0.5$, (c) $\theta = 0.75$, and (d) $\theta = 1$, respectively.

ical potential of Ga atom at six points which has been derived in Fig. 5.4 , and n represents the number of interstitial Ga atoms. It is noted that the calculated formation energies of Ga interstitial are positive values in the whole range of concentrations from 0.25 to 1 ML, suggesting the interstitial positions are not ideal sites for Ga. However, the configurations of Ga atoms substitute Mn sites has the specific stable conditions at Mn-poor and Sb-rich environment, which can be exhibited at point 1 and point 6 with negative formation energy. That is to say, all of the Ga-implanted atoms possess strong tendency to substitute Mn-subsurface sites rather than occupy top-surface interstitial sites consistent with MEIS results. Therefore, the atomic and electronic information (*e.g.* bonding characteristics and charge density difference) of substitution systems were mainly focused on above.

5.4 Conclusion

The segreation of Ga atom to the surface has been initially observed in experiment by the techniques of XPS and MEIS. The calculated the segregtion energy

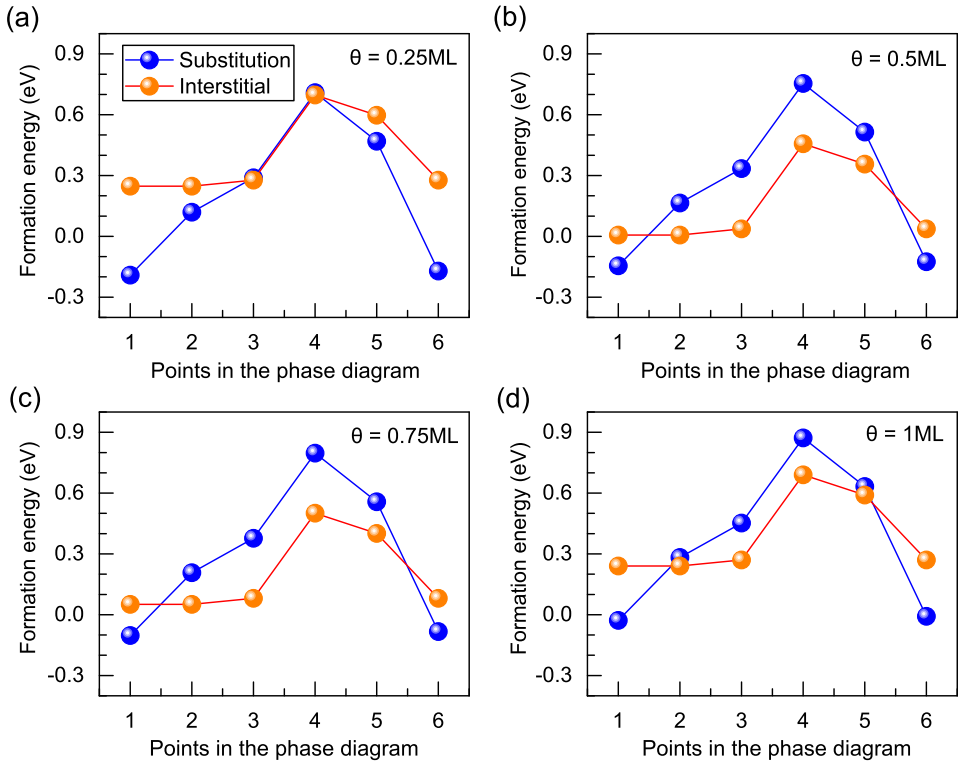

Figure 5.10: The formation energy of Ga_{Mn} (blue spheres) and Ga_i (orange spheres) cases for the coverage of (a) $\theta = 0.25$, (b) $\theta = 0.5$, (c) $\theta = 0.75$, and (d) $\theta = 1$.

from DFT further confirmed Ga atoms indeed diffused to the surface with lower total energy. Notably, in the process of segregation, only 0.75 ML Ga atoms appeared in the surface instead of a full monolayer. In terms of the segregation locations, the formation energy analysis also implies that Ga atoms have a greater tendency to replace the Mn atoms in the subsurface layer rather than to occupy the interstitial sites.

By analysing the atomic structures of the relaxed Ga-doped MnSb(0001) surface, we found that Ga atoms are more likely to account for the formation of *c*-MnSb in theory. Of course, the morphology of the product should also depend on reaction factors such as substrate temperature (T_{sub}) and the flux ratio (J). Numerious experiments performed by Bell's group in the University of Warwick already validated that the *c*-MnSb crystallites form on *n*-MnSb in the range of 6.6 to 7.5 of (J) with the $T_{\text{sub}} > 675$K [32]. The formation mechanisums of *c*-MnSb will be discussed in more detail in the next chapter.

Chapter 6

The formation and stabilisation of half-metallic c-MnSb polymorph

6.1 Introduction

TMP generally crystallises in hexagonal NiAs- or MnP-type structure in nature, and the formation of metastable zinc-blende structures is energetically unstable [40, 98]. Among this class of materials, a few experimental attempts have been made to stabilise cubic polymorphs such as c-CrAs and c-CrSb grown on GaAs(001) substrates, even though these thin films change to their stable non-HM ferromagnetic phases again within the growth thickness of 2-4 nm [101, 134]. Most recently, Dr. James Aldous under Dr. Bell's group (in Warwick Physics) prepared a mixture of bulk-like c-MnSb and w-MnSb polymophs in MnSb thin films epitaxially grown on GaAs(111) substrate by the MBE method [32]. On the basis of their experimental observations, some optimal growth conditions on the partially formed HM c-MnSb phases were suggested, *e.g.*, growth temperatures, T_{sub}, and ratios of Mn and Sb flux, J. A possible growth mechanism has also been speculated that a Sb-associated surface reconstruction may induce the change in atomic stacking order from ABAC to AaBbCc along the [0001] direction. However, further understanding on the formation of the stable c-MnSb polymorph in MnSb/GaAs heterostructures is still required provide experimental guidance.

In this chapter, we will explore the HM ferromagnetic properties of c-MnSb by first performing density of states (DOS) and electronic band structure calculations. Two representative bulk MnSb polymorphs (Niccolite and cubic phases) under the volume expansion/compression will be calculated to obtain optimal lattice parameters of the structures as well as to confirm the instibility of bulk c-MnSb. Following this, in order to interpret the formation mechanism of c-MnSb in

a MnSb(0001)/GaAs(111)B heterosystem, physically reasonable model structures and their calculated results will be presented and discussed together with experimental observations. Finally, a theoretical prediction of an innovative thin film growth regime, *i.e.* MnSb(0001)/GaSb(111), as a future experimental guidance to achieve *c*-MnSb, will be proposed.

6.2 Magnetic properties of c-MnSb bulk

To investigate the nature of HM properties and the total magnetic moment for *c*-MnSb, first-principle calculations on the electronic band structure and DOS have been carried out. The results shown in Fig. 6.1 indicate that *c*-MnSb has a typical HMF characteristic. Namely, the spin-up orbitals contribute a metallic behaviour at the Fermi energy, while the spin-down orbitals induce an insulating state with a direct band gap at the Γ point of 1.52 eV [40, 45]. This obtained band gap energy is similar with other results reported (1.54 eV) [45]. For the atomic bonding of *c*-MnSb, each Sb atom is surrounded tetrahedrally by four other Mn atoms. This local tetrahedral environment allows the hybridisation between the t_{2g} (namely d_{xy}, d_{yz}, and d_{xz}) states of the Mn atom and p states of Sb atoms mentioned in Sec. 1.5. It has been confirmed that such symmetry-induced hybridisation causes a repulsion interaction between Sb (p-orbitals) and Mn ($3d$ - t_{2g}) [135,136]. Hence, the derived t_{2g} states have extensively broad bandwidth for both majority and minority band structures as shown in Fig. 6.1. In the case of the $3d$ - e_g (d_{z^2} and $d_{x^2-y^2}$) states, there is no orbital interaction between Mn $3d$ - e_g and Sb p orbitals due to the far distance of the orbitals, resulting in the formation of flat and narrow e_g bands. We can also observe that these two spin band structures are similar, but the e_g and t_{2g} bands in the minority spin shift up above the Fermi level. This gives rise to a large bonding-antibonding splitting with an increase in exchange interaction energy and band gap energy [137, 138]. Other electronic properties obtained by DOS calculations are also illustrated in Fig. 6.1. The majority of bonding states is dominated by d states [see the orbital distribution nearby and below the Fermi level in Fig. 6.1(a)], and the antibonding states show more p-like characters. For

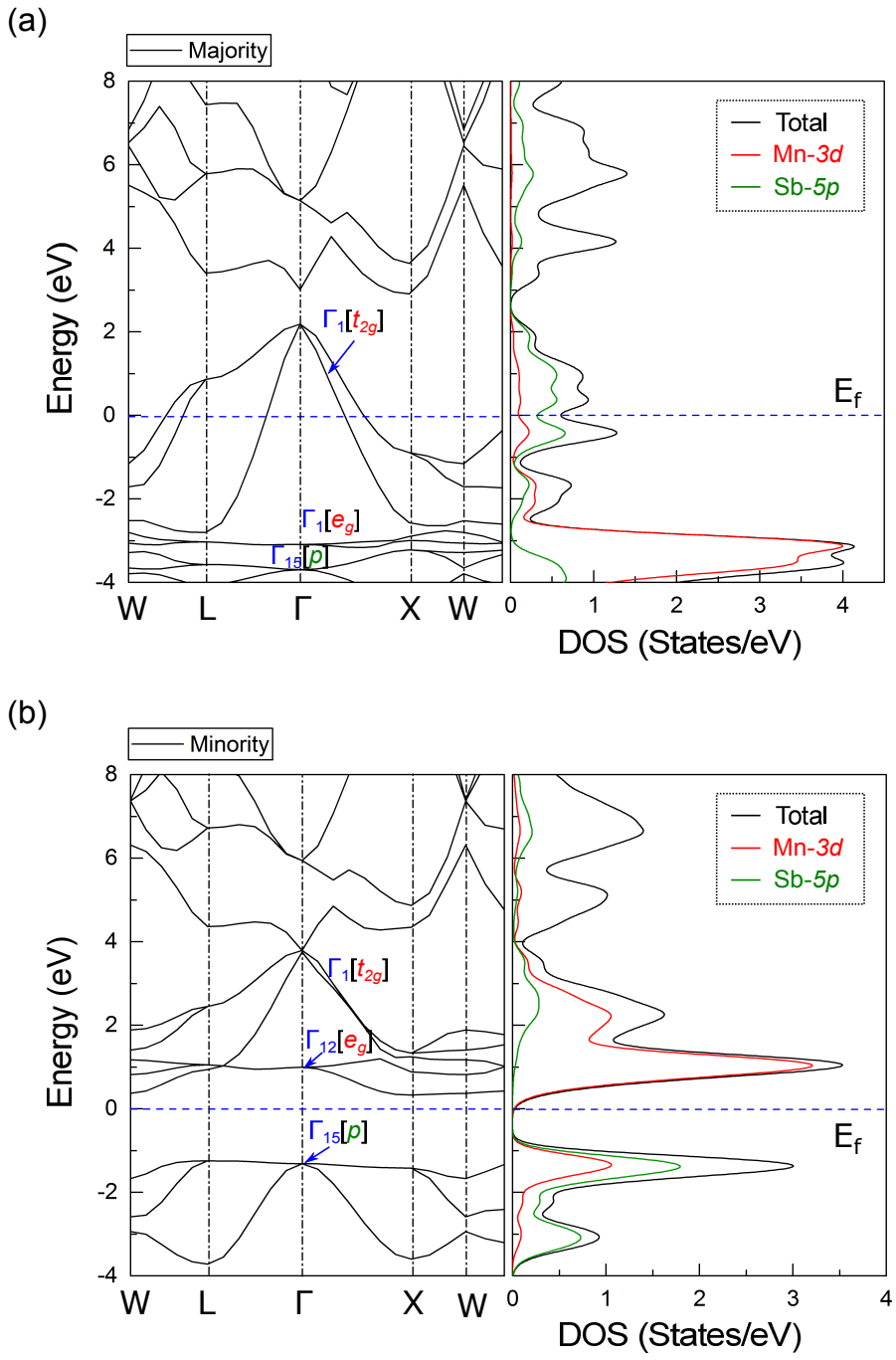

Figure 6.1: Band structure and DOS around Fermi level of bulk MnSb in the zinc-blende (B3) structures. Spin-dependent bands are shown in the upper panel (Majority) and bottom panel (Minority) with the letters at the bottoms manifesting the high symmetry points in the Brillouin zone. The originating orbitals of bands and corresponding characteristics are denoted by p, t_{2g} and e_g. Black, red and green curves in DOS stand for total, Mn-*3d* and Sb-*5p* orbitals, respectively.

the minority spin [Fig. 6.1(b)], the situation is the other way around. That is to say the bonding states are mainly contributed by p orbitals, whereas the antibonding bands are most likely formed by d orbitals.

The spin-magnetic moment (integrated spin-up DOS minus integrated spin-down DOS at the Fermi level) of *c*-MnSb per unit cell is $4\mu_B$ calculated in this thesis. The Mulliken populations in CASTEP show that Mn atoms contribute the prominent magnetic moment of $2.32\mu_B$, and Sb atoms give $-0.32\mu_B$. As proposed by Galanakis and Mavropoulos [139], the total magnetic moment is also complied by the semi-empirical Slater-Pauling rules of binary half-metallic magnets below:

$$M_t = (Z_t - 8)\mu_B. \tag{6.1}$$

where M_t and Z_t are the total spin magnetic moment per formula unit and the number of valence electrons, respectively. The analogue behaviour is also found in many Heusler alloys with different rules as 'rule of 18, $(Z_t - 18)\mu_B$' or 'rule of 24, $(Z_t - 24)\mu_B$' [140,141]. For the electronic configuration of MnSb, the outermost shell is composed by $Mn^{3+} : 3d^5 4s^2$ and $Sb^{3-} : 5s^2 5p^3$. Therefore, the valence electrons of *c*-MnSb is 12, leading to an integer of Bohr magneton ($4\mu_B$). Consequently, the calculated spin-up and -down DOS, and total magnetic moment of *c*-MnSb prominently indicate HM characteristics.

6.3 Phase equilibrium of MnSb bulk (c-MnSb and n-MnSb)

6.3.1 Computation details and method

As presented in Chapter 1, MnSb tends to form the hexagonal NiAs-type structure rather than the cubic structure. To examine their structural stability, the equilibrium lattice constants of *n*- and *c*-MnSb are calculated by fitting the total energy based on the Murnaghan-Birch equation of states [142, 143],

$$E(V) = E_0 + \frac{9V_0B_0}{16}\left\{\left[\left(\frac{V_0}{V}\right)^{\frac{2}{3}} - 1\right]^3 B_0' + \left[\left(\frac{V_0}{V}\right)^{\frac{2}{3}} - 1\right]^2 \left[6 - 4\left(\frac{V_0}{V}\right)^{\frac{2}{3}}\right]\right\}, \tag{6.2}$$

where E and V are total energy and unit cell volume, respectively. E_0 is the total energy and V_0 is the unit cell volume at the equilibrium phase. B_0 is the bulk modulus and B_0' is the first derivative of the bulk modulus.

Stated another simple way, the total energy in Equ. 6.2 can also be yielded by varying lattice parameter rather than volume, *e.g.* lattice-a corresponding to $E(a)$. Specifically, multiple calculations were performed to produce different total energy (E) by varying the value of lattice-a. For the case of n-MnSb, each calculation requires the in-plane lattice constants fixed and out-of plane lattice constant being allowed to relax (n-MnSb). However, for the case of c-MnSb, lattice constants b and c are fixed to the set value of a in the course of relaxation. This is because their crystal structures remain as hexagonal or cubic throughout.

6.3.2 Results and discussion

Figure 6.2 shows the total energy per unit cell of bulk c-MnSb and n-MnSb as a function of in-plane lattice parameter, a. As observed at the minimum of total energy, the lattice parameter a equal to 6.20 Å is the optimal value for c-MnSb, and the equilibrium lattice constants of n-MnSb are a = 4.13 Å and c = 5.69 Å, respectively. These calculated lattice parameters are in a good agreement with other calculations of a = 6.19 Å [44] and 6.10 Å [45] for c-MnSb, as well as experimentally obtained values, a = 6.502 Å for c-MnSb [32], and a = 4.12 Å, c = 5.77 Å for n-MnSb [40]. In addition, the hexagonal structure, n-MnSb, is formed by lower total free energy compared to cubic ones for all different a-lattice parameter configurations. The energy discrepancy for the formation of different crystalline phases is around 0.849 eV in their equilibrium states. It means the formation of c-MnSb is quite surprising, which requires us to understand the underlying mechanism of c-MnSb formation.

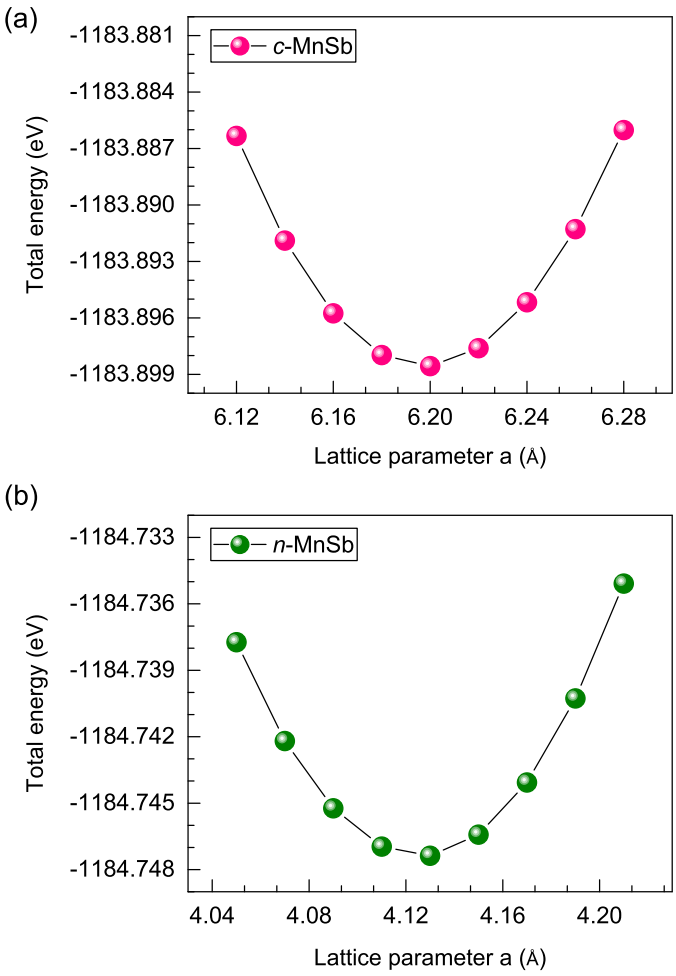

Figure 6.2: Plots of the calculated total energy per unit cell, $E_{\mathrm{Total}}/u.c.$, for (a) *c*-MnSb and (b) *n*-MnSb versus lattice parameter, a.

6.4 Formation of c-MnSb induced by Ga incorporation

As discussed in Sec. 5.3.4., Ga substitution to the subsurface Mn sites in Sb-terminated MnSb(0001) surface has been examined in the four different Ga coverage models. The results show that, in the relaxed model structures, Ga substitution significantly varies the lattice bonding distances and angles of the surrounding Mn and Sb atoms. The newly formed GaSb could act as an effective buffer layer for the formation of a secondary phase, *c*-MnSb, at the Ga-incorporated MnSb surface. To verify this, we further investigate the effect of Ga substitution on the interfacial strength between *n*-MnSb and *c*-MnSb interface. Namely, the negative substitution energies of *c*-MnSb/*n*-MnSb interfaces attained by Ga incorporation conclude that

Ga atoms perform to stabilise *c*-MnSb on *n*-MnSb.

6.4.1 Model structures and computation details

Four different interface models have been considered: Mn- or Sb-terminated (111) surfaces and Mn- or Sb-terminated $(\bar{1}\bar{1}\bar{1})$ surfaces of *c*-MnSb are cleaved to be combined with the most stable Sb-terminated *n*-MnSb(0001) surface. Additionally, Ga substitution of 0.75 ML to the subsurface Mn layers has been confirmed as an optimal Ga configuration at the MnSb surface compared with other coverages (0.25 ML, 0.5 ML as well as 1 ML) and distinct incorporated sites such as Ga interstitials (See Chapter 5). Thus, the Ga coverage of 0.75 ML at the *c*-MnSb/*n*-MnSb interface is employed in this section shown in Fig. 6.3. A vacuum gap of 20 Å is used to avoid any interaction between the topmost surface of *c*-MnSb and the bottommost surface of *n*-MnSb. The four bottom layers of *n*-MnSb are fixed, while the rest of atoms are allowed to fully relax during the calculation. Other calculation conditions are identical with the previous calculations shown in Chapter, 3, 4, and 5. A kinetic energy cut-off of 400 eV, $(2 \times 2 \times 1)$ $\boldsymbol{k}$-points, GGA exchange correlation function, on-the-fly pseudopotential, and spin polarisation are employed.

6.4.2 Substitution energy

The substitution energy of the *c*-MnSb/*n*-MnSb interface with the incorporation of Ga atoms can be described as

$$E_{\mathrm{Sub}} = E_{\mathrm{slab}}^{\mathrm{3Ga}} - E_{\mathrm{pure}} + 3\mu_{\mathrm{Mn}} - 3\mu_{\mathrm{Ga}}, \tag{6.3}$$

where $E_{\mathrm{slab}}^{\mathrm{3Ga}}$ and E_{pure} are the total energies of the interface systems with and without Ga substitution, respectively. They are listed in Table 6.1. μ_{Mn} and μ_{Ga} are the chemical potential of Mn and Ga atoms in the model slabs, which have been quantified by six points in the ternary phase diagram of Mn-Ga-Sb system (see Fig. 5.4). The best environment producing the most stable structure is point-1 in the ternary system with the chemical potentials of Mn, -592.04 eV, and Ga,

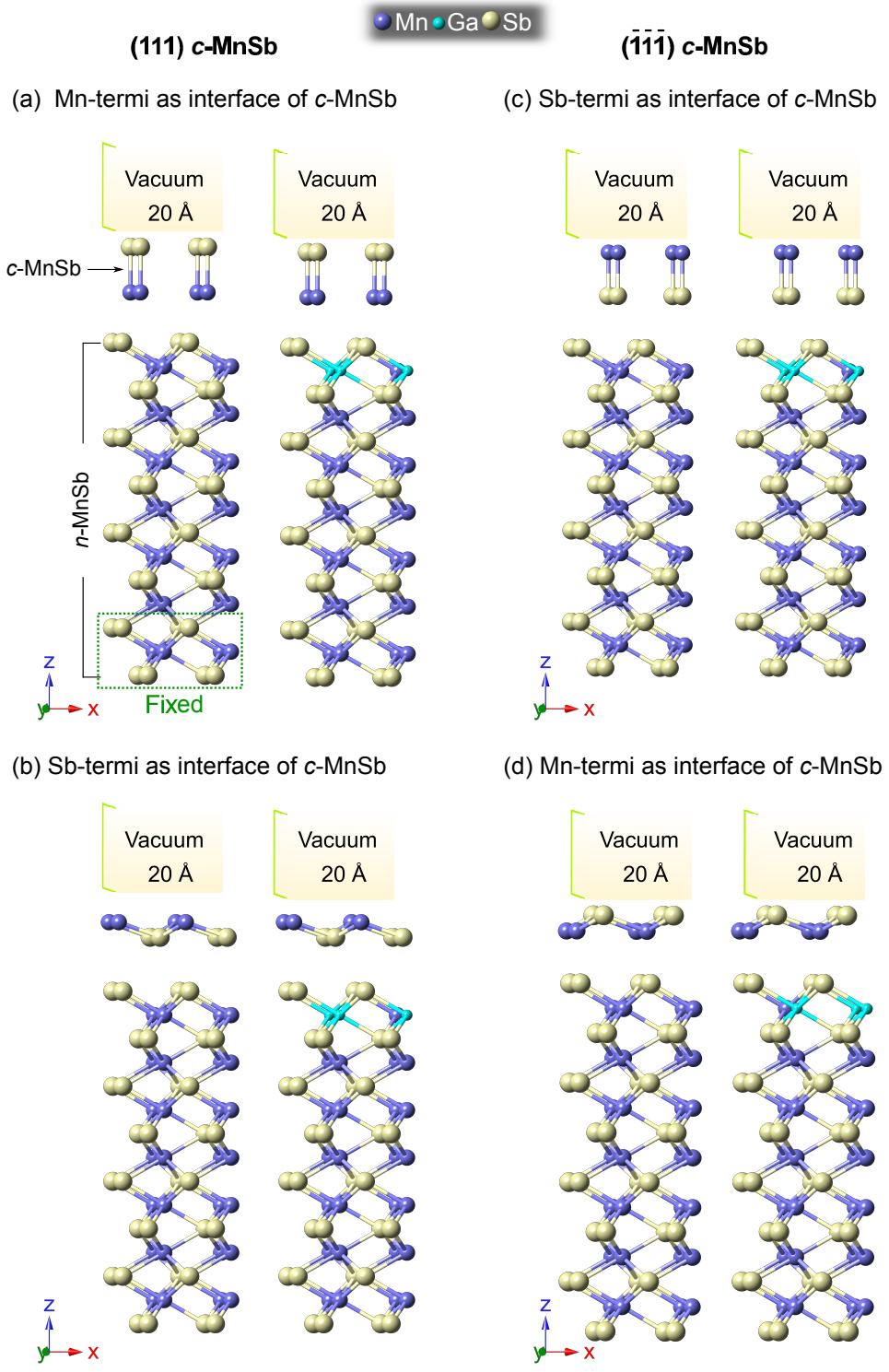

Figure 6.3: The interface slabs between (0001) *n*-MnSb and different terminated *c*-MnSb surfaces along (111) and ($\bar{1}\bar{1}\bar{1}$) planes, respectively. The (111) and ($\bar{1}\bar{1}\bar{1}$) planes face away from the *n*-MnSb. Purple, yellow and green balls stand for Mn, Sb and Ga atoms, respectively.

Table 6.1: Total energy and formation energy of the *c*-MnSb/*n*-MnSb interfaces with and without Ga-substitution.

		E_{pure} (eV)	$E^{3\text{Ga}}_{\text{Pure}}$ (eV)	E_{Form} (eV)
(111)	Mn-termination	-40277.549	-44947.073	0.392
	Sb-termination	-40272.161	-44948.626	-1.922
$(\bar{1}\bar{1}\bar{1})$	Mn-termination	-40273.848	-44945.410	-0.287
	Sb-termination	-40272.171	-44947.957	-1.696

-2148.94 eV. As shown in Table 6.1, the Mn-terminated *c*-MnSb(111) surface combining with n-MnSb is the most stable interface (-40277.49 eV) if there is no Ga influence. However, after Ga substitution to Mn sites at the topmost surface of *n*-MnSb, the Sb-terminated *c*-MnSb(111) surface becomes the strongest combination with *n*-MnSb. Furthermore, its more negative formation energy (-1.922 eV) implies that Ga atoms cohesively enhance the strength of *n*-MnSb/*c*-MnSb interface. This is the indicative of formation and stabilisation of *c*-MnSb on *n*-MnSb induced by Ga incorporation.

6.5 Experimental observation for the growth of n-MnSb thin film on GaAs

Figure 6.4(a) shows the transmission electron microscopy (TEM) image for a MnSb(0001) thin film grown on GaAs(111) substrate [32]. The growth temperature was 400 °C and the growth rate of MnSb film was set at 6 nm/min [32]. The TEM image clearly shows that multiple phases of MnSb are formed during the film growth. Also, the *n*-MnSb epilayer is grown on GaAs(111) with a number of misfit dislocations near the interface. This is because part of strain relaxation occurs within a few nm thickness of the film through the dislocation formation [32, 106]. Combining the MEIS results presented in the Sec. 5.2.1, Fig. 5.1, we conclude that coincidence of the dislocation formation and the Ga out-diffusion relieve the

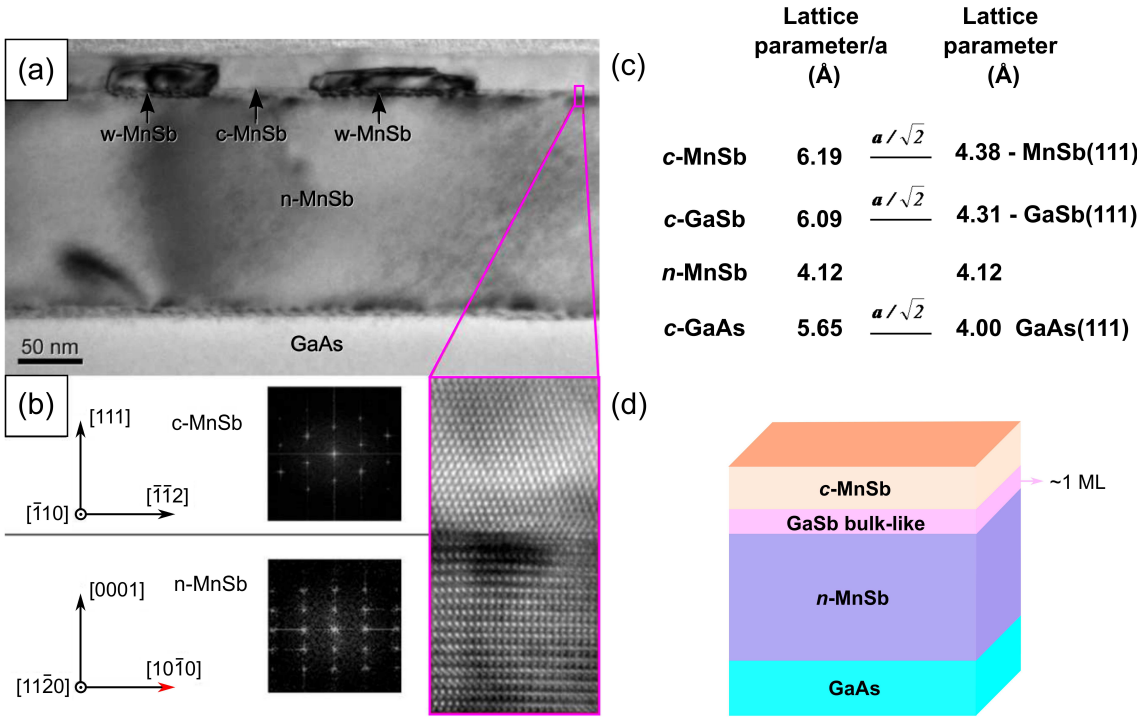

Figure 6.4: (a) TEM cross sectional image of a MnSb($\bar{1}$10)/GaAs(110). A polymorphic MnSb thin film was grown on GaAs(111) substrate [32]. (b) A bright-field image is labelled with constituent phases, while a high resolution micrograph of the *c*-MnSb/*n*-MnSb boundary shows a sharp eptaxial interface [32]. (c) The lattice parameters along x direction and the lattice parameters of the (111) plane for *c*-MnSb, *c*-GaSb and *c*-GaAs. (d) A schematic of the possible structural composition with different phases.

strain energy of the system to be relax. Obviously, the thickness of 100 nm *n*-MnSb implies a complete strain relaxation, which is also responsible for the strain relief. In addition, an abrupt structural transition from *n*-MnSb to *c*-MnSb/*w*-MnSb occurs beyond 100 nm film thickness. These structural changes have also been analysed using selected area diffraction patterns (SADPs) as shown in Fig. 6.4(b). The plane spacing, d, of the lattice planes in SADP was converted to calculate the lattice parameters of different MnSb phases: a = 4.115 Å, c = 5.769 Å for *n*-MnSb; a = 6.502 Å for *c*-MnSb; a = 4.291 Å and c = 7.003 Å for *w*-MnSb consistent with the formation of *c*-MnSb polymorph [32].

On the basis of the experimental observation and theoretical calculation results, the MnSb film on GaAs is modelled as GaAs/*n*-MnSb/*c*-GaSb/*c*-MnSb [Fig. 6.4(d)]. The out-diffusion of Ga atoms could thermodynamically occur during film

growth to form *c*-GaSb. Such atomic diffusion and secondary phase formation in the MnSb/GaAs heterostructure have been expected and calculated in Sec. 5.3.2. Therefore, the formation of the multiphase film on GaAs gives us a direct insight into a crucial role of secondly formed GaSb phase. Namely, thermodynamically stable *c*-GaSb could be functionalised as an effective buffer layer to form metastable ZB (*c*-) MnSb. Moreover, the absolute of the lattice mismatch between *c*-MnSb(111) and *c*-GaSb(111) (around 1.6 %) is much less than the one bewteen *c*-MnSb(111) and *c*-GaAs(111) (around 8.7 %) [The in-plane spacings on the *c*-MnSb(111), *c*-GaSb(111) and *c*-GaAs(111) surfaces being $a^{(111)}_{c-\mathrm{MnSb}}$ =$\mathrm{a}_{c-\mathrm{MnSb}}/\sqrt{2}$ = $6.09/\sqrt{2}$ = 4.31 Å, $a^{(111)}_{c-\mathrm{GaSb}}$ =$\mathrm{a}_{c-\mathrm{GaSb}}/\sqrt{2}$ = $5.94/\sqrt{2}$ = 4.20 Å, and $a^{(111)}_{c-\mathrm{GaAs}}$ =$\mathrm{a}_{c-\mathrm{GaAs}}/\sqrt{2}$ = $5.56/\sqrt{2}$ = 3.93 Å shown in Fig. 6.4(c)]. GaSb(111) surface can therefore facilitate the layer-by-layer film growth. It is additionally believed that the presence of mutual Sb element on the both sides of MnSb/GaSb would increase the probability of growing this heterostructure.

It therefore suggests that the investigation on the diffusion characteristics of Ga atoms would be crucial to address how Ga atoms diffuse out and accumulate at the surface of the grown MnSb film and the following formation of *c*-MnSb. In general, both of line defects (*e.g.* edge dislocations) and planar defects (*e.g.* grain boundaries) are energetically preferential sites for accumulation of point defects and dopants. Furthermore, they are effective pathways for atomic transport. Hence, detailed high resolution transmission electron microscopy (HRTEM) studies on atomic segregation in the local area of MnSb/GaAs could be required as the future experiments.

To get further insights for the effect of GaSb islands on the formation of *c*-MnSb, a strain-free cubic GaSb layer can be employed before MnSb thin film growth. Otherwise, residual strain may affect the formation of stable *n*-MnSb thin films on strained GaSb. In this case, a stable *c*-phase of GaSb will be prerequisite, and selecting appropriate substrates which have almost similar in-plane lattice parameters with GaSb will be crucial for strain-free *c*-GaSb film growth. Finally, different thicknesses of MnSb overlayer on strain-free GaSb/GaAs need to be compared to

evaluate any relaxation (phase transition) in its thin film growth regime.

6.6 Characteristics of GaSb/MnSb interface

Since the above results suggest that *c*-GaSb-bulk like layer is of prime importance for the stabilisation of *c*-MnSb, physical properties of the MnSb/GaSb interface are further demonstrated in simulations. Details on interface energy, geometrical structures, electronic and magnetic informations will be shown.

6.6.1 Computation details and method design

In order to examine the geometrical structure and bonding strength of GaSb, two different interfaces, GaSb(111)/*n*-MnSb(0001) and GaSb(111)/*c*-MnSb(111), are considered [shown in Fig. 6.5(a) and (b)]. The most possible crystal orientations of GaSb(111), *n*-MnSb(0001) and *c*-MnSb(111) are selected as observed in the previous XRD results for the MnSb(0001) thin film grown on GaAs(111) [132]. More specifically, each interface system includes another two interfacial atomic bonding configurations, Ga-Sb and Sb-Mn. This means the Ga-Sb (Sb-Mn) bonds take Ga- (Sb-) termination from GaSb to interact with Sb (Mn) atoms of MnSb. For the GaSb/*n*-MnSb, these two interfaces are referred to as *n*-Ga-Sb [shown in Fig. 6.5(a)I] and *n*-Sb-Mn [shown in Fig. 6.5(a)II]. While for the GaSb/*c*-MnSb, two different interfacial bondings are labelled as *c*-Ga-Sb [shown in Fig. 6.5(b)I] and *c*-Sb-Mn [shown in Fig. 6.5(b)II]. All of the interface model structures are attempted to satisfy the layer-stacking-order of bulk constituent materials. For example, the atomic sequence at the interface in Fig. 6.5(a) follows a hexagonal AcAb order of *n*-MnSb, A'c'A'b'Ac [Fig. 6.5(b)I] and c'A'b'A'c [Fig. 6.5(b)II], (denoted by red letters) or a cubic AaBbCc order of *c*-GaSb. A' (c') and A (c) represent for the similar symmetrical position in *n*-MnSb and GaSb, respectively. Since the models of GaSb/*c*-MnSb undergo significant atomic relaxation during the geometry optimisation, the reference structures before relaxation are also given in Fig. 6.5(b).

All of the supercell slabs consist of 13 atomic monolayers for GaSb and MnSb, respectively. All the layers were continuously relaxed to the residual forces below

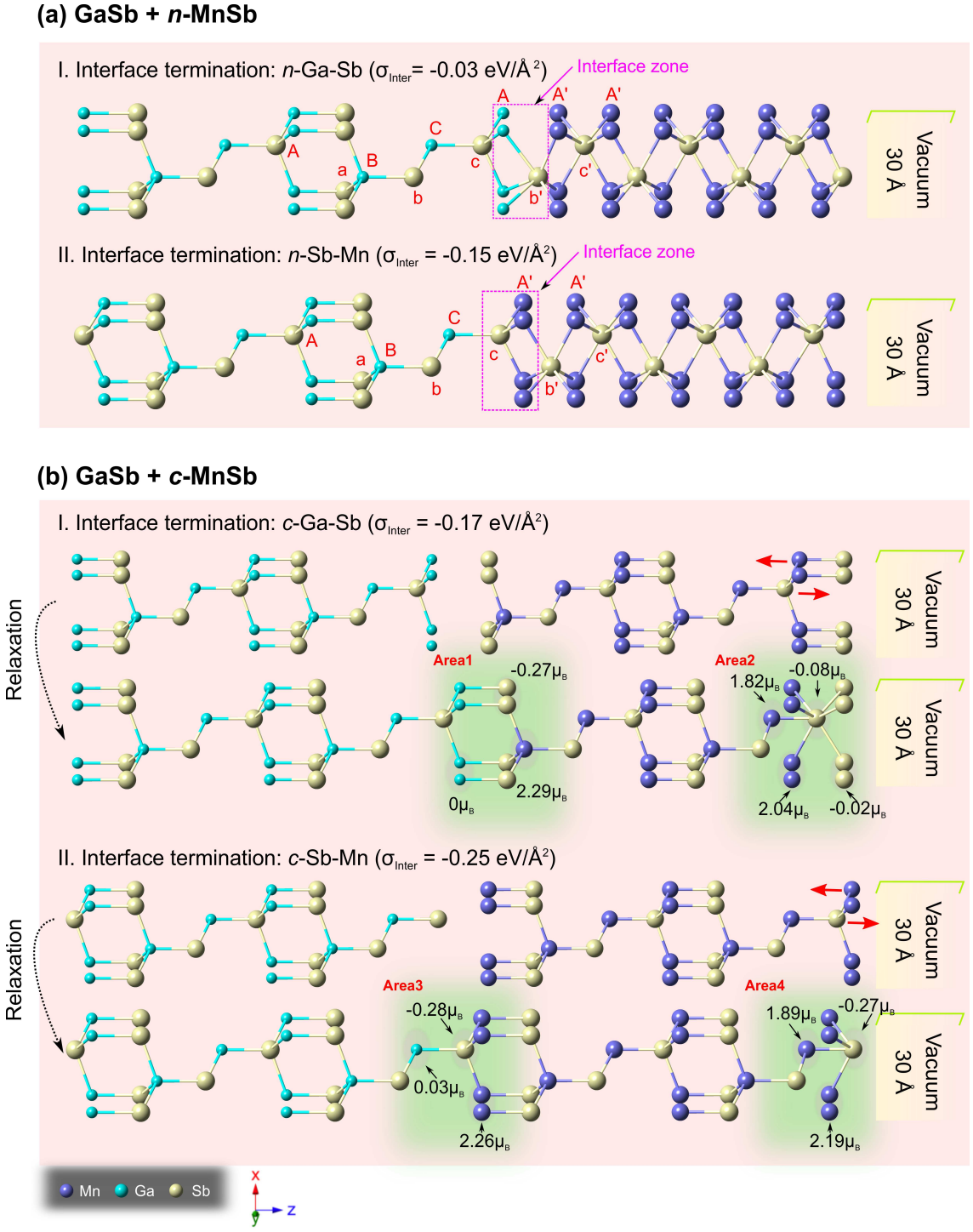

Figure 6.5: Structural models for (a) GaSb(111)/*n*-MnSb(0001) and (b) GaSb(111)/*c*-MnSb(111), each of which includes two types of termination interface: Ga-Sb and Sb-Mn. In the case of GaSb/*c*-MnSb system, the geometrical structures before relaxation were also inllustrated as references to be compared. The local magnetic moment for a collection of individual atoms in some special regions are labelled by Area-1, Area-2, Area-3, and Area-4. Purple, green, and yellow balls are Mn, Ga, and Sb atoms, respectively.

0.03 eV/Å. Vacuum of 30 Å was selected. All calculations were carried out using a kinetic energy cut-off of 400 eV, $(7 \times 7 \times 1)$ $\boldsymbol{k}$-points, GGA exchange correlation function, on-the-fly pseudopotentials, electron spin polarisation.

6.6.2 Interface energy

The interface energies of the four different GaSb/MnSb heterointerfaces mentioned above are calculated to determine the interface stability. The interface energy per area, σ_{Inter}, can be defined as:

$$\sigma_{\text{Inter}} = \frac{1}{A}\left(E_{\text{GaSb/MnSb}} - E_{\text{GaSb}} - E_{\text{MnSb}}\right). \tag{6.4}$$

Here, A is the area of the interface slab. $E_{\text{GaSb/MnSb}}$ is the total energy of the GaSb/MnSb interface slab; E_{GaSb} and E_{MnSb} are the total energy of the isolated GaSb and MnSb surface slab with a vacuum gap of 30 Å. The calculated total energies and interface energies are listed in Table 6.2.

The results show that the bonding strength of the *c*-MnSb/GaSb is stonger than *n*-MnSb/GaSb as expected, and the reason has already been explained in Sec. 6.5. In addition, the atomic bondings of Sb-Mn are always more stable than that of Ga-Sb regardless of type of crystal structure. The interface energy calculation suggests that the Sb-Mn termination in the composition of GaSb(111)/*c*-MnSb(111) system is most likely to be the ideal interface as discussed above with the lowest interface enegy of -0.25 eV/Å^2. Therefore, the following discussions of magnetic properties and DOS will be only focused on the system of GaSb/*c*-MnSb.

6.6.3 Magnetic properties and density of states

6.6.3.1 Magnetic moment

In this section, the magnetic properties of *c*-Ga-Sb and *c*-Sb-Mn interfaces are investigated by resolving four different interatomic bonds denoted by Area1-4 in Fig. 6.5. The results exhibit that the magnetic moment of the interface slabs [Area-1 and Area-3 in Fig. 6.5(b)] is very sensitive with the surface termination. As

Table 6.2: Total energies and interface energies for various GaSb/MnSb interface, and the total energies of the isolated GaSb and MnSb surface slabs.

Species	Total energy (eV)			σ_{Inter}
	$E_{\text{GaSb/MnSb}}$	E_{GaSb}	E_{MnSb}	(eV/Å^2)
n-Ga-Sb [Fig. 6.5(a)I]	-26300.230	-18599.382	-7700.369	-0.03
n-Sb-Mn [Fig. 6.5(a)II]	-24742.817	-17043.261	-7697.149	-0.15
c-Ga-Sb [Fig. 6.5(b)I]	-26296.509	-18599.382	-7694.339	-0.17
c-Sb-Mn [Fig. 6.5(b)II]	-24739.402	-17043.261	-7691.961	-0.25

evidenced by Area-1, there is no significant spin exchange splitting of interface-Ga atom because the neighboring Sb atom has a relatively weak magnetic moment, -0.27μ_B. By contrast, two normally nonmagnetic Ga and Sb layers have been induced to produce the magnetic moments of -0.03μ_B and -0.28μ_B shown in Area-3. This is indicative of that Sb(p)-Mn(d) hybridisation enhances the spin exchange splitting compared to that for Ga(s)-Sb(p) interaction.

Other interesting phenomena are also observed in Area-2 and Area-4. The energetically unstable surfaces of *c*-MnSb undergoes dramatic atomic relaxation along z-axis. As can be seen from the Sb-terminated surface, the Mn atom in the subsurface layer relaxes outward to the topmost surface. However, the Sb atom in the third layer moves in an opposite direction being inclined to situate at the vertex of the altered octahedron. This position swap of Mn and Sb atoms eventually gives to a new pattern in which the moved-Sb atom is coordinated with six neigbouring atoms. The surface atomic arrangement is more likely to attempt to create a hexagonal environment and form the *n*-MnSb phase. The closed values of magnetic moments between this surface configuration (1.82μ_B and 2.04μ_B for two different Mn layers in Area-2, respectively) and *n*-MnSb bulk (1.95μ_B per Mn atom) provides another

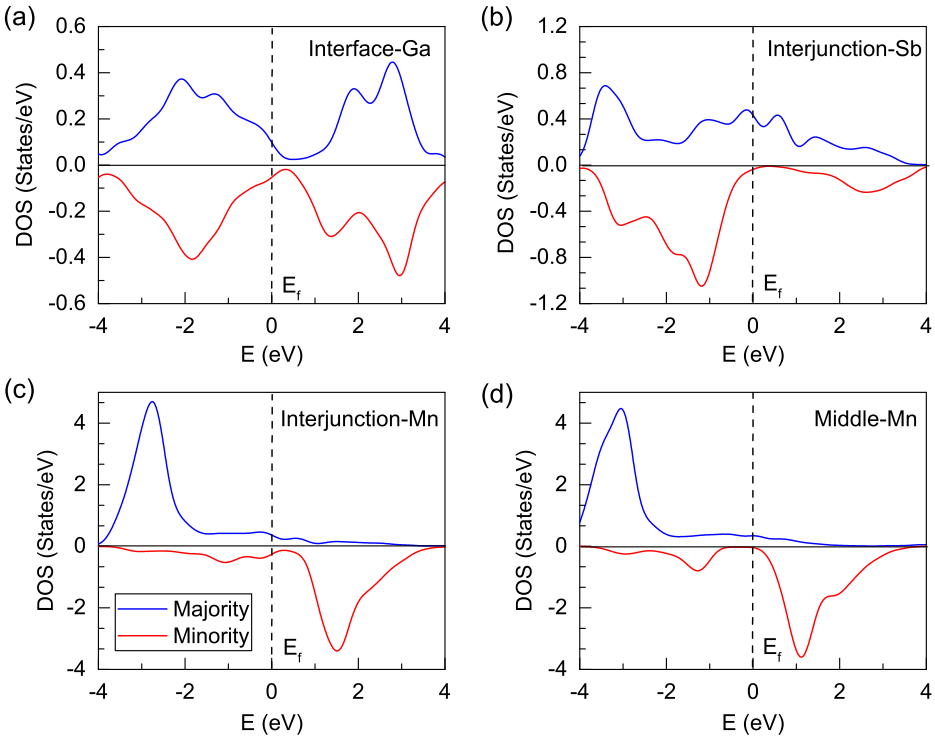

Figure 6.6: The spin polarised PDOS (States/eV) for the three layers of Ga, Sb and Mn in the frame of Area-3, as well as a Mn layer between Area-3 and Area-4. Blue and red lines are the majority (spin-up) and minority (spin-down) orbitals, respectively.

evidence of *n*-MnSb formation. By contrast, the magnetic moment of *c*-MnSb is $2.32\mu_B$ per Mn atom, which is far from the derived Mn atom magnetic moment at the surface. The relaxation of Mn-termination surface has the simliar tendence with Sb-termination as shown in Area-4. Consequently, the above comparison in the relaxation and revaluated magnetic moments of the different interfaces shows that the *c*-MnSb phase is effectively formed by connecting *c*-GaSb. However, all of the MnSb surfaces exposed to vacuum tend to form *n*-MnSb.

6.6.3.2 Density of states

In order to investigate the HM properties of the most stable *c*-Sb-Mn slab, the atomic partial density of states (PDOS) for the Ga, Sb and Mn layers in Area-3 in Fig. 6.5(b)II and a Mn layer between Area-3 and Area-4 are calculated. It is found that the SP is greatly influenced by the interface itself along with an adjacent layer. More particularly, the Sb atom becomes partially half-metallic [Fig. 6.6(b)],

while the Ga atom is just magnetic [Fig. 6.6(a)]. The Mn atom at the interface loses out a half-metallicity [Fig. 6.6(c)], however, 100 % SP has been fully recovered from the middle Mn atomic layer [Fig. 6.6(d)].

6.7 Conclusion

The electronic band structure and DOS of bulk *c*-MnSb have been confirmed using DFT calculations. The results show that the *c*-MnSb has purely HM properties with a spin magnetic moment of $4\mu_B$ and an energy band gap of 1.52 eV in the minority DOS orbitals. However, the *c*-MnSb is metastable by the comparison of the total energy of n-MnSb. Under this situation, Ga atoms embedded at *n*-MnSb/*c*-MnSb interfaces are modelled. The obtained negative substitution energies of the interfaces imply that Ga atom at *n*-MnSb/*c*-MnSb interface can lead to an increase in the interfacial strength, thereby stabilising *c*-MnSb on *n*-MnSb. Based on experimental results and a list of theory calculations presented in this chapter, multiple phases in a MnSb thin film grown on GaAs substrate are estimated as GaAs/*n*-MnSb/GaSb/*c*-MnSb.

Several further interface calculations of GaSb/n-MnSb and GaSb/*c*-MnSb have been performed. It is found that the interatomic bonding of Sb(from GaSb)-Mn(from *c*-MnSb) provides the most stable configuration with the most negative interface energy, -0.25 eV/Å^2. The PDOS results show that the HM properties of *c*-MnSb are maintained from the interface layers to middle layers of the *c*-MnSb. Furthermore, the relaxed *c*-MnSb surfaces tend to form *n*-MnSb phase. All of the results presented here suggest that GaSb can be an effective buffer layer for the formation/stabilisation of *c*-MnSb.

Chapter 7

Conclusions and future work

7.1 Summary

In this thesis, we have primarily explored the structural, electronic and magnetic properties of MnSb(0001) surfaces on a GaAs substrate. The first result chapter was concerned with the clean (1 × 1) *n*-MnSb surface. From the Gibbs free energy calculations, we concluded that the Sb-terminated surface is more energetically favourable than both the Mn-terminated and Sb-monolayer-coated surfaces. Subsequently, the stability and magnetic moment of the MnSb(0001) surface have been systematically investigated by comparing with other As- and Sb-based TMP compounds, *i.e.* MnAs, CrAs, CrSb, NiAs, and NiSb. The results show that the more stable structures normally have a lower magnetic moment. The Chapter 3 also determines the reason of island formation when MnSb grows onto GaAs(111) substrate in terms of the calculation of the surface energy of *n*-MnSb(0001), $(1\bar{1}00)$, and GaAs(111) surfaces.

In Chapter 4, quantitative structures of (2 × 2) reconstructed MnSb(0001) surfaces have been demonstrated using a combination of DFT and LEED I-V methods. Our results clearly show that single Sb adsorption at HCP sites is the most stable case for Sb-terminated surfaces of MnSb formed Sb-on-Sb (2 × 2) reconstructions. This stability is shown through having both the lowest Gibbs free energy in DFT and the best R-factor in LEED calculations. For the most favourable Sb-adatom surface, the bond characteristics and DOS results show the shortest bond length and lowest DOS value at the Fermi level. In addition, the MnSb surface tends to reconstruct in a similar way to semiconductor surface reconstruction on the basis of charge density difference calculations.

The segregation of Ga atoms from the GaAs substrate to the MnSb surface has been comprehensively investigated in Chapter 5. This phenomenon has been

observed by XPS and MEIS experimently, and DFT further confirmed the Ga atom segregation by considering the segregation energy. The surface energy change also provides the quantity of Ga segregation which is 0.75 ML. In addition, both MEIS and DFT suggest that Ga atoms have a stronger tendency to substitute Mn atoms in the subsurface layer rather than to occupy the interstitial sites. What is significant to note is that segregated Ga atoms can be treated as a seed to grow c-MnSb through the analysis of the relaxed atomic structures of Ga-substituted MnSb(0001) surfaces. Together with the optimal experimental growth conditions of the formation of c-MnSb, *e.g.* T_{sub} is larger than 675 K, and the flux ratio, J, is in the range of 6.6 to 7.5, we can make an initial speculation of the formation mechanisums of c-MnSb.

Chapter 6 discussed the formation mechanisum of c-MnSb in more detail. The band structure and DOS results show that c-MnSb has a purely HM property with a spin magnetic moment of $4\mu_B$, but the energy calculations indicate c-MnSb is metastable. Therefore, stabilising c-MnSb is considered to be a crucial issue. Here, the negative formation energy of interfaces acquired by designing the models of Ga atoms embeded at n-MnSb/c-MnSb, indicates that Ga atoms can increase the interfacial strength and thus stabilise c-MnSb on n-MnSb. This is because segregated Ga atoms form GaSb, which has the stable cubic phase and lower lattice mismatch with c-MnSb ($\approx$2.5 %) to promote c-MnSb growth. Hence, some interface calculations based on GaSb/n-MnSb and GaSb/c-MnSb were investigated. The results demonstrate that the interatomic bonding of Sb (from GaSb) - Mn (from c-MnSb) has the most stable configuration with the lowest interface energy, -0.25 eV/Å. We also found that the HM property can be sustained from interface layers to middle layers of the c-MnSb, however, the surface region are inclined to form n-MnSb. All of the results indicate that Ga atoms, more precisely GaSb, is a very important factor when forming c-MnSb.

7.2 Future work

There are still a lot of unknowns related to the hexagonal TMP surface structure and the formation of cubic MnSb.

The study of the surface reconstruction for III-V semiconductors are well-known on the basis of following the electron counting rules [144–146]. Namely, the anion dangling bonds are filled and the cation dangling bonds are empty. However, for the case of TMP, the rules of surface reconstruction are still not clear. Our calculations made some contribution to the (2×2) reconstructed surface of MnSb(0001), but it is still necessary to observe other TMPs to determine their reconstruct ion rules.

It has been shown in Chapter 5 that Ga segregation is directly linked to the annealing temperature. Based on previous studies, the annealing temperature of 420 °C can lead to Ga diffusion from GaAs, however, As diffusion requires the annealing temperature above 600 °C. Therefore, the further effects of different annealing temperature from 400 - 600 °C may help increase the amount of Ga segregation and thus create more *c*-MnSb. This will provide some useful insights in determining the mechanism of formation for *c*-MnSb. GaSb has been suggested to be the promising candidate to form and stabilise *c*-MnSb from theoretical predictions shown in Chapter 6. It is worthwhile growing MnSb on GaSb in experiment to check the growth mechanisum. To investigate this, several questions will have to be considered:

- Can MnSb be grown on GaSb sucessfully? If so, what is the interface between epitaxial thin film and the substrate smooth.

- What are the optimal growth conditions for GaSb/MnSb? (T_{sub} and flux ratio, J)

- Does *c*-MnSb form at the interface and is *n*-MnSb stabilised at the surface as presented in theory? If so, what is the thickness of *c*-MnSb and *n*-MnSb in the thin film, respectively?

Appendix A

Proposed (2 × 2) surface reconstruction models

A.1 Introduction

This appendix outlines all of trial models of MnSb(0001) (2 × 2) surfaces [Fig. A.1 (identical atom adsorptions) Fig. A.1 (mixed terminations)], and the relavant data including the number of different atoms in the slabs as well as the total energy summarized in Table A.1 and Table A.2, respectively. The purpose of presenting this work is to filter some unfavourable models through the total energy comparision. The other models with different atom numbers which requires calculation of the Gibbs free energy are selected and compared in Chapter 4.

A.2 Identical atom adsorptions

Fig. A.1(a) shows the adatom (one Mn or one Sb atom) configurations with three possible (HCP, FCC, and TOP) sites. Firstly considering the Sb-adatom case, each model has the same number of constituent atoms (28 for Mn and 29 for Sb atoms shown in Table A.1). Therefore, the optimal place can be determined by comparing the total energies directly, neglecting chemical potentials. The favourable location for Sb-adatom will be the HCP site with the lowest total energy of -33757.502 eV [FCC (-33756.854 eV) and TOP (-33755.805 eV)]. As such, Mn adatom perfers the FCC site in the Mn-adatom group. The corresponding total energy is -33756.073 eV. As a result, the "1Sb-HCP" and "1Mn-FCC" models have been chosen to be analysed in Chapter 4.

For two-atom adsorption shown in Fig. A.1(b), three series of structures are designed: dimer, HCP, and FCC. The dimer configurations have been shown both unrelaxed and relaxed structures due to the large movement after the relaxation.

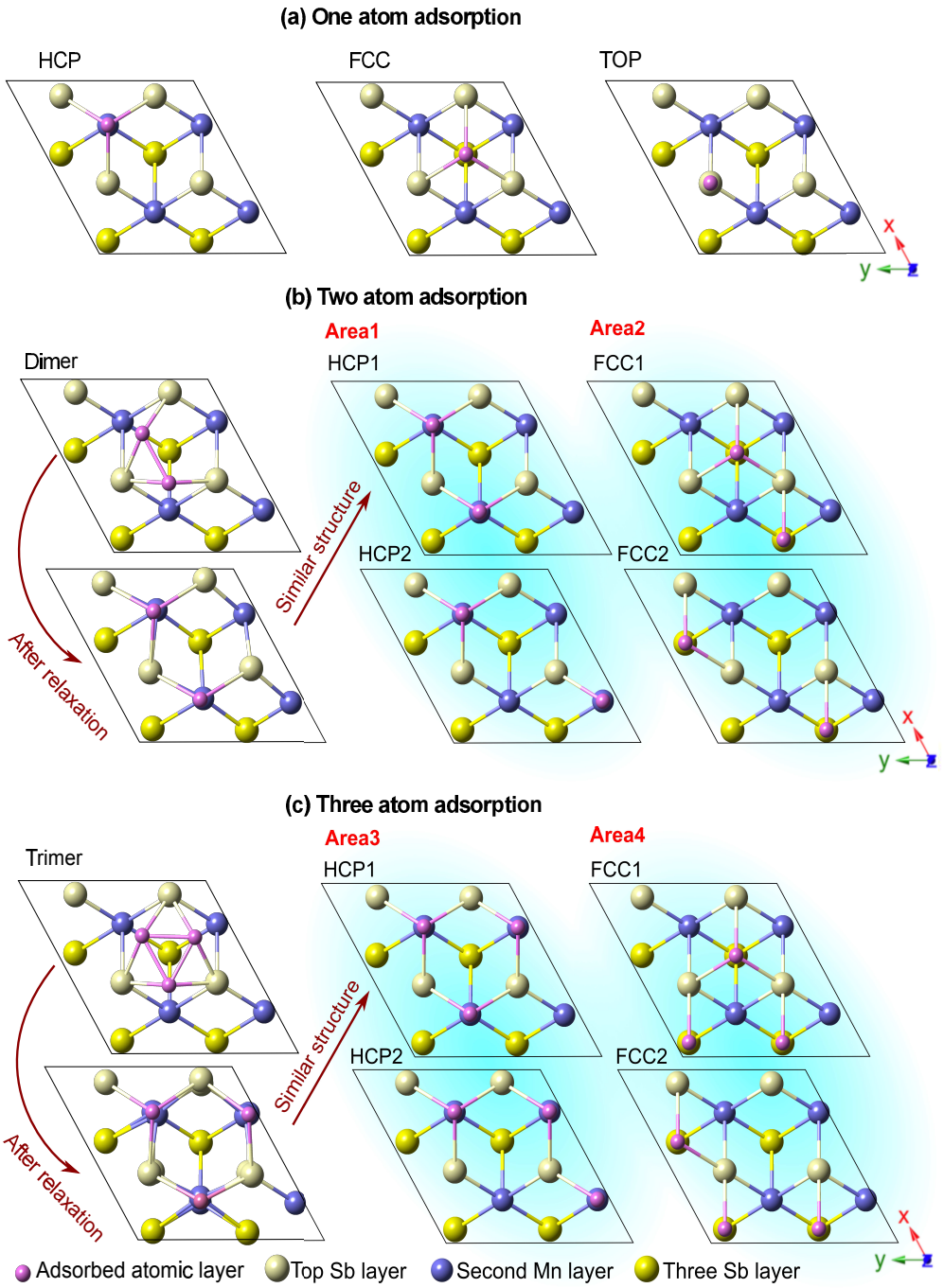

Figure A.1: Structures for (2 × 2) reconstructions of the trial (0001) MnSb models: (a) one, (b) two, and (c) three atom adsorption. Light and dark yellow balls indicate the top and third Sb layer, respectively. Purple balls stand for the second Mn layer. Pink balls are adsorbed atoms, which can either be Sb or Mn atoms.

Table A.1: The number of Mn and Sb atoms as well as the total energy of considered slabs in Fig. A.1

	Adsorption atoms	Adsorption sites	N_{Mn}	N_{Sb}	Total energy (eV)
One atom adsorption	Sb	HCP	28	29	-33757.502
		FCC	28	29	-33756.854
		TOP	28	29	-33755.805
	Mn	HCP	29	28	-33755.577
		FCC	29	28	-33756.073
		TOP	29	28	-33756.063
Two atom adsorptions	Sb	Dimer	28	30	-34350.119
		HCP1	28	30	-34350.117
		HCP2	28	30	-34350.104
		FCC1	28	30	-34349.211
		FCC2	28	30	-34349.091
	Mn	Dimer	30	28	
		HCP1	30	28	-34346.404
		HCP2	30	28	-34346.414
		FCC1	30	28	-34347.300
		FCC2	30	28	-34347.270
Three atom adsorptions	Sb	Trimer	28	31	-34942.252
		HCP1	28	31	-34942.252
		HCP2	28	31	-34942.252
		FCC1	28	31	-34941.628
		FCC2	28	31	-34941.265
	Mn	Trimer	31	28	-34937.033
		HCP1	31	28	-34937.034
		HCP2	31	28	-34937.034
		FCC1	31	28	-34938.459
		FCC2	31	28	-34938.458

Obviously, the initial pair of dimer atoms tends to be broken and eventually relax toward to the HCP sites. The Dimer and HCP (HCP1 here) achieving the analogous final structure can be also supported by their similar total energy. The total energy of Sb-dimer and HCP1 are -34350.119 and -34350.117 eV shown in Table A.1, respectively. For the case of Mn adsorption, dimer and HCP1 have the total energy of -34346.404 and -34346.404 eV. We can, therefore, get rid of the dimer adsorptions case by only considering HCP condition. The other two groups of HCP and FCC sites are established on HCP1(FCC1) and HCP2(FCC2) according to the distance of two adsorbed atoms shown in Fig. A.1(b). In comparision to their total energy, we can find that there is no noticable change between HCP1 and HCP2, also between FCC1 and FCC2. Additionally, HCP sites have the lowest total energy of Sb-modified surfaces (-34350.117 eV), whereas the lowest total energy is FCC for Mn-adsorbed surfaces (-34347.300 eV). Hence, the "2Sb-HCP" and "2Mn-FCC" are the relatively favourable models and selected to be further studied in Chapter 4.

Following the same steps, "3Sb-HCP" and "3Mn-FCC" are made choices for deeper analysis. These six models ("1Sb-HCP", "1Mn-FCC", "2Sb-HCP", "2Mn-FCC", "2Sb-HCP", and "3Mn-FCC") are highlighted by yellow shade in Table A.1.

A.3 Mixed termination

Six mixed-atom constructions are built up on the basis of the proportion of Mn and Sb atoms at the top surface. Due the different number of Mn and Sb in those slabs, the Gibbs free energy ($G = E^{\text{Slab}}_{\text{total}} - \mu_{\text{Mn}} N_{\text{Mn}} - \mu_{\text{Sb}} N_{\text{Sb}}$) has to be applied to determine their stability. The detailed calculation processes of Gibbs free energy are presented in Sec. 3.1.2, and the Gibbs free energies of mixed termination slabs are all around 10 eV under the both of Mn and Sb rich conditions (Table A.2). Those values are much higher the ones of selected models shown in Table 4.1, so this mixed cases are not considered either.

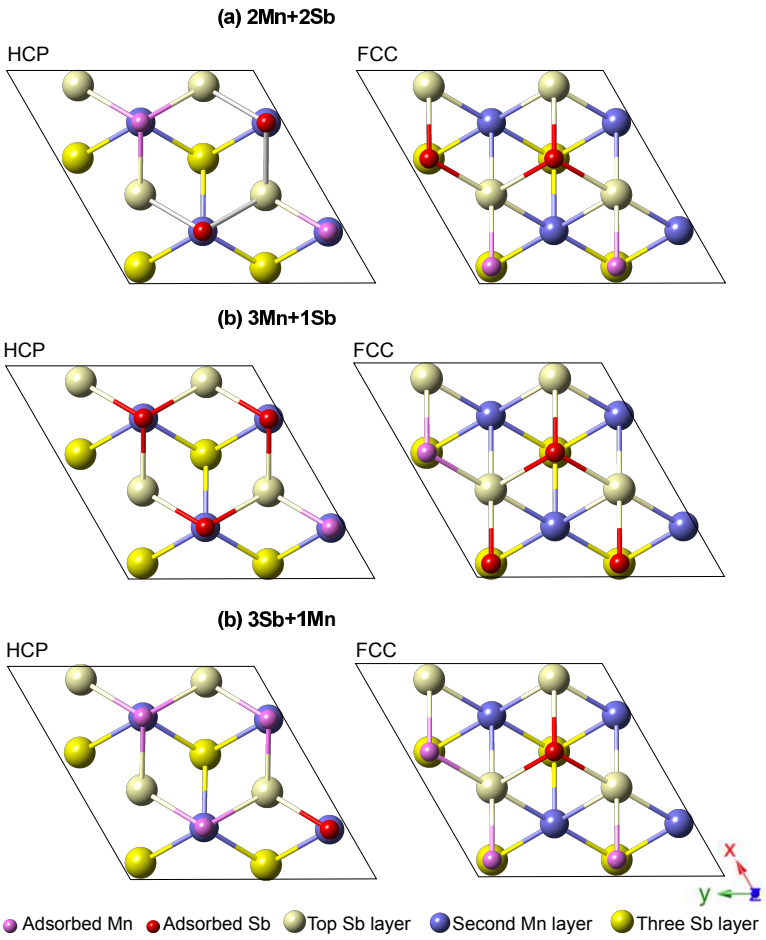

Figure A.2: Mixed adsorbed structures for (2 × 2) reconstructions of the (0001) MnSb models: (a) 2Mn + 2Sb, (b) 3Mn + 1Sb, and (c) 3Sb + 1Mn. Light and dark yellow balls indicate the top and third Sb layer. Purple balls stand for the second Mn layer. Pink and red balls are adsorbed Mn and Sb atoms

Table A.2: The number of Mn and Sb atoms as well as the total energy of considered slabs in Fig. A.2.

Species	Adsorption sites	N_{Mn}	N_{Sb}	Total energy (eV)	G (eV)	
					Mn-rich	Sb-rich
2Mn + 2Sb	HCP	30	30	-35532.231	10.383	10.383
	FCC	30	30	-35532.030	10.584	10.584
3Mn + 1Sb	HCP	31	29	-35531.432	9.876	10.496
	FCC	31	29	-35531.466	9.842	10.461
1Mn + 3Sb	HCP	29	31	-35533.144	10.766	10.156
	FCC	29	31	-35533.213	10.708	10.088

Appendix B

CLEED input files

An instance of CLEED input files employed in our calculations are provided here. The *.bul* and *.ctr* files are identical for all of configuration, and only *.inp* put files are required to be changed according to the relaxed CASTEP results.

B.1 MnSb2×2.bulk

```
c: MnSb(0001) bulk -- Sb terminated (Sb adatom)
#
a1:       3.5680    2.0600    0.0000
a2:      -3.5680    2.0600    0.0000
a3:       0.0000    0.0000   -5.7840
#
m1:  2.   0.
m2:  0.   2.
#
#sr:  3    0.0    0.0
#
vr:     -6.00
vi:      4.5
#0
#Vibs: T_D=220, dr1: Mn=0.1281, Sb=0.0861
#Vibs: T_D=300, dr1: Mn=0.0705, Sb=0.0474
#Vibs: T_D=200, dr1: Mn=0.1410, Sb=0.0947
#
# bulk:
pb: Sb_MnSb  0.0000     0.0000     0.0000     dr1   0.03
```

pb: Mn_MnSb 1.1893 2.0610 -1.4460 dr1 0.04

pb: Sb_MnSb -1.1893 2.0610 -2.8920 dr1 0.03

pb: Mn_MnSb 1.1893 2.0610 -4.3380 dr1 0.04

#

ei: 34.0

ef: 230.1

es: 4.

it: 0.0

ip: 0.

ep: 1.e-2

lm: 7

B.2 MnSb2×2.ctr

MnSb 2×2

(control file for R factor programme CRFAC)

ef=⟨experimental input file⟩

#ti = ⟨indices in theoretical input file⟩

#id = ⟨group ID⟩

:= separator

ef = Spot_1.dat : ti = $(0.00, 1.00) + (-1.00, 0.00) + (1.00, -1.00) + (0.00, -1.00) + (1.00, 0.00) + (-1.00, 1.00)$: id = 01 : wt = 1.

ef = Spot_2.dat : ti = $(1.00, 1.00) + (2.00, -1.00) + (1.00, -2.00) + (-1.00, -1.00) + (-2.00, 1.00) + (-1.00, 2.00)$: id = 02 : wt = 1.

#

ef = Spot_3.dat : ti = $(0.00, 0.50) + (-0.50, 0.00) + (0.50, -0.50) + (0.00, -0.50) + (0.50, 0.00) + (-0.50, 0.50)$: id = 03 : wt = 1.

ef = Spot_4.dat : ti = $(0.50, 0.50) + (-0.50, -0.50) + (1.00, -0.50) + (-1.00, 0.50) + (-0.50, 1.00) + (0.50, -1.00)$: id = 04 : wt = 1.

ef = Spot_5.dat : ti = $(0.00, 1.50) + (-1.50, 0.00) + (1.50, -1.50) + (0.00, -1.50) +$

$(1.50, 0.00)\ + (-1.50, 1.50) : \mathrm{id} = 05 : \mathrm{wt} = 1.$

.

B.3 MnSb2×2.inp

```
c: MnSb(0001) Sb terminated: adding Sb atom A layer
#
#
a1:       3.5680    2.0600    0.0000
a2:      -3.5680    2.0600    0.0000
#
m1:  2.   0.
m2:  0.   2.
#
#Vibs: T_D=220, dr1: Mn=0.1281, Sb=0.0861
#Vibs: T_D=300, dr1: Mn=0.0705, Sb=0.0474
#Vibs: T_D=200, dr1: Mn=0.1410, Sb=0.0947
#
# RECONSTRUCTED LAYER

# LAYER D (Sb)
po: Sb_MnSb    1.256102    2.069152    7.160193    dr1 0.100000
# LAYER C (Sb)
po: Sb_MnSb    0.233158   -0.221761    5.920166    dr1 0.090000
po: Sb_MnSb    0.115718   -4.422311    5.761497    dr1 0.090000
po: Sb_MnSb   -3.504662    1.548767    5.040507    dr1 0.090000
po: Sb_MnSb   -3.416434   -2.345862    6.093196    dr1 0.090000
# LAYER A (Mn)
po: Mn_MnSb    1.428174    1.801951    4.205336    dr1 0.060000
po: Mn_MnSb    1.163321   -2.002314    4.153360    dr1 0.060000
```

```
po: Mn_MnSb  -2.707060   3.459808   4.106447   dr1 0.060000
po: Mn_MnSb  -2.128805  -0.344043   4.306751   dr1 0.060000
# LAYER B (Sb)
po: Sb_MnSb  -0.955559   1.876954   2.958236   dr1 0.030000
po: Sb_MnSb  -1.096776  -2.353909   2.697818   dr1 0.030000
po: Sb_MnSb  -4.526914   4.229655   2.596126   dr1 0.030000
po: Sb_MnSb  -5.212148  -0.322360   2.936414   dr1 0.030000
# LAYER A (Mn)
po: Mn_MnSb   1.227762   1.941789   1.345653   dr1 0.040000
po: Mn_MnSb   1.220139  -2.730787   1.350228   dr1 0.040000
po: Mn_MnSb  -2.636359   3.443996   1.540532   dr1 0.040000
po: Mn_MnSb  -2.125988   0.263104   1.465071   dr1 0.040000
#
#
rm: Sb_MnSb  1.00
rm: Mn_MnSb  1.00
#
#sr:  3  0.0  0.0
#
zr: 1.01  7.80
#
sz: 0
sa: 0
```

Bibliography

[1] G. A. Prinz, Science **250**, 1092 (1990).

[2] S. A. Wolf, D. D. Awschalom, R. A. Buhrman, J. M. Daughton, S. von Molnár, M. L. Roukes, A. Y. Chtchelkanova, and D. M. Treger, Science **294**, 1987 (2001).

[3] L. Bogani, and W. Wernsdorfer, Nature Mater. **7**, 179 (2008).

[4] D. Supriyo, and D. Biswajit, Appl. Phys. Lett. **56**, 665 (1990).

[5] I. Tudosa, J. A. Katine, S. Mangin, and E. E. Fullerton, Appl. Phys. Lett. **96**, 212504 (2010).

[6] P. N. Hai, S. Ohya, M. Tanaka, S. E. Barnes, and S. Maekawa, Nature Lett. **458**, 489 (2009).

[7] D. A. Thompson, l. T. Romankiw, and A. F. Mayadas, IEEE Trans. Magn. **11**, 1039 (1975).

[8] G. Koster, and G. Rijnders, *In Situ Characterization of Thin Film Growth*, Woodhead Publishing Limited, 2011.

[9] D. Ielmini, and R. Waser, *Resistive Switching: From Fundamentals of Nanoionic Redox Processes to Memristive Device Applications*, John Wiley & Sons, 2015.

[10] O. Rader, A. Kimura, N. Kamakura, K. S. An, A. Kakizaki, S. Miyanishi, H. Akinaga, M. Shirai, K. Shimada, and A. Fujimori, Phys. Rev. B **57**, R689 (1998).

[11] W. Wu, J. G. Cheng, K. Matsubayashi, P. Kong, F. Lin, C. Q. Jin, N. L. Wang, Y. Uwatoko, and J. L. Luo, Nat. Commun. **5**, 5508 (2014).

[12] R. Coehoorn, C. Haas, and R. A. de Groot, Phys. Rev. B **31**, 1980 (1985).

[13] H. Kronmüller, J. B. Yang, and D. Goll, J. Phys.: Condens Matter **26**, 064210 (2014).

[14] F. Schippan, G. Behme, L. Däweritz, K. H. Ploog, B. Dennis, K. -U. Neumann, and K. R. A. Ziebeck, J. Appl. Phys. **88**, 2766 (2000).

[15] J. D. Aldous, C. W. Burrows, I. Maskery, M. S. Brewer, T. P. A. Hase, J. A. Duffy, M. R. Lees, C. Sánchez-Hanke, T. Decoster, W. Theis, A. Quesada, A. K. Schmid, and G. R. Bell, J. Phys.: Condens. Matter **24**, 146002 (2012).

[16] A. M. Nazmul, H. Shimizu, and M. Tanaka, J. Appl. Phys. **87**, 6791 (2000).

[17] K. Ono, M. Shuzo, M. Oshima, and N. Akinaga, Phys. Rev. B **64**, 085328 (2001).

[18] H. Akinaga, S. Miyanishi, W. Van Roy, and L. H. Kuo, Appl. Phys. Lett. **70**, 2472 (1997).

[19] V. Garcia, H. Jaffrès, M. Eddrief, M. Marangolo, V. H. Etgens, and J. M. George, Phys. Rev. B **72**, 081303 (2005).

[20] A. Ouerghi, M. Marangolo, M. Eddrief, S. Guyard, V. H. Etgens, and Y. Garreau, Phys. Rev. B **68**, 115309 (2003).

[21] A. Ouerghi, M. Marangolo, M. Eddrief, B. B. Lipinski, V. H. Etgens, M. Lazzeri, H. Cruguel, F. Sirotti, and A. Coati, and Y. Garreau, Phys. Rev. B **74**, 155412 (2006).

[22] M. N. Baibich, J. M. Broto, A. Fert, F. N. V. Dau, F. Petroff, P. Etienne, G. Creuzet, A. Friederich, and J. Chazelas, Phys. Rev. Lett. **61**, 2472 (1988).

[23] G. Binasch, P. Grünberg, F. Saurenbach, and W. Zinn, Phys. Rev. B **39**, 4828 (1989).

[24] J. Daughton, J. Brown, E. Chen, R. Beech, A. Pohm, and W. Kude, IEEE Trans. Magn. **30**, 4608 (1994).

[25] Wall Street Journal **10**, p.B8 (1997).

[26] M. Julliere, Phys. Lett **54A**, 225 (1975).

[27] S. Yuasa, T. Katayama, T. Nagahama, A. Fukushima, H. Kubota, Y. Suzuki, and K. Ando, editor, *Magnetic Heterostructures-Advances and Perspectives in Spinstructures and Spintransport*, Springer Tracts in Modern Physics, 2007.

[28] S. Yuasa, T. Katayama, T. Nagahama, A. Fukushima, H. Kubota, Y. Suzuki, and K. Ando, Appl. Phys. Lett. **87**, 222508 (2005).

[29] S. S. P. Parkin, C. Kaiser, A. Panchula, P. M. Rice, B. Hughes, M. Samant, and S. H. Yang, Nature Mater. **3**, 862 (2004).

[30] D. Hägele, M. Oestreich, W. W. Rühle, N. Nestle, and K. Eberl, Appl. Phys. Lett. **73**, 1580 (1998).

[31] A. Filipe, H. -J. Drouhin, G. Lampel, Y. Lassailly, J. Nagle, J. Peretti, V. I. Safarov, and A. Schuhl, Phys. Rev. Lett. **80**, 2425 (1998).

[32] J. D. Aldous, C. W. Burrows, M. S. Ana, R. Beanland, I. Maskery, M. K. Bradley, M. D. S. Dias, J. B. Staunton, and G. R. Bell, Phys. Rev. B **85**, 060403 (2012).

[33] J. D. Aldous, C. W. Burrows, I. Maskery, M. Brewer, D. Pickup, M. Walker, J. Mudd, T. P. A. Hase, J. A. Duffy, S. Wilkins, C. S. Hanke, G. R. Bell, J. Crys. Growth , 1 (2012).

[34] M. Tanaka, J. P. Harbison, M. C. Park, Y. S. Park, T. Shin, and G. M. Rothberg, Appl. Phys. Lett. , 1964 (1994).

[35] S. A. Hatfield, G. R. Bell, J. Crys. Growth , 165 (2006).

[36] R. A. de Groot, F. M. Mueller, P. G. van Engen, and K. H. J. Buschow, Phys. Rev. Lett. **50**, 2024 (1983).

[37] T. Amemiya, Y. Ogawa, H. Shimizu, H. Munekata, and Y. Nakano, Appl. Phys. Express **1**, 022002 (2008).

[38] G. C. Han, C. K. Ong, T. Y. F. Liew, J. Magn. Magn. Mater. **192**, 233 (1999).

[39] H. Akinaga, S. Miyanishi, and Y. Suzuki, Jpn. J. Appl. Phys **35**, L897 (1996).

[40] J. C. Zheng and J. W. Davenport, Phys. Rev. B **69**, 144415 (2004).

[41] A. Continenza, S. Picozzi, W. T. Geng, and A. T. Freeman, Phys. Rev. B **64**, 085204 (2001).

[42] P. Atkins, and J. De Paula, *Atkins' physical chemistry*, Oxford University Press, 2010.

[43] F. W. Harrison, W. P. Osmond, and R. W. Teale, Phys. Rev. **106**, 865 (1957).

[44] J. E. Pask, L. H. Yang, C. Y. Fong, W. E. Pickett, and S. Dag, Phys. Rev. B **67**, 224420 (2003).

[45] S. Mollet, and S. J. Jenkins, J. Phys.: Condens Matter **19**, 315214 (2007).

[46] J. N. Andersen, H. B. Nielsen, L. Petersen, and D. L. Adams, J. Phys, C: Solid St. Phys. **17**, 173 (1984).

[47] R. L. Park, H. Hannibal, and Jr. Madden, Surf. Sci. **11**, 188 (1968).

[48] E. A. Wood, J. Appl. Phys **35**, 1306 (1964).

[49] D. W. Pashley, Advan. Phys. **5**, 173 (1956).

[50] P. A. M. Dirac, Proc. R. Soc. **123**, 714 (1929).

[51] M. Born and J. R. Oppenheimer, Annalen der Physik **389**, 457 (1927).

[52] D. S. Sholl, and J. A. Steckel, *Density functional thory: A practical Introduction*, John Wiley & Sons, Inc., Hoboken, New Jersey, 2009.

[53] P. Hohenberg, and W. Kohn, Phys. Rev. B **386**, 864 (1964).

[54] W. Kohn, and L. J. Sam, Phys. Rev. A **140**, 1133 (1964).

[55] W. Kohn, Rev. Mod. Phys. **71**, 1253 (1999).

[56] E. Wigner, Trans. Faraday Soc. **34**, 678 (1938).

[57] D. Ceperley, Phys. Rev. B **18**, 3126 (1978).

[58] D. M. Ceperley, and B. J. Alder, Phys. Rev. Lett. **45**, 566 (1980).

[59] R. O. Jones, and O. Gunnarsson, Rev. Mod. Phys. **61**, 689 (1989).

[60] J. P. Perdew, J. A. Chevary, S. H. Vosko, K. A. Jackson, M. R. Pederson, D. J. Singh, and C. Fiolhais, Phys. Rev. B **46**, 6671 (1992).

[61] J. P. Perdew, K. Burke, and M. Ernzerhof, Phys. Rev. Lett. **77**, 3865 (1996).

[62] A. E. Mattsson, R. Armiento, P. A. Schultz, and T. R. Mattsson, Phys. Rev. B **73**, 195123 (2006).

[63] Accelrys Materials Studio 8.0 Help, http://www.tcm.phy.cam.ac.uk/castep/ documentation/WebHelp/content/modules/ castep/tskcastepsetelecpotentials.htm (December 17, 2014).

[64] M. C. Payne, M. P. Teter, D. C. Allan, T. A. Arias, and J. D. Joannopoulos, Rev. Mod. Phys. **64**, 1045 (1992).

[65] M. D. Segall, J. D. Lindan, Philip, M. J. Probert, C. J. Pickard, P. J. Hasnip, S. J. Clark, and M. C. Payne, J. Phys.: Condens Matter **14**, 2717 (2002).

[66] H. J. Monkhorst, and J. D. Pack, Phys. Rev. B **13**, 5188 (1976).

[67] J. S. Lin, A. Qteish, M. C. Payne, and V. Heine, Phys. Rev. B **47**, 4174 (1993).

[68] V. P. Madeleine Meyer, editor, *Surface and interface science, Volume 1: comncepts and methods*, Kluwer Academic Publishers, 1991.

[69] G. B. Bachelet, D. R. Hamann, and M. Schlüter, Phys. Rev. B **26**, 4199 (1982).

[70] D. Vanderbilt, Phys. Rev. B **41**, 7892 (1990).

[71] G. Kresse, and J. Hafner, J. Phys: Condens. Matter **6**, 8245 (1994).

[72] D. Porezag, M. R. Pederson, and A. Y. Liu, Phys. Rev. B **60**, 14132 (1999).

[73] D. Porezag, M. R. Pederson, and A. Y. Liu, Phys. stat. sol. (b) , 219 (2000).

[74] K. Lejaeghere, V. Van Speybroeck, G. Van Oost, and S. Cottenier, Crit. Rev. Solid State Mater. Sci. **39**, 1 (2014).

[75] R. Fletcher, *Practical methods of optimization*, New York: John Wiley & Sons, 1987.

[76] R. S. Mulliken, J.Chem.Phys. **23**, 1833 (1955).

[77] R. S. Mulliken, J.Chem.Phys. **23**, 1841 (1955).

[78] R. S. Mulliken, J.Chem.Phys. **23**, 2338 (1955).

[79] R. S. Mulliken, J.Chem.Phys. **23**, 2343 (1955).

[80] M. D. Segall, C. J. Pickard, R. Shah, and M. C. Payne, Mol. Phys. **89**, 571 (1996).

[81] M. D. Segall, R. Shah, C. J. Pickard, and M. C. Payne, Phys. Rev. B **54**, 16317 (1996).

[82] D. Sanchez-Portal, E. Artacho, and J. M. Soler, Solid State Commun. **95**, 685 (1995).

[83] J. D. Aldous, *Growth, characterisation and surface structures of MnSb and NiSb thin films*, PhD thesis, University of Warwick, 2011.

[84] M. A. Van Hove, W. H. Weinverg and C.-M. Chan, *Low Energy electron diffraction - experiment, theory and surface structure determination*, Springer Verlag, 2012.

[85] J. C. Slater, Phys. Rev. **51**, 846 (1937).

[86] B. Pendry, J. Phys, C: Solid St. Phys. **13**, 937 (1980).

[87] M. A. van Hove, and A. Barbieri, Barbieri/van Hove phase shift package, private communication .

[88] G. Held, and W. Braun, Cambridge LEED Package, private communication .

[89] V. Blum, L. Hammer, C. Schmidt, W. Meier, O. Wieckhorst, S. Müller, and K. Heinz, Phys. Rev. Lett. **89**, 266102 (2002).

[90] C. Rogero, C. Polop, L. Magaud, J. L. Sacedón, P. L. de Andrés, and J. A. Martín-Gago, Phys. Rev. B **66**, 235421 (2002).

[91] M. Fukuoka, M. Okada, M. Matsumoto, S. Ogura, K. Fukutani, and T. Kasai, Phys. Rev. B **75**, 235434 (2007).

[92] J. P. Perdew, and Y. Wang, Phys. Rev. B **45**, 13244 (1992).

[93] G. X. Qian, and R. M. Martin, and D. J. Chadi, Phys. Rev. B **38**, 7649 (1988).

[94] D. K. Biegelsen, R. D. Bringans, J. E. Northrup, and L. -E. Swartz, Phys. Rev. Lett. **65**, 452 (1990).

[95] F. R. de Boer, R. Boom, and A. R. Miedema, Physica B+C **113**, 18 (1982).

[96] S. J. Jenkins, Phys. Rev. B **70**, 245401 (2004).

[97] M. W. Finnis, and V. Heine, J. Phys. F: Met. Phys **4**, L37 (1974).

[98] K. Wandelt, editor, *Computer simulation in materials science: interatomic potentials, simulation techniques, and applications*, Wiley-VCH, 2012.

[99] A. Gro, *Theoretical surfae science: a microscopic perspective*, Springer-Verlag, 2007.

[100] S. A. Hatfield, *Heteroepitaxial growth of MnSb on III-V semiconductro substrates*, PhD thesis, University of Warwick, 2007.

[101] H. Akinaga, M. Mizuguchi, K. Ono, and M. Oshima, Appl. Phys. Lett. **76**, 2600 (2000).

[102] H. Akinaga, Semicond. Sci. Tech. **17**, 322 (2002).

[103] M. J. Madou, editor, *Fundametals of microfabrication and nanotechnology*, CRC Press, 2011.

[104] G. W. Zhou, and J. C. Yang, Surf. Sci. , 357 (2004).

[105] E. Penev, P. Kratzer, and M. Scheffler, Phys. Rev. B **64**, 085401 (2001).

[106] S. A. Hatfield, and G. R. Bell, Surf. Sci. **601**, 5368 (2007).

[107] F. Ercolessi, E. Tosatti, and M. Parrinello, Phys. Rev. Lett. **57**, 719 (1986).

[108] N. Takeuchi, C. T. Chan, and K. M. Ho, Phys. Rev. B **43**, 13899 (1991).

[109] A. Kirakosian, M. J. Comstock, J. Cho, and M. F. Crommie, Phys. Rev. B **71**, 113409 (2005).

[110] R. Pentcheva, and M. Scheffler, Phys. Rev. B **65**, 155418 (2002).

[111] H. Jahn, and E. Teller, Proc. R. Soc. London, Ser. A **164**, 916 (1938).

[112] C. J. Pickard and R. J. Needs, Nature **9**, 624 (2010).

[113] H. Jones, Proc. R. Soc. A **147**, 396 (1934).

[114] G. J. Ackland and I. R. Macleod, New J. Phys. **6**, 138 (2004).

[115] G. Held, and W. Braun, Cambridge LEED Package (2013).

[116] S. A. Hatfield, J. D. Aldous, and G. R. Bell, Appl. Surf. Sci. **255**, 3567 (2009).

[117] K. Heinz, Rep. Prog. Phys. **58**, 637 (1995).

[118] N. Fujimura, T. Nishihara, S. Goto, J. F. Xu, and T. lto, J. Crys. Growth , 130 (1993).

[119] S. -W. Chan, J. Phys. Chem. Solids **55**, 1137 (1994).

[120] T. Lei, K. F. Ludwig Jr., and T. D. Moustakas, J. Appl. Phys. **74**, 4430 (1993).

[121] T. Kakudate, N. Yoshimoto, and Y. Saito, Appl. Phys. Lett. **90** (2007).

[122] D. J. Larson, A. Cerezo, P. H. Clifton, A. K. Petford-Long, R. L. Martens, T. F. Kelly, and N. Tabat, J. Appl. Phys. **89**, 7517 (2001).

[123] G. Katsaros, G. Costantini, M. Stoffel, R. Esteban, A. M. Bittner, A. Rastelli, U. Denker, O. G. Schmidt, and K. Kern, Phys. Rev. B **72**, 195320 (2005).

[124] G. Radtke, M. Couillard, G. A. Botton, D. Zhu, and C. J. Humphreys, Appl. Phys. Lett. **100**, 011910 (2012).

[125] J. F. Anderson, M. Kuhn, U. Diebold, K. Shaw, F. Stoyanov, and D. Lind, Phys. Rev. B **56**, 9902 (1997).

[126] S. Estradé, J. Arbiol, F. Peiró, I. C. Infante, F. Sánchez, J. Fontcuberta, F. de la Peña, M. Walls, and C. Colliex, Appl. Phys. Lett. **93** (2008).

[127] W. Lee, M. C. Jeong, and J. M. Myoung, Appl. Phys. Lett. **85**, 6167 (2004).

[128] Y. C. Shih, M. Murakami, E. L. Wilkie, and A. C. Callegari, J. Appl. Phys. **62**, 852 (1987).

[129] Y. B. Zhang, M. H. N. Assadi, and S. Li, AIV Advances **2**, 042155 (2012).

[130] C. Kittel, *Introduction to solid state physics*, John Wiley & Sons, Inc, 2005.

[131] G. Kresse, O. Dulub, and U. Diebold, Phys. Rev. B **68**, 245409 (2003).

[132] G. R. Bell, C. W. Burrows, T. P. A. Hase, M. J. Ashwin, S. R. C. Mcmitchell, A. M. Sanchez, and J. D. Aldous, Spin **4**, 1440025 (2014).

[133] C. W. Burrows, A. Dobbie, M. Myronov, T. P. A. Hase, S. B. Wilkins, M. Walker, J. J. Mudd, I. Maskery, M. R. Lees, C. F. McConville, D. R. Leadley, and G. R. Bell, Cryst. Growth Des. **13**, 4923 (2013).

[134] J. H. Zhao, F. Matsukura, K. Takamura, E. Abe, D. Chiba, and H. Ohno, Appl. Phys. Lett. **79**, 2776 (2001).

[135] S.-H. Wei, and A. Zunger, Phys. Rev. B **37**, 8958 (1988).

[136] S. H. Wei, and A. Zunger, Phys. Rev. B **35**, 2340 (1987).

[137] S. Greenwald, and J. S. Smart, Nature **166**, 523 (1950).

[138] J. S. Smart, and S. Greenwald, Phys. Rev. **82**, 113 (1951).

[139] I. Galanakis, and P. Mavropoulos, Phys. Rev. B **67**, 104417 (2003).

[140] I. Galanakis, P. H. Dederichs, and N. Papanikolaou, Phys. Rev. B **66**, 134428 (2002).

[141] I. Galanakis, P. H. Dederichs, and N. Papanikolaou, Phys. Rev. B **66**, 174429 (2002).

[142] F. D. Murnaghan, Proc. Natl. Acad. Sci. U.S.A. **30**, 244 (1944).

[143] F. Birch, J. Geophys. Res. **86**, 1257 (1978).

[144] J. E. Northrup, and S. Froyen, Phys. Rev. Lett. **71**, 2276 (1993).

[145] W. G. Schmidt, F. Bechstedt, N. Esser, M. Pristovsek, C. Schultz, and W. Richter, Phys. Rev. B **57**, 14596 (1998).

[146] W. G. Schmidt, S. Mirbt, and F. Bechstedt, Phys. Rev. B **62**, 8087 (2000).